# Improving estimates of sub-daily gross primary production from solar-induced chlorophyll fluorescence by accounting for light distribution within canopy

**Ruonan Chen[1,2,3], Liangyun Liu [1,2,3*], Xinjie Liu [1,2], Zhunqiao Liu[4], Lianhong Gu[5], Uwe Rascher[6]**

[1]International Research Center of Big Data for Sustainable Development Goals (CBAS), Beijing, 100049, China

[2]Key Laboratory of Digital Earth Science, Aerospace Information Research Institute, Chinese Academy of Sciences, Beijing, 100094, China;

[3]College of Resources and Environment, University of Chinese Academy of Sciences, Beijing, 100049, China

[4]State Key Laboratory of Soil Erosion and Dryland Farming on the Loess Plateau, Northwest A&F University, Yangling, Shaanxi 712100, China

[5]Environmental Sciences Division and Climate Change Science Institute, Oak Ridge National Laboratory, Oak Ridge, TN 37831, USA;

[6]Institute of Bio- and Geosciences, Plant Sciences, Forschungszentrum Jülich GmbH, Jülich, Germany.

Corresponding author: Liangyun Liu (liuly@radi.ac.cn)

## Abstract

Solar-induced chlorophyll fluorescence (SIF) has long been regarded as a proxy for photosynthesis and has shown superiority in estimating gross primary production (GPP) compared to traditional vegetation indices, especially in evergreen ecosystems. However, current SIF-based GPP estimations regard the canopy as a large leaf and seldom consider the impact of interactions among light, canopy structure, and leaf physiology. In this study, we proposed GPP estimation models with different descriptions of light–structure–physiology interactions (including the layered model, the two-leaf model, and the layered two-leaf model)

and compared their performances with the big-leaf model using half-hourly (or hourly) observations at evergreen needleleaf forest sites. First, we found that the big-leaf model underestimated GPP, especially at noon. All models showed higher accuracy than that of the big-leaf model. Second, we investigated the diurnal dynamics of GPP estimations in each canopy layer and found that models with a two-leaf assumption captured the diurnal variations in GPP better than that with the layered assumption. We also deduced that the poor performance of the big-leaf model was related to its overestimation of the overall light stress on the redox state of PSII reaction centers (qL). Finally, we noticed that the qL at the canopy scale had lower sensitivity to light change than the single-leaf qL and that the light response of canopy-scale qL was influenced by the leaf area index during seasonal cycles. Overall, this study describes methods to accurately estimate sub-daily GPP from SIF in evergreen needleleaf forests and demonstrates that the interactions among light, canopy structure, and leaf physiology regulate the SIF-GPP relationship at the canopy scale. Further, it indicates the need to consider the description of light distribution within the canopy in next-generation terrestrial biosphere models, even if they incorporate SIF to constrain their parameterization. Thus, upscaling the established leaf-scale mechanistic SIF-GPP relationship or findings to canopy-scale applications still requires much work, especially when there are significant changes in environmental conditions and their within-canopy distributions.

**Keywords:** solar-induced chlorophyll fluorescence (SIF); gross primary productivity (GPP); two-leaf model; layered model; evergreen needle forests

## 1. Introduction

Photosynthesis in terrestrial ecosystems plays an important role in the global carbon cycle, offsetting approximately 30% of anthropogenic carbon dioxide ($CO_2$) emissions over the past century (Friedlingstein et al., 2020). Compared to ocean carbon sinks, land carbon cycles are sensitive to climate change and are highly unstable (Ciais et al., 2005; Friedlingstein et al., 2020; Luijkx et al., 2015; Maia et al., 2020), making them a crucial but largely uncertain part of global change studies. As one of the largest fluxes in the terrestrial carbon cycle (Wang et al., 2022b),

gross primary production (GPP) indicates the $CO_2$-assimilation ability of vegetation and is the foundation of many ecosystem functions and services (for example, providing food and fiber, altering local climate, and regulating the land–air interaction process) (Migliavacca et al., 2021; Ryu et al., 2019; Xiao et al., 2019). However, substantial difficulties and uncertainties in GPP quantification at a large scale remain despite decades of research (Ryu et al., 2019).

Before the emergence of state-of-art solar-induced chlorophyll fluorescence (SIF) techniques, ground GPP data were mainly obtained from in situ measurements of eddy covariance flux towers with limited spatial representativeness, and global GPP products were either model-based estimates, including light use efficiency models and process models, such as VPM (Zhang et al., 2017) and BEPS (Chen et al., 1999), or upscaled values from flux tower observations (for example, FLUXCOM) (Jung et al., 2019). These traditional GPP measurements and products are either not ideal for supporting the analyses on large spatiotemporal scales due to significant regional bias or are based on multiple large simplifications and assumptions (Anav et al., 2015; Wang et al., 2022a), leading to large uncertainties and divergence in their long-term trends (Cai et al., 2014; Wang et al., 2022a; Zheng et al., 2020). Remote-sensing methods based on vegetation indices (VIs) could partly capture the dynamics of photosynthesis and assist in the estimation of GPP, buthe effectiveness of VIs-based methods is mainly related to their representativeness of vegetation greenness (Li and Xiao, 2020), indicating that they might lose their power in ecosystems with an almost invariant canopy structure (such as evergreen forests) (Magney et al., 2019). The rapid development of SIF measurement and retrieval methods has facilitated the monitoring of photosynthetic dynamics on a large scale (Guanter et al. 2021; Joiner et al. 2011, 2016; Mohammed et al. 2019; Schimel et al. 2015; Sun et al. 2017; Du et al., 2022), although some limitations still exist, such as the sparse sampling or coarse spatial resolution of current satellite-based SIF products. SIF is the electromagnetic signal emitted by chlorophyll molecules after absorbing solar radiation~~, and~~. Together with non-photochemical quenching (NPQ) and photochemical reactions, SIF consumes ~~it competes with photochemical reactions and non-photochemical quenching (NPQ) for~~ the total absorbed light inside plants. Therefore, SIF contains information on physiology that can be detected using remote sensors (Porcar-Castell

et al., 2014). Numerous studies have demonstrated the tight link between SIF and GPP, although studies also show the decoupling of SIF and GPP during mild stress events (Helm et al., 2020; Marrs et al., 2020) and changes in their relationship at different spatiotemporal scales (Magney et al., 2020). Further, SIF is employed as a proxy for photosynthesis in many agricultural, ecological, and Earth system studies (Sun et al., 2015; Wang et al., 2020; Y. Zhang et al., 2020). Several studies have directly used the empirical relationship to estimate GPP via SIF observations, even though this relationship has been proven to be biome-specific (Damm et al., 2015; Liu et al., 2017).

~~Despite the widespread use of SIF as a proxy for GPP, discrepancies between them remain. Following the framework of Monteith's light use efficiency model (Monteith, 1972),~~ Although both SIF and GPP are largely driven by absorbed photosynthetic active radiation (APAR)~~, which largely explains their strong correlation~~ at the canopy scale (Du et al., 2017; Miao et al., 2018)~~.~~, discrepancies between them remain. ~~However, GPP is also influenced by light use efficiency (LUE), and canopy SIF is regulated by fluorescence quantum efficiency (ΦF) and escape probability (fesc). T~~The possible discrepancy between LUE and ΦF×fesc is one of the essential explanations for the dynamic relationship or decoupling between SIF and GPP. ~~At the leaf scale,~~ The physiological dynamics in the ~~both~~ ΦF ~~and~~ LUE relationship~~carry physiological information~~ (Porcar-Castell et al., 2014)~~, and the dynamics in their relationship~~ theoretically influence the SIF-GPP relationship~~.~~, and the~~For far-red SIF, a~~ positive correlation between LUE and fesc (for far-red SIF) ~~is~~ found at the seasonal scale~~,~~ also ~~strengthening~~ strengthens the link between SIF and GPP (Liu et al., 2020). These mechanisms result in the coupling of SIF and GPP as a mixture of canopy structure interference and physiological processes. ~~Previous studies have provided us with the opportunity to obtain the total SIF at the photosystem scale (Liu et al., 2019; Liu et al., 2020; Yang et al., 2020; Zeng et al., 2019), with which we can decompose the contribution of the canopy structure and reduce the uncertainty in SIF-GPP relationships (Zhang et al., 2019). However, r~~Recent studies have ~~shown that~~demonstrated the variant ~~the~~ physiological linkage between SIF and GPP ~~is also variant~~ (Magney et al., 2020)~~. Further~~, which~~, this relationship~~ can be influenced by the environment and the status of the plant (for example, stress conditions and development stages) (Chen et al.,

2022b, 2022a; Kim et al., 2021; Paul-Limoges et al., 2018; Zhuang et al., 2020). Even for evergreen needleleaf forests (ENF) with little variation in fesc during seasonal cycles, ~~the~~ SIF does not change in perfect agreement with GPP and shows lower sensitivity to environmental changes (Pierrat et al., 2022b; Yang et al., 2022).

Therefore, accurate estimation of GPP using SIF ~~also~~ requires the construction of a mechanistic model with the help of physiological findings. The mechanistic light response (MLR) model proposed by Gu (2019) ~~is a model that helps us to understand the association and inconsistency of the physiological information in SIF and GPP. It~~ links the quantitative SIF-GPP relationship to active fluorescence parameters with specific physiological meanings, such as qL (the fraction of opened PSII reaction centers) and $\Phi_{PSIImax}$ (the maximum photochemical quantum yield of PSII)~~, thus allowing the combination of passive and active fluorescence measurements to directly estimate GPP~~. In this model, qL is a key parameter influenced by the actual illumination condition of leaves; thus, the dynamics of qL are crucial to SIF-based GPP estimations ~~during~~ in diurnal cycles. The effectiveness of the MLR model has already been demonstrated by a previous leaf-scale study (Han et al., 2022b) but has not been extensively tested at the canopy scale or long time scales.

~~Although o~~One study has attempted to directly estimate GPP from canopy SIF in a winter-wheat field (Liu et al., 2022), but it is based on ~~uses~~ the big-leaf assumption ~~of canopy structure~~. The big-leaf assumption regards vegetation as a large flat leaf and assumes the same leaf property and the same direct and diffuse radiation conditions in the canopy (Guan et al., 2022; McCallum et al., 2013; Sellers et al., 1992). Therefore, GPP estimations using this method neglect the possible impact of the light distribution (caused by the three-dimensional structure) within the canopy. This ~~big-leaf~~ assumption is acceptable for crops with a simple structure and low height (anthropogenic ecosystems), as indicated by the model's success in direct SIF-based estimation in Liu's study (2022), but it may be unsuitable for natural ecosystems with complex canopy structures. ~~This~~ The big-leaf assumption does not ~~introduce~~ cause much uncertainty ~~to GPP estimation~~ at the seasonal scale ~~(Chen et al., 1999)~~, but is unsuitable for the half-hourly estimation of GPP in forests (Chen et al., 1999). ~~During daily cycles, the diurnal variation in light leads to a nonlinear relationship between fluorescence and photosynthesis due to their~~

~~different light responses (Liu et al., 2021; Maguire et al., 2020). In addition, d~~Diurnal changes in incident light interplay with the canopy structure, leading to a dynamic vertical gradient (redistribution) of light within the canopy. This interaction changes the actual light environment faced by each leaf, thereby causing vertical variations in the biophysical status of leaves and influencing the diurnal patterns of SIF and GPP (Chang et al., 2021)~~.~~ Therefore, it is necessary to consider the dynamic light and its interaction with the canopy structure and leaf physiology along the vertical dimension when using canopy SIF observations to estimate the half-hourly GPP in forest ecosystems. Recently, some studies using the LUE framework considered the impact of vertical light gradient on LUE and improved the GPP estimation(Guan et al., 2022, 2021), but there are no study directly considering the impact of vertical light gradient on SIF-GPP relationship to improve SIF-based GPP estimation at sub-daily scales.

Previous leaf-scale observations at two ENF sites have demonstrated that knowledge of sub-canopy and diurnal patterns of irradiance can assist in the investigation of physiological constraints on fluorescence (Maguire et al., 2020), but there have been few canopy-scale studies accounting for this issue. Recently, an observational study investigated the contributions of understory and midstory SIF to the total SIF, and it showed the different relationships between GPP and SIF in different layers (Morozumi et al., 2023). In addition, total emitted SIF was found to outperform top-of-canopy SIF in GPP estimation in many observational studies (~~X.~~ Liu et al., 2020; Lu et al., 2020; ~~Z.~~ Zhang et al., 2020), which indicate the importance of considering vertical variations within the canopy. There was also a study combining hyperspectral observations at different canopy layers with SCOPE modeling to estimate the total SIF in a subtropical evergreen forest. The results of that study showed that using the layered SIF benefits GPP estimation (Zhu et al., 2023). ~~In addition~~These studies highlight the importance of considering canopy vertical heterogeneity in the interpretation and application of SIF (Chang et al., 2021).

The vertical distribution of light plays an important role in the canopy's vertical heterogeneity. It should be considered in SIF-based GPP estimation since it impacts both the source energy for photosynthesis and the photosynthetic response of spectral fluorescence (Rajewicz et al., 2023). Dividing the canopy into several layers and estimating the GPP for each layer separately

may be a solution that can be used to consider the vertical distribution of light, but does not consider the situation in which there may be two types of leaves irradiated by direct light or scattered light at the same depth in the canopy. ~~At midday in summer~~Under high light conditions, leaves exposed to direct light are likely to be light-saturated or even photoinhibited, whereas leaves exposed to scattered light can still photosynthesize efficiently. Therefore, differentiating sunlit and shaded leaves can improve the SIF-based GPP estimation (Zhang et al., 2023). Being widely used in terrestrial biosphere models, the two-leaf model ~~simply~~ divides the leaves into shaded and sunlit leaves and describes the different light environments faced by them (Chen et al., 1999; Guan et al., 2022; He et al., 2013). Thus, this method considers the different effects of direct and scattered light on plant photosynthesis. However, because it uses the overall light environment of shaded leaves and does not explicitly describe the scattered light gradient in the vertical direction, we are unsure whether this simplification will significantly impact the SIF estimation of GPP. The methods described above illustrate within-canopy light distribution in different ways, but we cannot directly determine the description that is more suitable for SIF-based half-hourly GPP estimation in ENFs.

Therefore, in this study, we used SIF to estimate GPP using tower-based observations at ENF sites under the framework of the MLR model. We employed a layered model (separating leaves into several layers), a two-leaf model (separating leaves into sunlit and shaded groups), and a layered two-leaf model (separating leaves into sunlit and shaded groups for each layer) to describe the interaction among the light conditions, canopy structure, and leaf physiology to estimate half-hourly GPP. We then compared the effectiveness of these three models with that of the big-leaf assumption and analyzed their performances in tracking GPP dynamics during the day. With the help of accurate GPP estimation results, we obtained the canopy-scale qL, determined its light response pattern, and compared it with the leaf-scale pattern. In this study, we attempted to answer the following questions:1. How can SIF-based GPP estimates be improved at the half-hourly scale, and how does the big-leaf assumption affect the SIF-based GPP estimation at ENF sites? 2. What are the differences in the performance of models with different descriptions of light–structure–physiology interactions (including layered, two-leaf, and layered two-leaf models)? 3. How does the redistribution of light within the canopy affect

the diurnal variation and vertical distribution pattern of GPP and plants' physiological properties (qL)? 4. What is the difference in the light responses of the overall qL (referred to as "canopy-scale qL" in the following part) and the single-leaf qL, and what factors can explain this difference?

## 2. Materials and Methods

### 2.1 Study Sites

In this study, we used tower-based SIF and GPP observations from three open-access ENF sites to examine the performance of our methods; to investigate the dynamics of the estimated GPP, light conditions, and qL at different canopy depths; and to obtain the canopy-scale qL. Among these sites, the data for the boreal forest site (Southern Old Black Spruce, located in Canada, site ID: CA-Obs) was obtained from FLUXNET and spanned September 2018 to December 2020 (Pierrat et al., 2022); the data for subalpine conifer forest site (Niwot Ridge, located in America, site ID: US-NR1) was obtained from AmeriFlux, and had observations from September 2017 to June 2018 (Magney et al., 2019); and the data for the temperate ENF site (located in Taehwa Mountain in South Korea, site ID: KR-TCK) was obtained from AsiaFlux, covering measurements from September 2018 to December 2018 (Kim et al., 2021). The photosynthetic active radiation (PAR) averages of the observations were similar during the study period (for the KR-TCK site, 680.59 μmol/$m^2$/s; for the CA-obs site, 607.22 μmol/$m^2$/s; for the US-NR1site, 689.06 μmol/$m^2$/s). The annual average air temperature at these sites was 1.4 °C (CA-obs), 1.5 °C (US-NR1), and 12.7 °C (KR-TCK). Other detailed information regarding these sites is provided in Table S1. We tested the landscape heterological conditions around the sites via visual interpretation using the Google Earth platform, and images of the landscape conditions around these sites are shown in Figure S1. Using the ratio of 30 m NDVI (the normalized difference vegetation index) to 250 m NDVI as the indicator of representativeness, we found that all sites are generally homogeneous and have fine representativeness (close to 1; Figure S2).

## 2.2 Datasets

All the SIF data used in this research were obtained from canopy-scale measurements using tower-based monitoring systems. For the CA-obs site, the average canopy height was approximately 16 m, and a scanning spectrometer system (Photospec) was installed at the top of a 26 m tower to obtain the canopy SIF (Pierrat et al., 2022). The PhotoSpec system enables SIF retrieval in the red (680–686 nm) and far-red (745–758 nm) wavelength ranges (Grossmann et al., 2018), as well as supports the calculation of vegetation indices due to its moderate resolution at the corresponding wavelengths. The US-NR1 site also used the Photospec system fixed on the top of a tower (also 26 m above the ground) and measured the spectra with a time resolution of ~20 s per measurement (Magney et al., 2019). SIF values at both CA-obs and US-NR1 sites were retrieved using a Fraunhofer-line-based based fitting algorithm (Grossmann et al., 2018), and the SIF retrieval error was lower than 0.2 $Wm^2/sr/\mu m$ at the CA-obs site. For the KR-TCK site, the average canopy height was approximately 20 m, and observations were measured using a QE Pro system installed at the top of the 40 m tower. At this site, only far-red SIF (760 nm) was retrieved using the Singular Vector Decomposition (SVD) method, and SIF values with rRMSE larger than 25% were removed to ensure data quality. The spectral reflectance at this site was collected using Jaz spectroradiometers (Ocean Insight, Dunedin, FL, USA), which cover a spectral range of 350–1020 nm (Kim et al., 2021). Notably, the unit of SIF measurements at both the CA-obs and US-NR1 sites was $mW/m^2/nm/sr$ due to the hemispherical–conical configuration of Photospec, whereas the unit of SIF measurements at the KR-TCK site was $mW/m^2/nm$ because two cosine correctors were used to obtain the hemispheric SIF.

GPP measurement relies on the eddy covariance technique. For all sites, a 3-D sonic anemometer and infrared gas analyzer fixed on the flux towers were used to measure the wind speed and $CO_2$ concentration, which allowed calculation of the 30 min net ecosystem exchange (NEE) using Eddy-Pro software. Then, various preprocessing procedures, including data quality control, night-time $CO_2$ flux corrections, and gap filling, were employed on the NEE time series; finally, GPP was obtained after the partition step (Barr et al., 2004; Reichstein et

al., 2005; Wutzler et al., 2018).

In addition to GPP observations, the flux tower provides meteorological data every 30 min. In this study, we mainly used air temperature, PAR, and relative humidity data. Using air temperature and relative humidity, we further determined the vapor pressure deficit according to Tetens's formula (Monteith and Unsworth, 1990) for describing atmospheric dryness and calculating carbon-reaction-related parameters:

$$VPD = 0.61078 \times e^{\frac{17.27 \times T_a}{T_a + 237.3}} \times (1 - RH) \quad (1)$$

where $T_a$ is the air temperature (°C), RH is relative humidity (%), and VPD is the vapor pressure deficit (kPa). In our study, the unit of VPD was converted to Pa. By averaging the records every half hour, all these sites provided a continuous time series of observations at a temporal resolution of 30 min, except US-NR1 (because only hourly GPP was obtained at this site). Based on the 30 min incident PAR and the PAR at the top of the atmosphere (which was calculated using the latitude, longitude, and corresponding time), we calculated the clearness index following the method in Chen et al. (1999) to describe the weather condition and determine the ratio of direct to diffuse light in the two-leaf model:

$$\mathrm{CI} = \frac{\mathrm{PAR}}{\mathrm{PAR_{TOA}}} = \frac{\mathrm{PAR}}{S_0 \times 0.46} \quad (2)$$

where $S_0$ represents the solar constant (1367 W/m$^2$), and 0.46 is the fraction of PAR in the incoming solar radiance. We used 0.219 covert the unit of PAR (from μmol/m$^2$/s to W/m$^2$) in this equation.

In this study, we also used the leaf area index (LAI) and clumping index (Ω) to describe canopy structure. The LAI data used in this research were obtained from a GLASS LAI product with 500 m spatial resolution (Xiao et al., 2014), and the Ω data were also from a 500 m satellite product generated based on MODIS products (Jiao et al., 2018). The time series of LAI and Ω were extracted according to the location of each site, and the possible uncertainties introduced by satellite products were tested using ground measurement LAI data at the KR-TCK site. We also used another clumping index dataset to clarify the uncertainties introduced by different satellite clumping index products (Li and Fang, 2022). To estimate the escape probability of

SIF photons (details in Section 2.5, equation 18), we also employed NDVI, NIR (near-infrared reflectance), and fPAR using the in situ measurements provided by each site (Kim et al., 2021; Magney et al., 2019; Pierrat et al., 2022a). More details can be found in the original papers (Kim et al., 2021; Magney et al., 2019; Pierrat et al., 2022a).

### 2.3 The framework of SIF-based GPP estimation

In this study, we used the framework of the MLR model to estimate GPP at three ENF sites. According to previous work (Gu et al., 2019), the electron transportation rate (J) can be expressed using the full-band PSII SIF ($SIF_{full}$) and fluorescence kinetics parameters:

$$J = \frac{(1 + k_{df}) q_L \Phi_{PSIImax}}{1 - \Phi_{PSIImax}} SIF_{full} \quad (3)$$

where $SIF_{full}$ refers to the total full-band PSII SIF (unit: μmol/m$^2$/s, calculation details in Section 2.5); qL is the fraction of opened PSII reaction centers; $\Phi_{PSIImax}$ is the maximum photochemical quantum yield of PSII; and $k_{df}$ is the ratio of the rate constant for constitutive heat loss to the rate constant for fluorescence emission, which is almost a constant (Zaks et al., 2012). In this study, we used $k_{df} = 9$, which was in accordance with previous measurements (Liu et al., 2022). qL can be expressed as an exponential function of light (Liu et al., 2021a), and $\Phi_{PSIImax}$ can be estimated using a quadratic function of temperature due to its high correlation with temperature (Swoczyna et al., 2022; Vitale et al., 2012):

$$q_L = a_L \, e^{-b_L PAR} \quad (4)$$

$$\Phi_{PSIImax} = a \, {T_a}^2 + bT_a + c \quad (5)$$

where Ta represents the temperature, and PAR is the photosynthetic active radiance. We took $a_L = 1$, $b_L = 0.001$, $a = -0.0011$, $b = 0.036$, and $c = 0.44$, according to previous studies (Feng et al., 2021). The values of aL and bL are consistent with previous studies (Feng et al., 2021), and the values of a, b, and c were fitted based on long-term pulse amplitude modulation (PAM) observations (for details, see Text S1).

Notably, J in the MLR model represents the actual electron transport rate, which is possible because the SIF in this model already contains information about the light reaction in

photosynthesis. Thus, this SIF-based model does not require the complex estimation of $J_{max}$ (maximum electron transport rate) and comparison of Ac (rubisco-limited photosynthesis) and Aj (RuBP-limited photosynthesis), which is crucial in the widely used FvCB model (Farquhar et al., 1980).

For the quantitative relationship between J and GPP, we referred to the FvCB model and used the following equation:

$$GPP = J\frac{C_i - \Gamma^*}{4C_i + 8\Gamma^*} \quad (6)$$

where $C_i$ is the intercellular $CO_2$ partial pressure, and Γ* is the photocompensation point of $CO_2$ in the absence of dark respiration. The estimation of $C_i$ and Γ* is included in Section 2.6.

Finally, combining Equations 3 and 6, we used the following model to estimate GPP (Gu et al., 2019):

$$GPP = \frac{C_i - \Gamma^*}{4C_i + 8\Gamma^*}\frac{(1 + k_{df})q_L\Phi_{PSIImax}}{1 - \Phi_{PSIImax}}SIF_{full} \quad (7)$$

### 2.4 Description of interactions among light, canopy structure, and leaf physiology

Compared to the vertical distribution of environmental factors such as temperature and moisture, the vertical distribution of light exposure of leaves within the canopy is highly dynamic during diurnal cycles. Because the intensity and angle of incident light vary significantly with time, light is redistributed when it penetrates the canopy, resulting in a changing vertical gradient and horizontal heterology in within-canopy illumination. Furthermore, one of the key parameters in the MLR model, qL, is highly sensitive to changes in light. Therefore, diurnal variation in light affects SIF and GPP by interfering with the canopy-scale APAR, and it also alters the relationship between SIF and GPP by regulating the qL of individual leaves. Therefore, the dynamics of the SIF-GPP relationship and canopy-scale qL (the overall qL) at the half-hourly scale are the result of the interaction among light, canopy structure, and plants' physiological properties, which should be described well for the accurate estimation of half-hourly (or hourly) GPP. In this study, we proposed and compared methods with different assumptions (layered, two-leaf, and layered two-leaf assumptions) to describe the manner in which the canopy

structure affects light distribution and qL.

### 2.4.1 Construction of a layered model

First, we used a layered model to capture the vertical gradient of light. This method separates the canopy into several layers and estimates the GPP for each layer. Adding these GPP values, we obtained the GPP of the entire canopy (the layered GPP in this study). The canopy layers were divided according to the canopy optical depth of LAI rather than vertical height. Therefore, a layer with a higher index indicated a location in a deeper canopy. The GPP estimation in each layer followed the MLR framework in Equation 7, and product of APAR and ΦF was used to divide $SIF_{full}$ of the whole canopy into the full-band PSII SIF of different layers:

$$SIF_i = SIF_{full} \times \frac{APAR_i \times \Phi F_i}{\sum_{L=1}^{n} APAR_L \times \Phi F_L} \quad (8)$$

where n represents the total number of layers; i is the layer index (ranging from 0 to n-1, where i = 0 represents the top layer); and $SIF_i$, $APAR_i$, and $\Phi F_i$ represent the full-band PSII SIF, APAR, and ΦF in layer i, respectively. We used n = 10 in this research, and to assess the uncertainty introduced by the value of n, we tested different values (n = 5, 10, 20, 40, 80, 160, 320, and 640) to examine the impact of the model performance.

In this method, we simplified the radiative transmission process and did not account for the impacts of leaf single scattering albedo, the fraction of diffused light, and the absorption and reflectance of soil backgrounds. Therefore, the APAR for each canopy layer can be expressed as the difference between the PAR at the top of this layer and the PAR at the top of the next layer (Chang et al., 2021). Here, $APAR_i$ is represented as the difference between the PAR in layer i+ 1 ($PAR_{i+1}$) and that in layer i ($PAR_i$), $\Phi F_i$ can be estimated using a fitted function of $PAR_i$ (Liu et al., 2021), and $PAR_i$ can be obtained according to Lambert–Beer's law:

$$APAR_i = PAR_i - PAR_{i+1} \quad (9)$$

$$PAR_i = PAR \times e^{-\frac{0.5 \times \Omega \times LAI_{ai}}{\cos(SZA)}} \quad (10)$$

where PAR is the incident PAR at the top of the canopy, $LAI_{ai}$ is the accumulated LAI from the top to layer i (equal to LAI × i/n), $\Omega$ is the clumping index, and SZA is the solar zenith angle.

Combining Equations 9 and 15, we can obtain the qL of layer i and use it to estimate the GPP of layer i ($GPP_i$). Although $\Phi F_i$ can be influenced by many other factors, PAR contributes significantly to its vertical variation. Compared to the variation in APAR, variation in ΦF is usually small (Van der Tol et al., 2014) and may not significantly influence the results. We examined the model's performance when solely APAR was used for the SIF partition to clarify the contribution of ΦF to the model's performance.

### 2.4.2 Construction of the two-leaf model

The second method used to describe light–structure interaction is based on the two-leaf model proposed by Chen et al. (1999), which considers different illumination conditions in the horizontal direction. In the two-leaf model, the leaves are separated into sunlit and shaded groups, and the total GPP is calculated using the sum of GPPs from sunlit and shaded leaves. Similar to the layered model, we divided the $SIF_{full}$ of the entire canopy into $SIF_{shade}$ and $SIF_{sun}$ according to APAR × ΦF. Here, $APAR_{shade}$, and $APAR_{sun}$ could be estimated using the following equations:

$$\mathrm{APAR}_{sun} = (1 - \mathrm{a}) * \mathrm{PAR}_{sun} * \mathrm{LAI}_{sun} \quad (11)$$

$$\mathrm{APAR}_{shade} = (1 - \mathrm{a}) * \mathrm{PAR}_{shade} * \mathrm{LAI}_{shade} \quad (12)$$

where a represents the leaf albedo, taken as 0.15 for evergreen needle forests according to a previous study (He et al., 2013), and $\mathrm{PAR}_{sun}$, $\mathrm{PAR}_{shade}$, $\mathrm{LAI}_{sun}$, and $\mathrm{LAI}_{shade}$ are directly calculated using the equations in the work of Chen et al. (1999) (Details in Supplementary Text S2). Because the two-leaf model includes the effects of direct PAR and diffuse PAR, calculating these parameters requires the clearness index for the partition of PAR:

$$PAR_{dif} = PAR \times (0.7527 + 3.8453CI - 16.316CI^2 + 18.962CI^3 - 7.0802CI^4) \quad (13)$$

$$PAR_{dir} = PAR - PAR_{dif} \quad (14)$$

where $PAR_{dif}$ is the diffuse PAR, $PAR_{dir}$ is the direct PAR, and CI is the clearness index.

### 2.4.3 Construction of the layered two-leaf model

Finally, although the two-leaf model considered the different light conditions for sunlit and

shaded leaves, it only divided the leaves into two groups and used $PAR_{shade}$ to represent the overall illumination of shaded leaves. This simplification neglected the vertical gradient of diffuse PAR in the canopy, which may introduce uncertainty in ecosystems with large tree heights. To examine whether this issue will influence GPP estimation, we combined the layered model and the two-leaf model to establish a layered two-leaf model. In this model, $SIF_i$ in layer i was still allocated to $SIF_{shade\_i}$ and $SIF_{sun\_i}$ based on APAR×ΦF. Therefore, $SIF_{sun}$ and $SIF_{shade}$ in layer i and were expressed as the following equations:

$$SIF_{sun\_i} = SIF_{full} \times \frac{APAR_{sun\_i} \times \Phi F_{sun\_i}}{\sum_{L=1}^{n} APAR_{shade\_L} \times \Phi F_L + \sum_{L=1}^{n} APAR_{sun\_L} \times \Phi F_{sun\_L}} \quad (15)$$

$$SIF_{shade\_i} = SIF_{full} \times \frac{APAR_{shade\_i} \times \Phi F_{shade\_i}}{\sum_{L=1}^{n} APAR_{shade\_L} \times \Phi F_L + \sum_{L=1}^{n} APAR_{sun\_L} \times \Phi F_{sun\_L}} \quad (16)$$

By replacing LAI with $LAI_{ai}$ (accumulated LAI from the top to the layer i, equals to LAI×i/n) in Chen's work (1999), we calculated $PAR_{sun\_i}$ and $PAR_{shade\_i}$ in layer i; by dividing the $LAI_i$ into sunlit fraction and shaded fraction, we obtained $LAI_{sun\_i}$ and $LAI_{shade\_i}$; finally, using equations similar to Equations 11 and 12, we obtained $APAR_{sun\_i}$ and $APAR_{shade\_i}$. In the combined model (layered two-leaf model), we estimated the $GPP_{shade}$ and $GPP_{sun}$ for each layer, and the sum of these GPPs from different leaf groups was the final GPP estimated using the third method.

### 2.5 Conversion from SIF observations to full-band PSII SIF ($SIF_{full}$)

Due to the multi-scattering and reabsorption effects during radiative transfer in the canopy, the SIF signal observed by sensors is only a small fraction of the total SIF and is also a mixture of the signals emitted by different photosystems (PSI and PSII). Therefore, we first partitioned the observed SIF into $SIF_{PSII}$ and $SIF_{PSI}$ using the ratio of PSII fluorescence to the PSI+PSII fluorescence given wavelength (fPSII):

$$SIF_{PSII\_obs} = SIF_{obs} \times fPSII \quad (17)$$

For the KR-TCK site, fPSII was calculated at 760 nm wavelength; for the CA-obs and US-NR1 sites, fPSII was calculated as the ratio of the integrated PSII SIF to the integrated total SIF from 745 to 758 nm. We calculated the fPSII values based on the Soil Canopy Observation of

Photosynthesis and Energy (SCOPE) model simulations considering various canopy structure conditions described by Liu et al. (2022), and obtained values of 0.6676 for the Ca-obs and US-NR1sites and 0.6481 for the KR-TCK site.

Then, to downscale the canopy-scale PSII SIF, we calculated the escape probability of SIF photons from the leaf surface to the top of the canopy (fesc) using the method proposed by Zeng et al. (2019):

$$fesc = \frac{NIRv}{fPAR} = \frac{NDVI \times NIR}{fPAR} \quad (18)$$

where NIRv is the near-infrared reflectance of vegetation, NDVI is the normalized difference vegetation index, and fPAR is the fraction of absorbed photosynthetic active radiation. This method is based on the similar radiative transfer of reflectance and emitted SIF at the near-infrared wavelengths. Upon dividing the canopy-scale SIF observations ($SIF_{PSII\_obs}$) using fesc, we obtained the total SIF signals on the leaf surface ($SIF_{PSII\_leaf}$). We then used the escape probability of the SIF photons from the photosystems to the leaf surface (fLp) to further downscale $SIF_{PSII\_leaf}$ to the total SIF at the photosystem scale ($SIF_{PSII\_ps}$). In this study, we only employed the far-red SIF and regarded fLp as a constant (approximately 0.9) according to previous studies (Liu et al., 2022; Liu et al., 2020c; Lu et al., 2020). In summary, PSII SIF at the photosystem scale ($SIF_{PSII\_ps}$) was obtained using the following equation:

$$SIF_{PSII\_ps} = \frac{SIF_{PSII\_obs}}{fesc \times fLp} \quad (19)$$

Because the wavelength of SIF emission ranged from 650 to 800 nm, but $SIF_{PSII\_ps}$ only represents the SIF signal at the specific wavelength (745 to 758 nm for CA-obs and US-NR1 site, 760 nm for the KR-TCK site), we converted $SIF_{PSII\_ps}$ to obtain the total full-band PSII SIF ($SIF_{full}$, the integration of SIF in the wavelengths from 640 to 850nm, unit: μmol/m$^2$/s) to estimate photosynthesis according to a previous study (Liu et al., 2022):

$$SIF_{full} = \sum_{\lambda=640}^{850} \left( SIF_{PSII\_ps} \times fc(\lambda) \times \frac{\lambda \times 10^6}{h \times c \times N_A \times 10^3 \times 10^9} \right) \quad (20)$$

where $fc(\lambda)$ is the conversion factor used for calculating SIF at the $\lambda$ wavelength, $h$ is the Planck constant ($6.63 \times 10^{-34}$ J·s), c is the speed of light t ($3 \times 10^8$ m/s), λ is the wavelength (nm), and $N_A$ is the Avogadro constant ($6.02 \times 10^{23}$ mol$^{-1}$). The conversion factor $fc(\lambda)$ was

436 determined by the first principal component of the PSII SIF spectrum simulations, as described
437 by Liu (2022).
438 Combing equation 17, 19, and 20, we completed the conversion of observed SIF ($SIF_{obs}$) to full-
439 band PSII SIF ($SIF_{full}$).

440 **2.6 Determination of carbon-reaction-related parameters in GPP estimations**

441 The carbon-reaction-related parameters in our MLR-based model refer to the intercellular $CO_2$
442 concentration (Ci) and the photocompensation point of $CO_2$ without dark respiration (Γ*). To
443 estimate Γ*, we followed the previously described altitude-dependent temperature function
444 (Bernacchi et al., 2001; G D Farquhar et al., 1980), and to estimate Ci, we used a method based
445 on iteration.

446 To estimate Ci, we first selected records with PAR higher than the 90$^{th}$ percentile for each day
447 and regarded the photosynthesis at that time as Rubisco-limited (the photosynthetic apparatus
448 should be light-saturated when there is abundant light; otherwise, it is wasting energy to develop
449 a high photosynthetic capacity that can seldom be reached). At this time, the actual GPP equals
450 the Rubisco-limited GPP:

451 $$J\frac{C_i-\Gamma^*}{4C_i+8\Gamma^*}=V_{cmax}\frac{C_i-\Gamma^*}{C_i+K} \quad (21)$$

452 Thus, we can calculate $V_{cmax}$ (maximum carboxylation rate) using the actual electron transport
453 rate (J) estimated using $SIF_{full}$ and other biophysical properties of plants:

454 $$V_{cmax}=\mathrm{J}\frac{C_i+K}{4C_i+8\Gamma^*}=\frac{(1+k_{df})q_L\Phi_{PSIImax}(C_i+K)}{1-\Phi_{PSIImax}(4C_i+8\Gamma^*)}SIF_{full} \quad (22)$$

455 where K is the effective Michaelis–Menten coefficient of Rubisco-limited photosynthesis,
456 which can be estimated using the Michaelis–Menten constants for the carboxylation and
457 oxygenation reactions (Farquhar et al., 1980). In this equation, K, $\Gamma^*$, and $C_i$ are daily values
458 calculated based on the average of records above the 90$^{th}$ percentile PAR, and all of their units
459 are Pa. During this process, we excluded observations with 90$^{th}$ percentile PAR below 500
460 μmol/m$^2$/s and observations obtained on cloudy days (CI < 0.5) to ensure the Rubisco-limited
461 condition; further, linear interpolation was conducted for the gap-filling of $V_{cmax}$. Then, based

on the instantaneous temperature response of $V_{cmax}$, we converted $V_{cmax}$ to $V_{cmax25}$ (Kattge and Knorr, 2007), which will be used in the following iteration process to estimate the half-hourly real-time $C_i$.

Notably, $C_i$ in Equation 22 is a daily value calculated using a method based on the theory of optimal stomatal behavior (Harrison et al., 2021) and cannot capture the light response of stomata during diurnal cycles. Therefore, we used the following iteration to estimate the real-time $C_i$ for every half-hour record for comparison:

Step 1: Set the initial $C_i = 0.7 \times C_a$, where $C_a$ stands for the ambient $CO_2$ concentration;

Step 2: Estimate the net assimilation rate $A_{net}$ (the analog of GPP minus dark respiration at the leaf scale) using the following equation:

$$A_{net} = \mathrm{J}\frac{C_i - \Gamma^*}{4C_i + 8\Gamma^*} - R_d = \frac{\left(1 + k_{df}\right) q_L \Phi_{PSIImax} (C_i - \Gamma^*)}{1 - \Phi_{PSIImax}(4C_i + 8\Gamma^*)} SIF_{full} - R_d \quad (23)$$

where Rd is the dark respiration derived from its temperature response and $R_{d25}$ (the dark respiration rate at 25 °C), and $R_{d25}$ equals $0.015 \times V_{cmax25}$.

Step 3: Estimate the stomatal conductance for $CO_2$ ($G_c$, unit: mol/m$^2$/s) according to previous studies on stomatal behavior (Wang and Leuning, 1998):

$$G_c = 0.64 \times \left(G_0 + \frac{(a-1) f_w A_{net}}{C_i \left(1 + \frac{VPD}{D_0}\right)}\right) \quad (24)$$

where $G_0$ is the residual conductance (0.01, unit: mol/m$^2$/s); a is a parameter related to $CO_2$ diffusion on the leaf surface, which is assumed to be 11; fw is related to the soil moisture and is taken as 1; VPD is the vapor pressure deficit (unit: kPa); and $D_0$ is regarded as a constant showing the stomatal sensitivity to VPD (1.5, unit: kPa).

Step 4: Update $C_i$ using the diffusion model (Ju et al., 2006):

$$C_i = C_a - \frac{A_{net}}{G_c} \quad (25)$$

By repeating Steps 2–4 until $C_i$ becomes stable, we can obtain the final half-hourly $C_i$. This

iteration was performed for every leaf group (both sunlit and shaded leaves for the two-leaf model and all leaves at different canopy depths for the layered model) to consider the impact of light conditions on gas exchange. The estimations using this method to calculate $C_i$ were labeled with the suffix "_iter".

In this study, we also used another simple method to estimate $C_i$ for comparison (Shan et al., 2021):

$$C_i = \frac{3C_a\Gamma^* - \Gamma^*\frac{1.6VPD}{\lambda} - C_a\sqrt{3\Gamma^*\frac{1.6VPD}{\lambda}}}{3\Gamma^* - \frac{1.6VPD}{\lambda}} \quad (26)$$

where $\lambda$ is a parameter describing the marginal water cost of plant carbon assimilation, and the unit of VPD in this equation is hPa. Because $\lambda$ is almost constant for a specific vegetation type, we simply used $\lambda$ = 900 in this study. Compared to the iterative method, this simple method does not consider the possible influence of light conditions on stomatal closure. The estimations using this simple λ-based method to calculate $C_i$ were labeled with the suffix "_lambda".

Finally, for comparison, we also used two empirical SIF-based GPP models to estimate GPP: one of them used the linear regression to fit the SIF—GPP relationship, and the other used a nonlinear function (quadratic function) to describe the SIF—GPP relationship. GPP estimates from the linear model are GPP_linear, and GPP estimates from the model are GPP_nonlinear.

## 3. Results

### 3.1 Performances of different SIF-based GPP estimation models

In this study, we used different strategies to describe the interaction between light and canopy structure to estimate the half-hourly (or hourly) GPP from tower-based SIF observations at three ENFs. Here, we evaluated and compared the performances of these different models, and the results are shown in Figure 1.

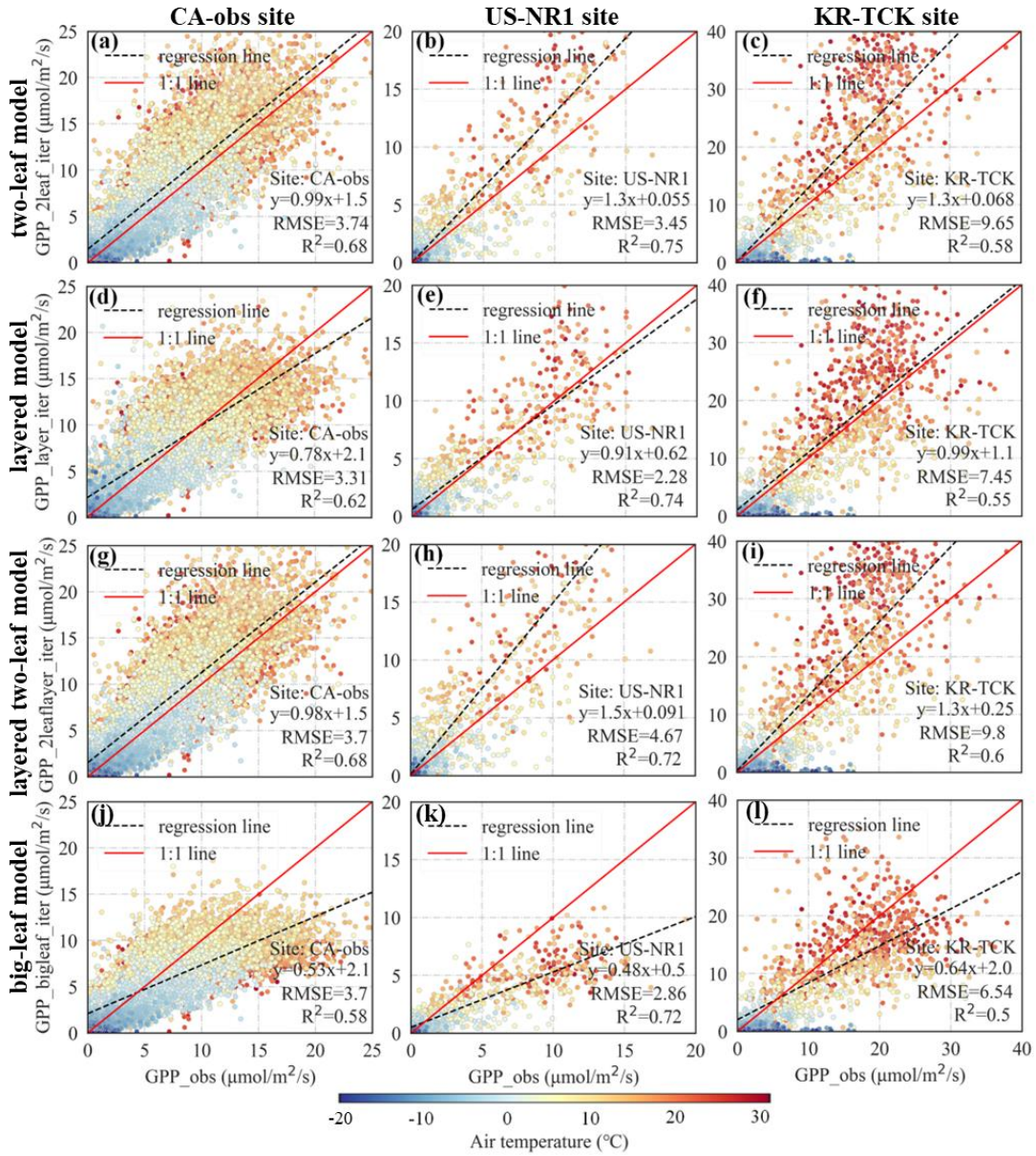


509

510 Figure 1. The performance of different models in estimating the half-hourly (or hourly) GPP.
511 Each row represents the results of different methods, and each column represents the results
512 of different ENF sites. (a)-(c), (d)-(f), (g)-(i), and (j)-(l) show the performance of the two-leaf,
513 layered, layered two-leaf, and big-leaf models, respectively. The figures in the first column show
514 the GPP estimation tested at the CA-obs site, the figures in the second column show the results
515 of the US-NR1 site, and those in the last column show the results of the KR-TCK site. All GPP
516 estimations in this figure used the iterative method to estimate Ci. The color of the dots

represents the corresponding air temperature, the dashed black line is the regression line, and the solid red line is the 1:1 line.

As displayed in the last row (Figure 1j-1l), the big-leaf model significantly underestimated GPP and had the lowest $R^2$ among the tested models. For all three sites in this study, GPP estimations from the big-leaf model exhibited a nonlinear relationship with GPP observations, and the slopes of the regression lines indicated that the big-leaf assumption would lead to approximately 45% underestimation, especially when the GPP value was high. In contrast, the models with a better description of the vertical or horizontal light distribution (including the layered model, the two-leaf model, and the layered two-leaf model) showed better performances (Figure 1a-1i), and the GPP estimates showed more linear relationships with the observed values. For the CA-obs site, the two-leaf model (Figure 1a) showed the best performance, with $R^2 = 0.68$, and a regression line close to the 1:1 line (slope:0.99); for the US-NR1 and KR-TCK sites, although the two-leaf model had high $R^2$, the layered model showed regression lines closest to the 1:1 line (for US-NR1, slope = 0.91; for KR-TCK, slope = 0.99). Compared with the results of the layered model, the GPP estimates from the two-leaf model were higher when the GPP and temperature were high (according to the distribution of scatters) and lower when the GPP and temperature were low (according to the interception of regression lines). Although the layered two-leaf model also avoided the underestimation problem and had a relatively high $R^2$, it did not show better performance than the two-leaf model at the CA-obs and US-NR1 sites and even increased the overall RMSE at the US-NR1 and KR-TCK sites. We also tested the results of different models using the simple λ-based method for $C_i$ estimation (Figure S3) and obtained similar results. In addition, we investigated the model's performance under sunny (clearness index >0.5) and cloudy conditions (clearness index <0.5) and found that the results do not change significantly (Figures S4-S5).

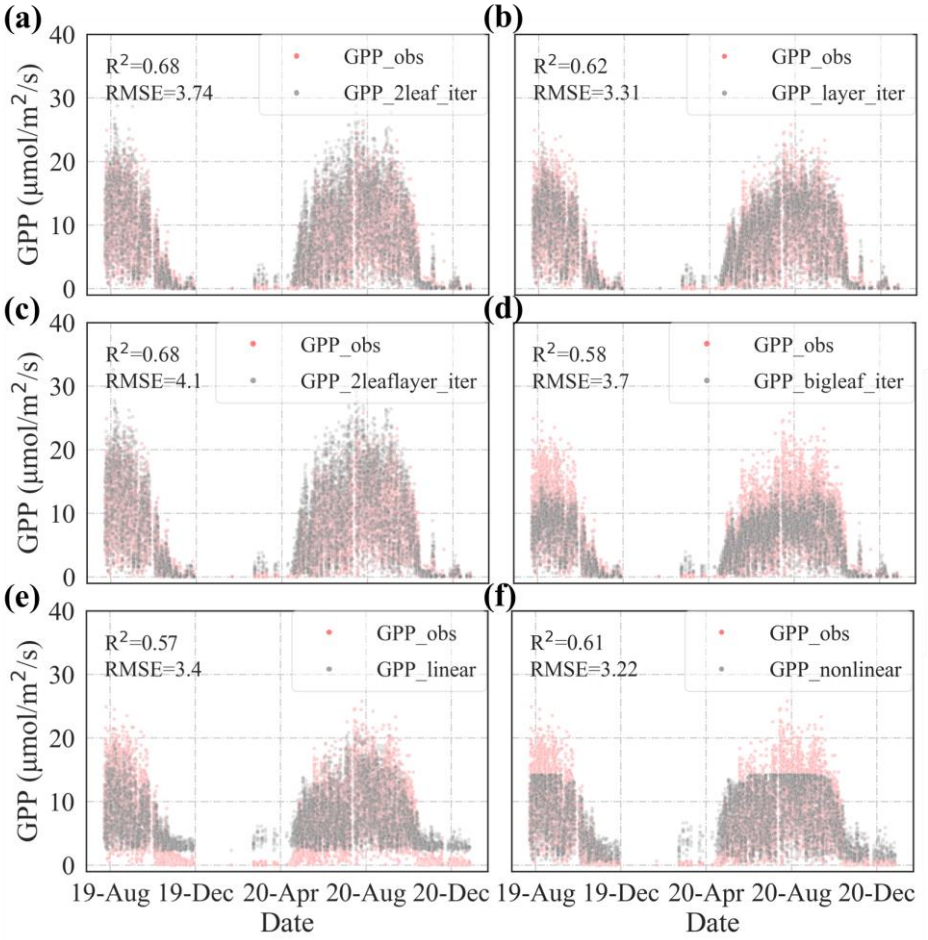


542

543 Figure 2. Time series of GPP observations and GPP estimates from the (a) two-leaf, (b) layered,
544 (c) layered two-leaf, (d) big-leaf, and (e) linear models using the empirical linear relationship
545 between SIF and GPP and from the (f) nonlinear model based on the empirical relationship
546 between SIF and GPP. The grey dots represent the half-hourly observations, and the pink dots
547 represent the GPP estimates. Here, we only displayed the results from the CA-obs site using
548 the iterative method for estimating Ci.

549
550 Figure 2 shows the time series of the observed and estimated GPP of different models. Here,
551 we can see that the two-leaf, layered, and layered two-leaf models all managed to capture the
552 dynamics of GPP observations, and there was no significant difference among their
553 performances (Figure 2a-2c). However, the big-leaf model underestimated GPP, which was
especially significant during the middays of summer (Figure 2d). In addition, empirical models

based on the empirical relationship between SIF and GPP also failed to track the dynamics of half-hourly GPP. In Figure 2e, the linear model overestimated the low GPP values during the entire study period. In Figure 3f, the nonlinear model showed truncation when the GPP estimation reached a certain value (~ 15 μmol/$m^2$/s) and thus underestimated the high GPP values in summer. Furthermore, the nonlinear model also overestimated the low GPP values, even though this overestimation problem in the nonlinear model was not as significant as that in the linear model.

Further analysis of the difference between the big-leaf and two-leaf models showed that their discrepancy was higher under conditions with high light intensity (and thereby higher GPP). Compared to environmental factors such as VPD and temperature, PAR showed the highest correlation with GPP bias (GPP estimation from the two-leaf model minus GPP estimations from the big-leaf model; $R^2$ = 0.15; Figure S3~~6~~a), whereas the GPP relative bias (obtained by dividing GPP bias by GPP values) showed a much lower correlation with PAR ($R^2$ = 0.001, Figure S6b). Similarly, the difference between the big-leaf and layered models was also highly related to incident light. In addition, while a better description of the light–structure–physiology interaction within the canopy improved the accuracy of GPP estimation (Figure 1, 2), we found that the estimation of $C_i$ did not influence the results significantly (Figure 1 vs. Figure S3). Indeed, there was a difference in the GPP estimations using different $C_i$ estimations, and it showed a high correlation with VPD, but this difference was very small. Therefore, the uncertainties caused by the change in stomatal behavior under different light conditions (which influences $C_i$) were not the most important factor influencing GPP estimation at the half-hourly scale.

### 3.2 Diurnal dynamics of GPP estimations from different models

As the intensity and angle of incident light change significantly during the day, the within-canopy illumination and its distribution vary with time, which may thereby modify the diurnal dynamics of the whole-canopy GPP and its estimation. Figure 3 shows the dynamics of the observed and estimated GPP from different models during the day (composited using all observations during the study period). Although the GPP estimations using iterative methods

to calculate $C_i$ were slightly higher than those obtained using the simple λ-based method at midday, there was high consistency in GPP estimations using different $C_i$ calculation methods (Figure 3a-d, GPP_lambda vs. GPP_iter). In contrast, the diurnal dynamics of GPP estimates from models assuming different light–structure–physiology interactions~~)~~ varied significantly. GPP estimations from both the two-leaf and layered two-leaf models tracked the bell-shaped dynamics of GPP observations (Figure 3a, 3c), but the layered model underestimated GPP at midday and overestimated GPP in the early morning and late afternoon (Figure 3b). As depicted in Figure 3d, the big-leaf model showed the most significant underestimation at midday but performed well when the light was relatively weak (before 8:00 and after 18:00). In contrast to their poor performance in Figure 2, both the empirical linear and nonlinear models tracked the diurnal dynamics of GPP well (Figure 3e, 3f), probably because they were based on the statistical relationship and were thus able to capture the "overall" pattern.

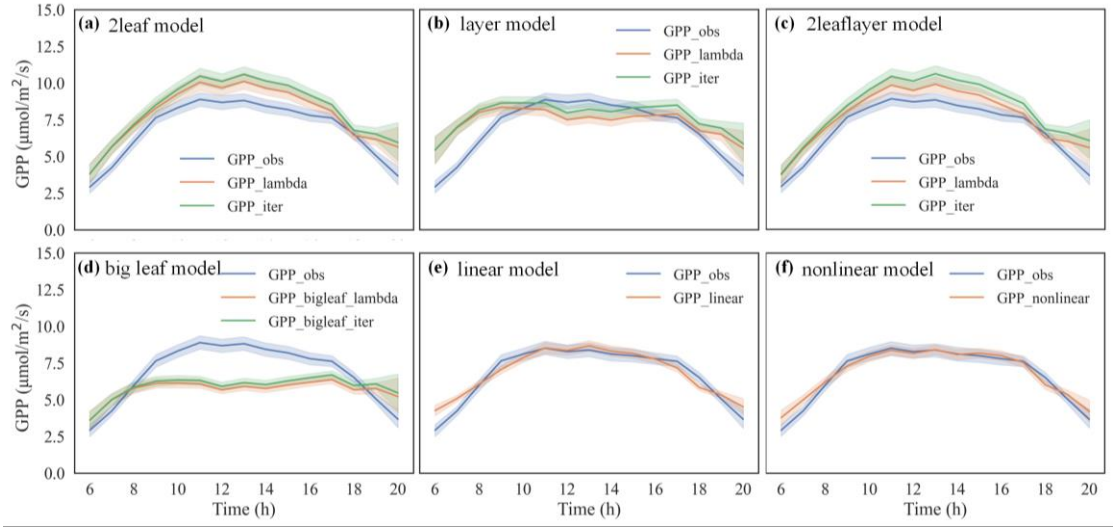


Figure 3. Diurnal dynamics of GPP observation and GPP estimates from (a) the two-leaf, (b) layered, (c) layered two-leaf, (d) big-leaf, (e) linear, and (f) nonlinear models. Variables with the suffix "_iter" refer to GPP estimation with $C_i$ estimated using the iterative method, and variables with the suffix "_lambda" refer to GPP estimation with $C_i$ estimated via the simple λ-based method. This figure shows the results from the CA-obs site using all of the half-hourly data obtained during the entire study period. The solid lines represent the average dynamics, and

the shaded areas represent 95% confidence intervals. Similar results were obtained at the other sites.

In Figure 4, we selected two sunny days during summer to further examine the differences in GPP estimations using the big-leaf model and other models. On those two days, PAR, SIF, and GPP showed "bell-shaped" patterns (Figure 4d, 4f, 4g), even though GPP had higher uncertainty and exhibited a less-smooth curve. Similar to the results in Figure 3, the layered, two-leaf, and layered two-leaf models all capture the midday increase in GPP, whereas the big-leaf model underestimated the GPP from 8:00 to 17:00 (Figure 4a-4c). This underestimation was more significant when the PAR was higher and was not significantly related to temperature changes, as exhibited in Figure 4e (because the temperature kept increasing in the afternoon, but the underestimation was weaker at that time). We further investigated the daily cycles of the estimated J/SIF ratio and J using the big-leaf model to understand the reasons for its poor performance. Figure 4h shows a significant midday reduction in the J/SIF ratio estimated by the big-leaf model, and Figure 4e indicates that the big-leaf assumption "suppressed" the ratio so strongly that even the estimated J (which equals J/SIF ratio times SIF) cannot capture the midday increase in photosynthesis.

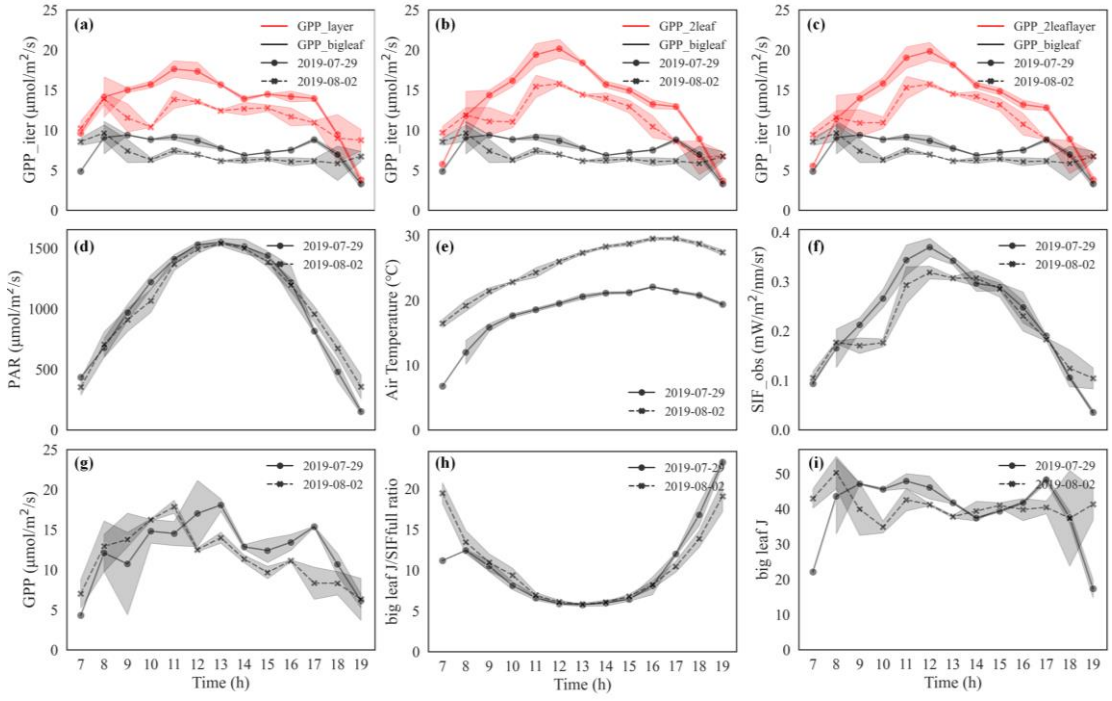


Figure 4. Comparison between the diurnal dynamics of GPP estimations from the big-leaf

model and the (a) layered, (b) two-leaf, and (c) layered two-leaf models and the corresponding (d) incident PAR, (e) temperature, (f) SIF, and (g) GPP on July 29, 2019, and August 2, 2019. (h) shows the changes in estimated J/SIF ratio, and (i) shows the dynamics of estimated J using the big-leaf model. The shaded areas represent the 95% interval. All the data used in this figure were obtained from the CA-obs half-hourly dataset.

### 3.3 Diurnal dynamics of GPP in different canopy layers (under different light conditions)

Due to the changing illumination and its distribution in the canopy, photosynthesis from different leaf groups (specifically, in different layers or under different light conditions) varies during the day, leading to the heterogeneity of GPP within the canopy. In Figure 5, we investigated the vertical variation in the diurnal dynamics of GPP estimations in each layer (depth) of the canopy to determine the reason for the midday underestimation and early morning overestimation in the layered model (as indicated in Figure 3b and 4a). Figure 5a and 5b display the estimated GPP dynamics derived from the layered model on July 29, 2019, and August 2, 2019, respectively. The results showed that the layered model successfully captured the increased GPP at noon in the bottom layers but showed a significant reduction in midday GPP in the top layers. Therefore, the discrepancy between GPP estimation from the layered model and GPP observations (Figure 3b) was mainly related to its unsatisfactory estimation in the top layers. The underestimation problem in the top layers (the top 5) was so severe that the GPP estimations even exhibited a reduction trend at noon and became smaller than the GPP estimations in the bottom layers. However, the results derived from the layered two-leaf model showed an increase in GPP at noon in both the bottom and top layers (Figure 5c and 5d). As the only difference between these two models was their assumption of light distribution, the different results in Figure 5a and 5c, 5b, and 5d indicated that the description of light–canopy–physiological interaction was important in the half-hourly GPP estimations, especially when considering the diurnal patterns of photosynthesis. The layered model assumes that all the leaves were not shaded and received direct light (even though the light decayed when it

penetrated the canopy); thus, this model may have overestimated the overall high light stress on the top leaves and "over-penalized" their qL at midday; simultaneously, because it does not consider that gaps among leaves could cause light spots in the deep canopy and high light conditions for some leaves, it might have underestimated the overall light condition in the bottom layers and thus slightly overestimated the qL and thereby GPP in the bottom layers at noon.

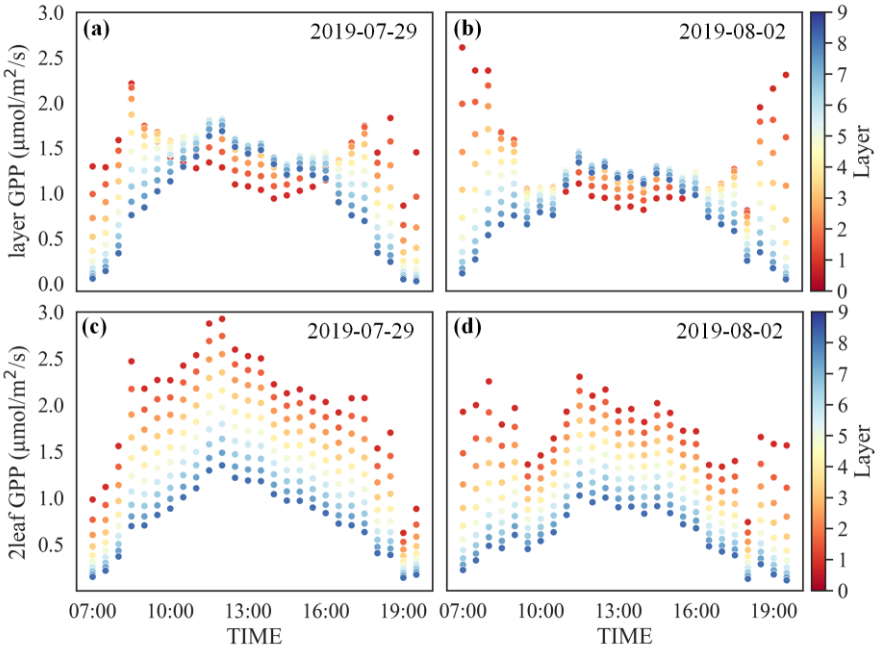


Figure 5. Diurnal dynamics of GPP estimation in different layers. The GPP estimations in (a) and (b) came from the layered model, and the GPP estimations in (c) and (d) came from the layered two-leaf model. The color of the dots represents the layer index, and a larger number represents a deeper location within the canopy. The LAI of each layer in this figure can be calculated as total LAI/10.

To investigate the dynamic distribution of GPP within the canopy, we further studied the depths of the layer above which the leaves contributed 80% of the total GPP during two sunny days (Figure 6). Using the vertical GPP estimations displayed in Figure 5, we found that both the layered and layered two-leaf models indicated that the GPP contribution at midday came from deeper layers than that in the morning or afternoon, which led to the "bell-shaped" curve in

Figure 6a and 6b. That is, the incident PAR (including direct and diffused fractions) can penetrate deeper into the canopy at noon and trigger increased photosynthesis in the bottom layer leaves. The deepest 80% GPP contribution depth estimated from the layered model is 8, which is slightly deeper than the depth of 7 from the layered two-leaf model; meanwhile, the 80% GPP contribution depths before 8:00 and after 18:00 estimated by the layered model were shallower than those estimated by the layered two-leaf model, which may relate to the lack of consideration of diffused light in the layered model.

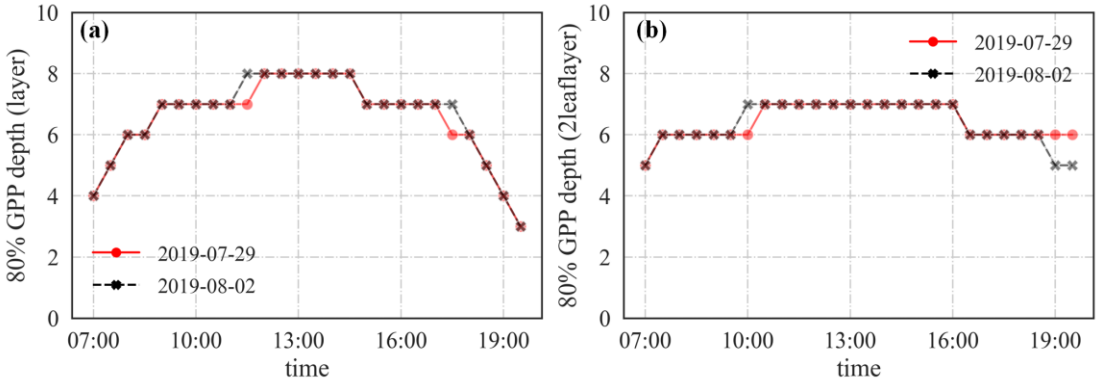


Figure 6. Depths of the layer above which the leaves contributed 80% of the total GPP on July 29, 2019, and August 2, 2019. Data used for depth estimation and plotting were half-hourly estimations from (a) the layered model and (b) the layered two-leaf model at the CA-obs site.

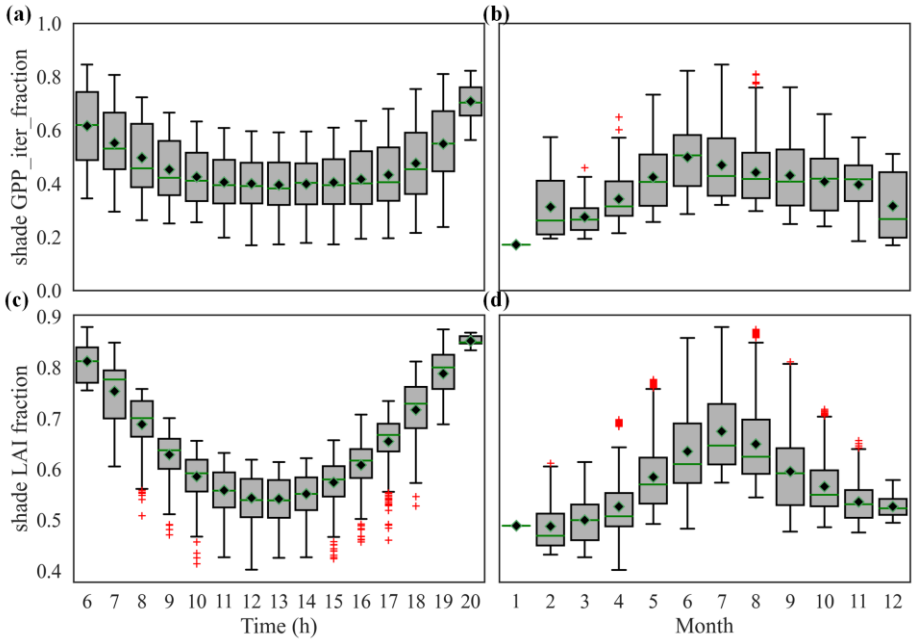

Figure 7. (a) Diurnal variation in the GPP contribution of shaded leaves; (b) seasonal variation in the GPP contribution of shaded leaves; (c) diurnal variation in the LAI fraction of shaded leaves; (d) seasonal variation in the LAI fraction of shaded leaves. The cross-marks in the plots represent the outliers, the black dots represent the mean values of each box, and the green lines represent the median values of each box.

In Figure 7a and 7b, we investigated the diurnal change in the GPP contribution of the shaded leaves and compared it with their seasonal dynamics. Here, we found that the GPP fraction from shaded leaves decreased in the morning and increased in the afternoon, while it increased from spring to summer and decreased from autumn to winter. These dynamics were consistent with the dynamics of the shaded LAI fraction at the diurnal and seasonal scales displayed in Figure 7c and 7d, respectively. These results indicate that the contribution of shaded leaves was more important in the morning and afternoon, when there was an apparent change in the solar zenith angle during the day; however, at the seasonal scale, the denser canopy led to a higher shaded LAI fraction and thus made GPP from shaded leaves (which used diffused light for photosynthesis) more crucial in summer. According to the result in Figure 7a, we deduced that the reason for the higher contribution of the bottom layers at noon in Figure 6b (compared to the morning and evening) should not only be attributed to the increase in the total intensity of diffused light but also to the direct light penetrating to the deeper layers through the gaps among leaves (indicated by the increase in the sunlit leaf fraction and reduction in the shaded leaf fraction) at midday.

### 3.4 Comparison of single-leaf qL and “canopy-scale qL”

To clarify the possible differences between single-leaf qL and canopy-scale qL, we used the framework of the big-leaf model but GPP estimations from the layered model or layered two-leaf model as input to calculate the canopy-scale qL. Figure 8 shows the different light responses of single-leaf qL (red dots), canopy-scale qL calculated from the results of the two-leaf model (pink dots), and canopy-scale qL calculated from the results of the layered model

(gray dots). Compared to the canopy-scale qL, the single-leaf qL (directly estimated using Equation 4) was more sensitive to the change in illumination and showed a faster decrease as the incident light increased. The scatterplot also showed that the distribution of canopy-scale qL from the two-leaf model was more dispersed than that of the canopy-scale qL from the layered model, which should be attributed to their different description of light–structure–physiology interactions because both of them used the same function (Equation 4) to estimate the qL of individual leaf groups.

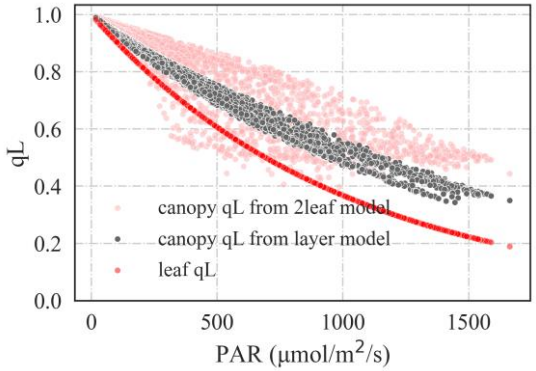


Figure 8. The light response of single-leaf qL (in red), canopy-scale qL obtained from the layered model (in gray), and canopy-scale qL from the two-leaf model (in pink). The PAR label of the x-axis refers to the incident PAR obtained at the top of the canopy.

We further investigated how LAI impacts the light response of canopy-scale qL estimated from the two-leaf model in Figure 9a (and the canopy-scale qL estimated from the layered model in Figure S7). We found that the LAI largely explained the variation in the light response of canopy qL and that a higher LAI corresponded to a less-sensitive light response of canopy qL (a less-steep slope in the relationship between qL and PAR) (Figure 9 and S5). We further compared the canopy-scale qL of sunlit leaves (using GPP of sunlit leaves) and that of shaded leaves (Figure 9b, 9c) and found that the qL of the shaded leaves showed a less-sensitive response to changes in light than sunlit leaves and that the impact of LAI on the light response of canopy-scale qL was more significant for sunlit leaves.

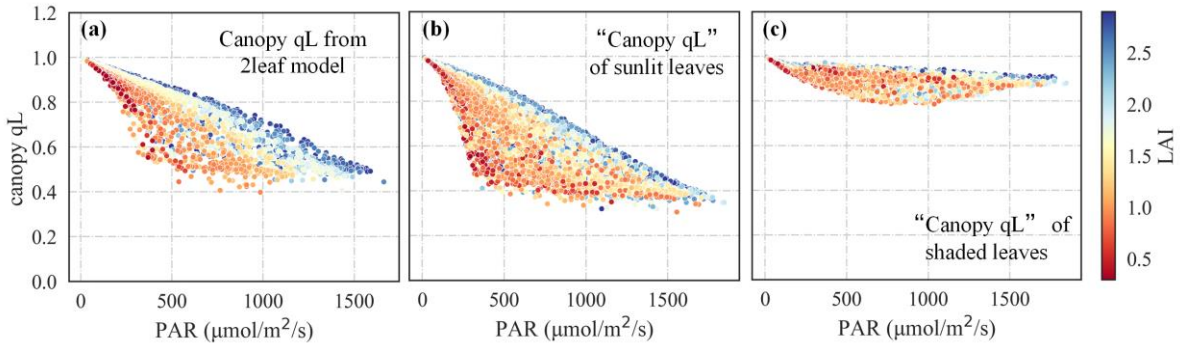


721

722 Figure 9. The impact of LAI on the light response of the (a) canopy-scale qL from the two-leaf

723 model; (b) canopy-scale qL of sunlit leaves; (c) canopy-scale qL of shaded leaves. The color of

724 the dots represents the corresponding LAI. The PAR label of the x-axis refers to the incident

725 PAR obtained at the top of the canopy.

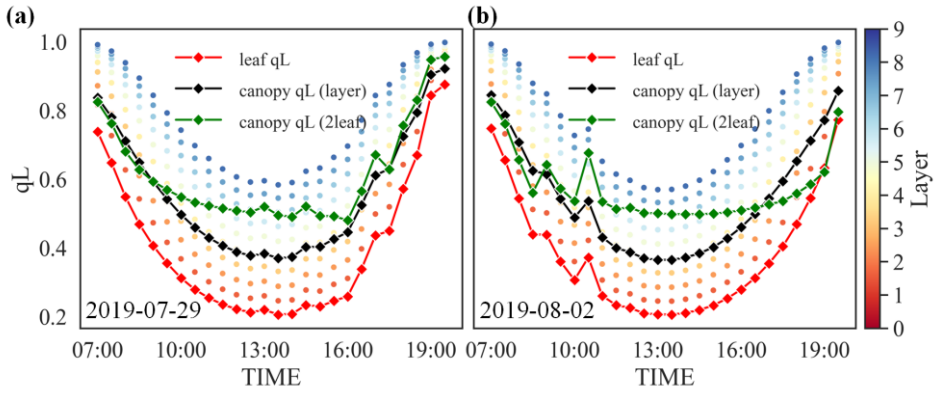


726

727 Figure 10. The diurnal patterns of single-leaf qL (red lines), canopy qL from the layered model

728 (black lines), canopy-scale qL from the two-leaf model (green lines), and the qL in different

729 layers of the canopy (colored scatters). The color of the dots represents the layer index, and

730 the larger number represents the deeper location within the canopy. The LAI of each layer in

731 this figure can be calculated as total LAI/10.

732 Using the observations from two sunny days, we compared the diurnal patterns of single-leaf

733 qL, canopy qL from the layered model, canopy-scale qL from the two-leaf model, and qL in

734 different canopy layers in Figure 10. Here, we found that the single leaf showed the same pattern

as the qL in the first layer of the canopy, with lower values than those in the other layers due to their higher light exposure (the incident PAR at the top of the canopy). The qL values in the top layers were higher than those in the bottom layers, and the difference was greater at noon. The canopy-scale qL from the layered model showed moderate qL dynamics (compared to the qL in the top and bottom layers) and was lower than the canopy-scale qL from the two-leaf model at noon. The differences in these qL dynamics indicated that the interaction between light and canopy structure (which leads to light redistribution within the canopy) could influence the dynamics of canopy-scale qL (the "overall qL") and that underestimation of GPP in big-leaf models could be mainly attributed to the utility of single-leaf qL rather than the canopy-scale qL during calculation.

## 4. Discussion

In this study, we found that employing the big-leaf assumption in the SIF-based GPP estimation would lead to significant underestimation at the half-hourly scale (Figure 1j-1l, Figure 2d), and this underestimation mainly appeared under intense light conditions (at noon), which thereby distorted the diurnal patterns of estimated GPP (Figure 3d, Figure 4a-4c). However, when the interaction of light, canopy structure, and plants' physiological factors was considered to provide a more accurate description of the light redistribution within the canopy, the accuracy of half-hourly GPP estimation could be significantly improved, and the estimation results could better capture the diurnal pattern of GPP (Figure 1a-1i, Figure 2a-2c, and Figure 3a-3c). The success of our attempt demonstrated that the unsuitable description of light–structure–physiologica interactions in the big-leaf model is responsible for the poor estimation of the J/SIF ratio (Figure 4h-4i), thereby influencing the half-hourly GPP estimation.

Due to the shading and absorption effects in the radiation transmission process, incident light is attenuated from the top to the bottom of the canopy layers and causes vertical gradients of the light condition and photosynthesis within the canopy (Chen et al., 1999; Yang et al., 2021). During diurnal cycles, variation in the combination of light intensity and incident angle leads to the redistribution of light and changes the vertical gradients, which affects the dynamics of

762 qL at different canopy depths (Chang et al., 2021). This can be proved by the simulated diurnal
763 patterns of PAR and qL (a crucial parameter in MLR-based GPP estimation models) in different
764 layers under clear sky conditions (Figures S8 and S9). To clarify the impacts of the light
765 intensity and incident angle (solar zenith angle) on the variation patterns of qL in different
766 layers, we further controlled the variation in light intensity and incident angle by fixing them
767 before the simulation and found that the dynamics of light and qL in the upper layers of the
768 canopy were mainly influenced by the daily variation pattern of light intensity, whereas those
769 in the lower layer were mainly influenced by the change in the incident angle (Figures S8 and
770 S9). We also found that the difference in qL at different depths was greater at midday (smaller
771 SZA) than in the morning and evening (larger SZA), which partly explained the more
772 significant GPP underestimation at noon (Figure S9). Therefore, the pattern of qL results from
773 interactions among light, canopy structure, and leaf physiology, which explains why
774 considering this interaction improved the GPP estimation accuracy in our research.

775 Our study demonstrated that it is important to select a proper light-canopy interaction
776 assumption when SIF is used to estimate the half-hourly GPP. The widely used big-leaf model
777 assumes that the canopy is a big foliage, and thus, all of the leaves in the canopy are considered
778 sunlit leaves and have the same physiological properties (Gu et al., 2019; Liu et al., 2022).
779 Therefore, all the leaves in the canopy are considered to be under high-light conditions and
780 even in a photoinhibition state at midday in summer. As there is a monotonical negative
781 correlation between qL and light intensity (Han et al., 2022a; Liu et al., 2021), this assumption
782 would make the qL “over-penalized” at noon, which causes underestimation of the high GPP
783 values. In comparison, the layered model determines the light levels at different depths so that
784 not all leaves are assumed to be in a high-light intensity state; thus, it improves the estimation
785 accuracy and is more consistent with reality. The two-leaf model further counts the effects of
786 direct light, diffused light, and the clumping condition of leaves to improve the model’s
787 accuracy. As the model assumes that only a fraction of leaves receives high-intensity direct
788 light and that many other leaves are under milder diffused light, it describes the real condition
789 well and can avoid significant underestimation under high-light conditions.

790 The two-leaf model and layered two-leaf model should be attributed to the merit of two-leaf

assumptions; however, we used this assumption here differently from that in previous studies. The two-leaf assumption has been applied in light use efficiency (LUE) photosynthetic modules integrated into terrestrial ecosystem models (e.g., BEPS models) or SIF simulation models in previous studies (Cui et al., 2020; Liu et al., 1997) and has been demonstrated to perform well (Zheng et al., 2020). Previous LUE models used different LUEs to describe the different physiological characteristics of sunlit and shaded leaves, and the LUE values ($LUE_{shade}$ and $LUE_{sun}$) were mostly obtained from calibration or empirical results. As the variations in the angle and intensity of incident light during the day alter the amount of light penetrating the lower canopy and lead to highly dynamic overall light conditions, the determination of $LUE_{shade}$ and $LUE_{sun}$ (which respond to the light condition) without the support of clear mechanisms will introduce uncertainty in the results. In contrast, our method contains a clear mechanistic expression of the SIF-GPP relationship. Except for the physiological information included in the SIF signal, we mainly used qL to capture the differences in the physiological properties of shaded and sunlit leaves. Because the difference in qL between shaded and sunlit leaves can be calculated directly using their incident light, our model can show the difference in the physiological characteristics of shaded and sunlit leaves more clearly and directly; thus, it can consider the fertilization effect of diffused light without the need for calibration. We acknowledge that other physiological factors may also contribute to the different photosynthetic capacities between sunlit and shaded leaves, but we do not consider these contributions in this study. Nevertheless, recent studies have proven the importance of considering the impact of light on LUE (Guan et al., 2022, 2021), and the good performance of their modified LUE model with radiation scalar confirmed that the differences in LUE between sunlit and shaded leaves are mainly caused by the differences in light conditions, which means that consideration of light impacts should be good enough to provide relatively accurate estimations.

Even though physiological differences remain between sunlit and shaded leaves that were not considered in this study, they may influence the performance of two-leaf models. As the different micro-environments and long-term adaptation may cause differences in physiological properties (such as the light response) of sunlit and shaded leaves, we evaluated this effect by using different qL light response curves in sunlit and shaded leaves (Chang et al., 2021) and

found that it did not significantly influence our results (Figure S10a,b vs. Figure 1a). In addition, we tried to assign SIF using APAR without considering the different physiological signals of sunlit and shaded leaves (sunlit ΦF vs. shaded ΦF), and we found that the effect was not significant (Figure S10c vs. Figure 1a). This result suggests that the differences or estimation uncertainty in the physiological signals in SIF (ΦF) do not significantly affect the GPP estimation from the two-leaf model, whereas the difference in qL matters.

Unlike other models proposed in this study, the big-leaf model directly uses the single-leaf qL to estimate GPP. However, the canopy-scale qL obtained from the relatively accurate GPP estimations in our study showed a lower sensitivity to incident light than the single-leaf qL (Figures 8 and 10). The light response of canopy-scale qL is influenced by LAI, but when the canopy density decreases (with low LAI), it is closer to the single-leaf pattern (Figures 8, 9a). Therefore, we deduce that the big-leaf assumption might be more acceptable for sparser canopies with simple structures but not for dense canopies with complex structures. In addition, as the light response of canopy-scale qL is too complicated to be described by merely one function (Figures 8 and 9), it might be inefficient to simply correct the leaf-scale response function (or even use another function type) and then apply it at the canopy scale. This result is echoed by a previous study showing depression in fluorescence at the leaf level but not in the canopy of a pine forest (Louis et al., 2006). In that study, the canopy structure also impacts the canopy-scale pattern by modulating the light penetrating into deeper canopy layers.

Although models with an improved description of the light–structure–physiology interactions in our study performed well in capturing the diurnal dynamics of GPP, we have to admit that there are still some uncertainties. First, we used satellite-based LAI rather than ground observations collected at each site in our study. The possible mismatch or error in these satellite data may affect the accuracy of GPP estimation. To clarify these problems, we replaced the GLASS LAI with the ground LAI measurement at the KR-TCK site (only this site had ground observation of LAI) and found that this did not significantly influence GPP estimation (Figure S11). Second, there were uncertainties in the satellite-based Ω dataset. Therefore, we also tested another satellite clumping index dataset at the CA-obs site and found that although there were differences in the clumping index results, this discrepancy was not passed down to the model

outputs (Figure S10d vs. Figure 1a). Third, although the comparison between Figure 1 and Figure S3 demonstrated that the methods used to estimate $C_i$ and the consideration of light response of stomatal behaviors do not introduce much difference in GPP estimation, and the iterative method still slightly increased the accuracy. Third, for the layered model, the number of layers (n) also influences the model performance, and we found that the increase in layer numbers increased the $R^2$, RMSE, and regression slope but reduced the regression interception of the relationship between the observed and estimated GPP (Figure S12). However, when the number of layers was greater than 320, it no longer impacted the accuracy of GPP estimation. For the layered model using the interactive method to estimate $C_i$, $R^2$ dropped significantly as the number of layers continued to increase after reaching 80, but this phenomenon was not found in the layered model using the simple λ-based method. This result indicated that using the interactive method makes the model more sensitive to uncertainties in SIF (SIF in each layer has larger uncertainty as the number of layers increases), even though it had a higher $R^2$ compared to the simple λ-based method. Finally, although we employed the widely accepted Lambert–Beer's law and the method proposed by Chen et al. (1999), uncertainty remains in the description of vertical variation in light. For the quantification of such uncertainty, we employed the 3-D Discrete Anisotropic Radiative Transfer Model (DART) to validate the PAR estimation in each layer for three different scenes (Appendix A). The results demonstrated the effectiveness of Lambert–Beer's law in describing the vertical profile of PAR for ENF sites ($R^2$ higher than 0.9; Figures A1, A2). However, the results also indicated that violating the canopy homogenous assumption in the real world would undermine the effectiveness of Lambert–Beer's law, leading to a less-credible estimation of light distribution in relatively sparse and highly heterogeneous canopies. Nevertheless, the key point of this study is to highlight the importance of considering vertical light distribution when using SIF to estimate GPP. Although we only used the 1-D radioactive transfer models and highly simplified the canopy structure in this study, the GPP estimates still showed high consistency with the GPP observation. In the future, combining 3-D models and Lidar measurements would enable a more accurate estimation of the PAR profile, thereby assisting in a more accurate estimation of GPP via SIF.

There are also some limitations in our study. Although the layered model and two-leaf model

878 considered the vertical and horizontal heterogeneity of light conditions and leaf biophysical
879 properties (mainly the redox state of PSII reaction centers indicated by qL), they do not indicate
880 that we thoroughly considered the variations in leaf biophysical properties. The inherent
881 differences in leaves (for example, age, status, and nutrient conditions) were not considered. In
882 this study, we used the empirical relationship between PAR and qL; however, previous studies
883 have shown that temperature could also influence qL (Han et al., 2021). We could not consider
884 the impacts of temperature heterogeneity or other environmental factors within the canopy,
885 mainly because of the lack of a modeled relationship between qL and temperature and the
886 difficulty in obtaining the temperature distribution in canopies. This might make the models
887 incapable of reproducing photoinhibition under high temperatures, which probably explains the
888 decreased GPP in the afternoon of August 2, 2019, at the CA-obs site (Figure 4g). In addition,
889 none of the models in our study considered the contribution of understory species, but they are
890 important for the total photosynthesis of the whole ecosystem (Nunes et al., 2022). As there are
891 many non-photosynthetic organisms (such as branches and trunks) that block light transmission
892 within the canopy, the woody fraction, the space among trees, and the orientation of the terrain
893 slope are also issues that need further consideration (Chang et al., 2021).

894 **5. Conclusion**

895 In this study, we developed SIF-based GPP estimation models with different descriptions of
896 light–structure–physiological interactions, including a layered model, a two-leaf model, and a
897 layered two-leaf model. We compared their performances with the big-leaf model on a half-
898 hourly scale at three ENF sites. The results showed that the big-leaf model significantly
899 underestimated the half-hourly GPP. The underestimation mainly occurred at midday, which
900 distorted the diurnal dynamics of the estimated GPP. In contrast, the layered model, two-leaf
901 model, and layered two-leaf model all improved the estimation accuracy. Compared with the
902 layered model, both the two-leaf model and the layered two-leaf model showed daily patterns
903 closer to reality, with no significant differences between them. We further investigated the
904 diurnal dynamics of GPP and qL in different layers and found that the big-leaf and layered
905 assumptions overestimated the overall light stress at noon and thus “over-penalized” qL,

leading to the underestimation of GPP. In the morning and afternoon, the leaves on the top layers of the canopy contributed significantly to the total GPP, but as the solar zenith angle decreased at noon, leaves from the deeper layers also played an important role. Finally, by comparing the single-leaf scale qL with the canopy-scale qL (obtained from relatively accurate GPP estimations), we demonstrated that the canopy-scale qL was less sensitive to light than the single-leaf scale qL and that the difference was larger for the shaded leaf group or when the LAI was high.

## Appendix

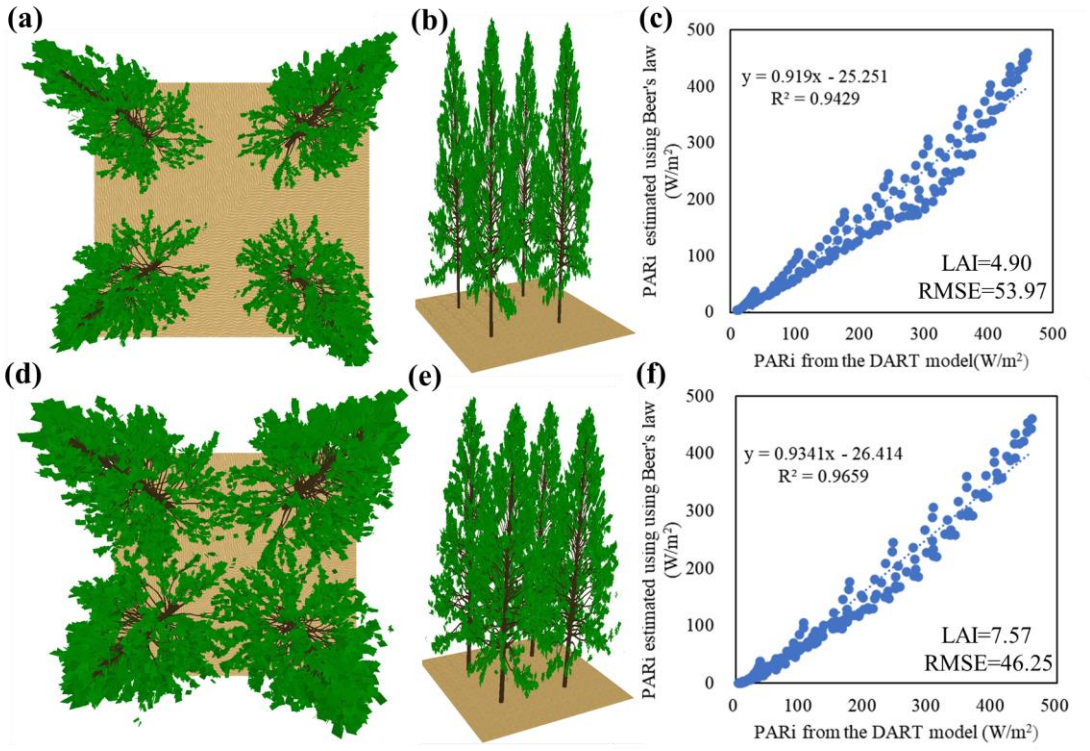


Figure A1. The nadir view (a, d) and the side view (b, e) of the 3-D scene, and the accuracy of $PAR_i$ estimated using Lambert–Beer's law (c, f). The method was examined in canopies with different densities. Canopies were divided into 16 layers, and the PAR in each layer ($PAR_i$ for layer i) was calculated when SZA =0°, 9°, 18°, 27°, 36°, 45°, 54°, 63°, 81°. (a-c) shows the condition in a relatively sparse canopy, and (d-f) shows the condition in a dense canopy.

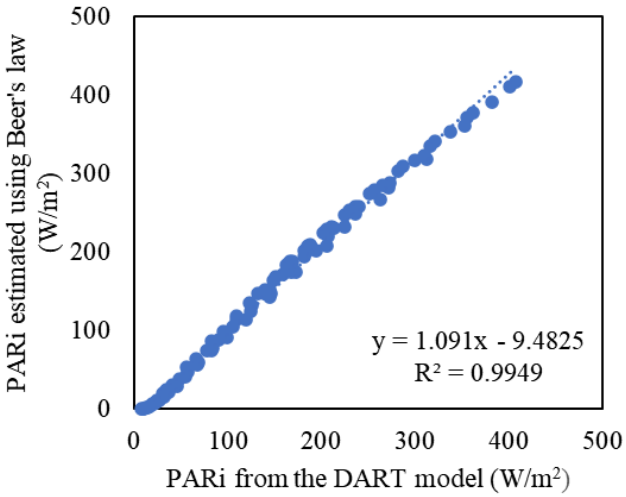


Figure A2. The accuracy of $PAR_i$ estimated using Lambert–Beer's law in a turbid canopy (more homogenous; LAI=2). PAR in each layer ($PAR_i$ for layer i) was calculated when SZA =0°, 9°, 18°, 27°, 36°, 45°, 54°, 63°, 81°.

## Conflicts of interest

The authors declare that they have no conflict of interest.

## Acknowledgement

We appreciate Prof. Juliane Bendig from Institute of Bio- and Geosciences, Plant Sciences, Forschungszentrum Jülich GmbH, Prof. Zbynek Malenovsky, Dr. Omar Regaieg, and Dr. Thang Nguyen from University of Bonn for their kind help in the technical details in the application of DART model. We also thanks Prof. Troy Magney from the University of California Davis, Dr Zoe Pierrat and Prof. Jochen Stutz from the University of California, Los Angeles, and Prof. Youngryel Ryu, Prof. Hyun Seok Kim from Seoul National University, and Dr. Jongmin Kim from University of Virginia, for they recommended datasets with high-quality. This research was funded by the National Natural Science Foundation of China (42071310)~~the Innovative Research Program of the International Research Center of Big Data for Sustainable Development Goals (CBAS2022IRP01)~~ and ~~the National Natural Science Foundation of China (42071310)~~ the Innovative Research Program of the International Research Center of Big Data

for Sustainable Development Goals (CBAS2022IRP01).

## References


Anav, A., Friedlingstein, P., Beer, C., Ciais, P., Harper, A., Jones, C., Murray-Tortarolo, G., Papale, D., Parazoo, N.C., Peylin, P., Piao, S., Sitch, S., Viovy, N., Wiltshire, A., Zhao, M., 2015. Spatiotemporal patterns of terrestrial gross primary production: A review. Rev. Geophys. https://doi.org/10.1002/2015RG000483

Barr, A.G., Black, T.A., Hogg, E.H., Kljun, N., Morgenstern, K., Nesic, Z., 2004. Inter-annual variability in the leaf area index of a boreal aspen-hazelnut forest in relation to net ecosystem production. Agric. For. Meteorol. https://doi.org/10.1016/j.agrformet.2004.06.011

Bernacchi, C.J., Singsaas, E.L., Pimentel, C., Portis, A.R., Long, S.P., 2001. Improved temperature response functions for models of Rubisco-limited photosynthesis. Plant, Cell Environ. https://doi.org/10.1046/j.1365-3040.2001.00668.x

Cai, W., Yuan, W., Liang, S., Zhang, X., Dong, W., Xia, J., Fu, Y., Chen, Y., Liu, D., Zhang, Q., 2014. Improved estimations of gross primary production using satellite-derived photosynthetically active radiation. J. Geophys. Res. Biogeosciences. https://doi.org/10.1002/2013JG002456

Chang, C.Y., Wen, J., Han, J., Kira, O., LeVonne, J., Melkonian, J., Riha, S.J., Skovira, J., Ng, S., Gu, L., Wood, J.D., Näthe, P., Sun, Y., 2021. Unpacking the drivers of diurnal dynamics of sun-induced chlorophyll fluorescence (SIF): Canopy structure, plant physiology, instrument configuration and retrieval methods. Remote Sens. Environ. 265. https://doi.org/10.1016/j.rse.2021.112672

Chen, J.M., Liu, J., Cihlar, J., Goulden, M.L., 1999. Daily canopy photosynthesis model through temporal and spatial scaling for remote sensing applications. Ecol. Modell. 124, 99–119. https://doi.org/10.1016/s0304-3800(99)00156-8

Chen, R., Liu, L., Liu, X., 2022a. Leaf chlorophyll contents dominates the seasonal dynamics of SIF/GPP ratio: Evidence from continuous measurements in a maize field. Agric. For. Meteorol. 323, 109070. https://doi.org/10.1016/j.agrformet.2022.109070

964 Chen, R., Liu, X., Chen, J., Du, S., Liu, L., 2022b. Solar-induced chlorophyll fluorescence imperfectly
965 tracks the temperature response of photosynthesis in winter wheat. J. Exp. Bot. erac388.
966 https://doi.org/10.1093/jxb/erac388

967 Ciais, P., Reichstein, M., Viovy, N., Granier, A., Ogée, J., Allard, V., Aubinet, M., Buchmann, N.,
968 Bernhofer, C., Carrara, A., Chevallier, F., De Noblet, N., Friend, A.D., Friedlingstein, P.,
969 Grünwald, T., Heinesch, B., Keronen, P., Knohl, A., Krinner, G., Loustau, D., Manca, G.,
970 Matteucci, G., Miglietta, F., Ourcival, J.M., Papale, D., Pilegaard, K., Rambal, S., Seufert, G.,
971 Soussana, J.F., Sanz, M.J., Schulze, E.D., Vesala, T., Valentini, R., 2005. Europe-wide reduction
972 in primary productivity caused by the heat and drought in 2003. Nature 437, 529–533.
973 https://doi.org/10.1038/nature03972

974 Cui, T., Sun, R., Xiao, Z., Liang, Z., Wang, J., 2020. Simulating spatially distributed solar-induced
975 chlorophyll fluorescence using a BEPS-SCOPE coupling framework. Agric. For. Meteorol. 295,
976 108169. https://doi.org/10.1016/j.agrformet.2020.108169

977 Damm, A., Guanter, L., Paul-Limoges, E., van der Tol, C., Hueni, A., Buchmann, N., Eugster, W.,
978 Ammann, C., Schaepman, M.E., 2015. Far-red sun-induced chlorophyll fluorescence shows
979 ecosystem-specific relationships to gross primary production: An assessment based on
980 observational and modeling approaches. Remote Sens. Environ.
981 https://doi.org/10.1016/j.rse.2015.06.004

982 Du, S., Liu, L., Liu, X., Hu, J., 2017. Response of canopy solar-induced chlorophyll fluorescence to the
983 absorbed photosynthetically active radiation absorbed by chlorophyll. Remote Sens. 9, 911.

984 Farquhar, G. D., von Caemmerer, S., Berry, J.A., 1980. A biochemical model of photosynthetic CO2
985 assimilation in leaves of C3 species. Planta 149, 78–90. https://doi.org/10.1007/BF00386231

986 Farquhar, G D, von Caemmerer, S., Berry, J.A., 1980. A biochemical model of photosynthetic
987 CO<Subscript>2</Subscript> assimilation in leaves of C<Subscript>3</Subscript> species.
988 Planta.

989 Feng, H., Xu, T., Liu, L., Zhou, S., Zhao, J., Liu, S., Xu, Z., Mao, K., He, X., Zhu, Z., Chai, L., 2021.
990 Modeling transpiration with sun- induced chlorophyll fluorescence observations via carbon-

water coupling methods. Remote Sens. https://doi.org/10.3390/rs13040804

Friedlingstein, P., O'Sullivan, M., Jones, M.W., Andrew, R.M., Hauck, J., Olsen, A., Peters, G.P., Peters, W., Pongratz, J., Sitch, S., Le Quéré, C., Canadell, J.G., Ciais, P., Jackson, R.B., Alin, S., Aragão, L.E.O.C., Arneth, A., Arora, V., Bates, N.R., Becker, M., Benoit-Cattin, A., Bittig, H.C., Bopp, L., Bultan, S., Chandra, N., Chevallier, F., Chini, L.P., Evans, W., Florentie, L., Forster, P.M., Gasser, T., Gehlen, M., Gilfillan, D., Gkritzalis, T., Gregor, L., Gruber, N., Harris, I., Hartung, K., Haverd, V., Houghton, R.A., Ilyina, T., Jain, A.K., Joetzjer, E., Kadono, K., Kato, E., Kitidis, V., Korsbakken, J.I., Landschützer, P., Lefèvre, N., Lenton, A., Lienert, S., Liu, Z., Lombardozzi, D., Marland, G., Metzl, N., Munro, D.R., Nabel, J.E.M.S., Nakaoka, S.I., Niwa, Y., O'Brien, K., Ono, T., Palmer, P.I., Pierrot, D., Poulter, B., Resplandy, L., Robertson, E., Rödenbeck, C., Schwinger, J., Séférian, R., Skjelvan, I., Smith, A.J.P., Sutton, A.J., Tanhua, T., Tans, P.P., Tian, H., Tilbrook, B., Van Der Werf, G., Vuichard, N., Walker, A.P., Wanninkhof, R., Watson, A.J., Willis, D., Wiltshire, A.J., Yuan, W., Yue, X., Zaehle, S., 2020. Global Carbon Budget 2020. Earth Syst. Sci. Data. https://doi.org/10.5194/essd-12-3269-2020

Grossmann, K., Frankenberg, C., Magney, T.S., Hurlock, S.C., Seibt, U., Stutz, J., 2018. Remote Sensing of Environment PhotoSpec : A new instrument to measure spatially distributed red and far- red Solar-Induced Chlorophyll Fluorescence. Remote Sens. Environ. 216, 311–327. https://doi.org/10.1016/j.rse.2018.07.002

Gu, L., Han, J., Wood, J.D., Chang, C.Y.Y., Sun, Y., 2019. Sun-induced Chl fluorescence and its importance for biophysical modeling of photosynthesis based on light reactions. New Phytol. 223, 1179–1191. https://doi.org/10.1111/nph.15796

Guan, X., Chen, J.M., Shen, H., Xie, X., 2021. A modified two-leaf light use efficiency model for improving the simulation of GPP using a radiation scalar. Agric. For. Meteorol. 307, 108546. https://doi.org/10.1016/j.agrformet.2021.108546

Guan, X., Chen, J.M., Shen, H., Xie, X., Tan, J., 2022. Comparison of big-leaf and two-leaf light use efficiency models for GPP simulation after considering a radiation scalar. Agric. For. Meteorol. 313, 108761. https://doi.org/10.1016/j.agrformet.2021.108761

Guanter, L., Bacour, C., Schneider, A., Aben, I., Kempen, T.A. Van, Retscher, C., Köhler, P., Frankenberg, C., Joiner, J., 2021. Sentinel-5P TROPOMI mission 202104, 1–27.

Han, J., Chang, C.Y., Gu, L., Zhang, Y., Meeker, E.W., Magney, T.S., Walker, A.P., Wen, J., Kira, O., McNaull, S., Sun, Y., 2022a. The physiological basis for estimating photosynthesis from Chl a fluorescence. New Phytol. https://doi.org/10.1111/nph.18045

Han, J., Chang, C.Y.Y., Gu, L., Zhang, Y., Meeker, E.W., Magney, T.S., Walker, A.P., Wen, J., Kira, O., McNaull, S., Sun, Y., 2022b. The physiological basis for estimating photosynthesis from Chla fluorescence. New Phytol. https://doi.org/10.1111/nph.18045

Han, J., Gu, L., Warren, J.M., Guha, A., Mclennan, D.A., Zhang, W., Zhang, Y., 2021. The roles of photochemical and non-photochemical quenching in regulating photosynthesis depend on the phases of fluctuating light conditions. Tree Physiol. 1–14. https://doi.org/10.1093/treephys/tpab133

Harrison, S.P., Cramer, W., Franklin, O., Prentice, I.C., Wang, H., Brännström, Å., de Boer, H., Dieckmann, U., Joshi, J., Keenan, T.F., Lavergne, A., Manzoni, S., Mengoli, G., Morfopoulos, C., Peñuelas, J., Pietsch, S., Rebel, K.T., Ryu, Y., Smith, N.G., Stocker, B.D., Wright, I.J., 2021. Eco-evolutionary optimality as a means to improve vegetation and land-surface models. New Phytol. 231, 2125–2141. https://doi.org/10.1111/nph.17558

He, M., Ju, W., Zhou, Y., Chen, J., He, H., Wang, S., Wang, H., Guan, D., Yan, J., Li, Y., Hao, Y., Zhao, F., 2013. Development of a two-leaf light use efficiency model for improving the calculation of terrestrial gross primary productivity. Agric. For. Meteorol. 173, 28–39. https://doi.org/10.1016/j.agrformet.2013.01.003

Helm, L.T., Shi, H., Lerdau, M.T., Yang, X., 2020. Solar-induced chlorophyll fluorescence and short-term photosynthetic response to drought. Ecol. Appl. 30, 1–12. https://doi.org/10.1002/eap.2101

Jiao, Z., Dong, Y., Schaaf, C.B., Chen, J.M., Román, M., Wang, Z., Zhang, H., Ding, A., Erb, A., Hill, M.J., Zhang, X., Strahler, A., 2018. An algorithm for the retrieval of the clumping index (CI) from the MODIS BRDF product using an adjusted version of the kernel-driven BRDF model. Remote Sens. Environ. https://doi.org/10.1016/j.rse.2018.02.041

1045 Joiner, J., Yoshida, Y., Guanter, L., Middleton, E.M., 2016. New methods for retrieval of chlorophyll
1046 red fluorescence from hyper-spectral satellite instruments: simulations and application to GOME-
1047 2 and SCIAMACHY. Atmos. Meas. Tech. Discuss. https://doi.org/10.5194/amt-2015-387

1048 Joiner, J., Yoshida, Y., Vasilkov, A.P., Yoshida, Y., Corp, L.A., Middleton, E.M., 2011. First
1049 observations of global and seasonal terrestrial chlorophyll fluorescence from space.
1050 Biogeosciences. https://doi.org/10.5194/bg-8-637-2011

1051 Ju, W., Chen, J.M., Black, T.A., Barr, A.G., Liu, J., Chen, B., 2006. Modelling multi-year coupled
1052 carbon and water fluxes in a boreal aspen forest. Agric. For. Meteorol.
1053 https://doi.org/10.1016/j.agrformet.2006.08.008

1054 Jung, M., Koirala, S., Weber, U., Ichii, K., Gans, F., Camps-Valls, G., Papale, D., Schwalm, C.,
1055 Tramontana, G., Reichstein, M., 2019. The FLUXCOM ensemble of global land-atmosphere
1056 energy fluxes. Sci. Data. https://doi.org/10.1038/s41597-019-0076-8

1057 Kattge, J., Knorr, W., 2007. Temperature acclimation in a biochemical model of photosynthesis: A
1058 reanalysis of data from 36 species. Plant, Cell Environ. https://doi.org/10.1111/j.1365-
1059 3040.2007.01690.x

1060 Kim, J., Ryu, Y., Dechant, B., Lee, H., Kim, H.S., Kornfeld, A., Berry, J.A., 2021a. Solar-induced
1061 chlorophyll fluorescence is non-linearly related to canopy photosynthesis in a temperate
1062 evergreen needleleaf forest during the fall transition. Remote Sens. Environ. 258, 112362.
1063 https://doi.org/10.1016/j.rse.2021.112362

1064 Kim, J., Ryu, Y., Dechant, B., Lee, H., Seok, H., Kornfeld, A., Berry, J.A., 2021b. Solar-induced
1065 chlorophyll fluorescence is non-linearly related to canopy photosynthesis in a temperate
1066 evergreen needleleaf forest during the fall transition. Remote Sens. Environ. 258, 112362.
1067 https://doi.org/10.1016/j.rse.2021.112362

1068 Li, X., Xiao, J., 2020. Global climatic controls on interannual variability of ecosystem productivity:
1069 Similarities and differences inferred from solar-induced chlorophyll fluorescence and enhanced
1070 vegetation index. Agric. For. Meteorol. 288–289, 108018.
1071 https://doi.org/10.1016/j.agrformet.2020.108018

Li, Y., Fang, H., 2022. Real-Time Software for the Efficient Generation of the Clumping Index and Its Application Based on the Google Earth Engine. Remote Sens. 14, 3837.

Liu, J., Chen, J.M., Cihlar, J., Park, W.M., 1997. A process-based boreal ecosystem productivity simulator using remote sensing inputs. Remote Sens. Environ. https://doi.org/10.1016/S0034-4257(97)00089-8

Liu, L., Guan, L., Liu, X., 2017. Agricultural and Forest Meteorology Directly estimating diurnal changes in GPP for C3 and C4 crops using far-red sun-induced chlorophyll fluorescence. Agric. For. Meteorol. 232, 1–9. https://doi.org/10.1016/j.agrformet.2016.06.014

Liu, L., Liu, X., Chen, J., Du, S., Ma, Y., Qian, X., Chen, S., Peng, D., 2020. Estimating Maize GPP using Near-infrared Radiance of Vegetation. Sci. Remote Sens. 2, 100009. https://doi.org/10.1016/j.srs.2020.100009

Liu, X., Liu, L., Hu, J., Guo, J., Du, S., 2020. Improving the potential of red SIF for estimating GPP by downscaling from the canopy level to the photosystem level. Agric. For. Meteorol. 281, 107846. https://doi.org/10.1016/j.agrformet.2019.107846

Liu, X., Liu, Z., Liu, L., Lu, X., Chen, J., Du, S., Zou, C., 2021. Modelling the influence of incident radiation on the SIF-based GPP estimation for maize. Agric. For. Meteorol. 307, 108522. https://doi.org/10.1016/j.agrformet.2021.108522

Liu, Z., Zhao, F., Liu, X., Yu, Q., Wang, Y., Peng, X., Cai, H., Lu, X., 2022. Direct estimation of photosynthetic CO2 assimilation from solar-induced chlorophyll fluorescence (SIF). Remote Sens. Environ. 271, 112893. https://doi.org/10.1016/j.rse.2022.112893

Lu, X., Liu, Z., Zhao, F., Tang, J., 2020. Comparison of total emitted solar-induced chlorophyll fluorescence (SIF) and top-of-canopy (TOC) SIF in estimating photosynthesis. Remote Sens. Environ. https://doi.org/10.1016/j.rse.2020.112083

Luijkx, I., Velde, I.R., Krol, M., Gatti, L., Domingues, L., S. C. Correia, C., Miller, J., Gloor, M., Leeuwen, T., Kaiser, J., Wiedinmyer, C., Basu, S., Clerbaux, C., Peters, W., 2015. Response of the Amazon carbon balance to the 2010 drought derived with CarbonTracker South America. Global Biogeochem. Cycles 29. https://doi.org/10.1002/2014GB005082

Magney, T.S., Barnes, M.L., Yang, X., 2020. On the Covariation of Chlorophyll Fluorescence and Photosynthesis Across Scales. Geophys. Res. Lett. 47, e2020GL091098. https://doi.org/10.1029/2020GL091098

Magney, Troy S, Bowling, D.R., Logan, B., Grossmann, K., Stutz, J., Blanken, P., 2019. Mechanistic evidence for tracking the seasonality of photosynthesis with solar-induced fluorescence. Proc. Natl. Acad. Sci. In Press. https://doi.org/10.1073/pnas.1900278116

Magney, Troy S., Bowling, D.R., Logan, B.A., Grossmann, K., Stutz, J., Blanken, P.D., Burns, S.P., Cheng, R., Garcia, M.A., Köhler, P., Lopez, S., Parazoo, N.C., Raczka, B., Schimel, D., Frankenberg, C., 2019. Mechanistic evidence for tracking the seasonality of photosynthesis with solar-induced fluorescence. Proc. Natl. Acad. Sci. U. S. A. 116, 11640–11645. https://doi.org/10.1073/pnas.1900278116

Maguire, A.J., Eitel, J.U.H., Griffin, K.L., Magney, T.S., Long, R.A., Vierling, L.A., Schmiege, S.C., Jennewein, J.S., Weygint, W.A., Boelman, N.T., Bruner, S.G., 2020. On the Functional Relationship Between Fluorescence and Photochemical Yields in Complex Evergreen Needleleaf Canopies. Geophys. Res. Lett. 47, e2020GL087858. https://doi.org/10.1029/2020GL087858

Maia, V.A., Santos, A.B.M., de Aguiar-Campos, N., de Souza, C.R., de Oliveira, M.C.F., Coelho, P.A., Morel, J.D., da Costa, L.S., Farrapo, C.L., Fagundes, N.C.A., de Paula, G.G.P., Santos, P.F., Gianasi, F.M., da Silva, W.B., de Oliveira, F., Girardelli, D.T., de Carvalho Araújo, F., Vilela, T.A., Pereira, R.T., da Silva, L.C.A., de Oliveira Menino, G.C., Garcia, P.O., Fontes, M.A.L., dos Santos, R.M., 2020. The carbon sink of tropical seasonal forests in southeastern Brazil can be under threat. Sci. Adv. 6, eabd4548. https://doi.org/10.1126/sciadv.abd4548

Marrs, J.K., Reblin, J.S., Logan, B.A., Allen, D.W., Reinmann, A.B., Bombard, D.M., Tabachnik, D., Hutyra, L.R., 2020. Solar-Induced Fluorescence Does Not Track Photosynthetic Carbon Assimilation Following Induced Stomatal Closure. Geophys. Res. Lett. 47, 1–11. https://doi.org/10.1029/2020GL087956

McCallum, I., Franklin, O., Moltchanova, E., Merbold, L., Schmullius, C., Shvidenko, A., Schepaschenko, D., Fritz, S., 2013. Improved light and temperature responses for light-use-

efficiency-based GPP models. Biogeosciences. https://doi.org/10.5194/bg-10-6577-2013

Miao, G., Guan, K., Yang, X., Bernacchi, C.J., Berry, J.A., DeLucia, E.H., Wu, J., Moore, C.E., Meacham, K., Cai, Y., Peng, B., Kimm, H., Masters, M.D., 2018. Sun-Induced Chlorophyll Fluorescence, Photosynthesis, and Light Use Efficiency of a Soybean Field from Seasonally Continuous Measurements. J. Geophys. Res. Biogeosciences. https://doi.org/10.1002/2017JG004180

Migliavacca, M., Musavi, T., Mahecha, M.D., Nelson, J.A., Knauer, J., Baldocchi, D.D., Perez-Priego, O., Christiansen, R., Peters, J., Anderson, K., Bahn, M., Black, T.A., Blanken, P.D., Bonal, D., Buchmann, N., Caldararu, S., Carrara, A., Carvalhais, N., Cescatti, A., Chen, J., Cleverly, J., Cremonese, E., Desai, A.R., El-Madany, T.S., Farella, M.M., Fernández-Martínez, M., Filippa, G., Forkel, M., Galvagno, M., Gomarasca, U., Gough, C.M., Göckede, M., Ibrom, A., Ikawa, H., Janssens, I.A., Jung, M., Kattge, J., Keenan, T.F., Knohl, A., Kobayashi, H., Kraemer, G., Law, B.E., Liddell, M.J., Ma, X., Mammarella, I., Martini, D., Macfarlane, C., Matteucci, G., Montagnani, L., Pabon-Moreno, D.E., Panigada, C., Papale, D., Pendall, E., Penuelas, J., Phillips, R.P., Reich, P.B., Rossini, M., Rotenberg, E., Scott, R.L., Stahl, C., Weber, U., Wohlfahrt, G., Wolf, S., Wright, I.J., Yakir, D., Zaehle, S., Reichstein, M., 2021. The three major axes of terrestrial ecosystem function. Nature. https://doi.org/10.1038/s41586-021-03939-9

Mohammed, G.H., Colombo, R., Middleton, E.M., Rascher, U., van der Tol, C., Nedbal, L., Goulas, Y., Pérez-Priego, O., Damm, A., Meroni, M., Joiner, J., Cogliati, S., Verhoef, W., Malenovský, Z., Gastellu-Etchegorry, J.P., Miller, J.R., Guanter, L., Moreno, J., Moya, I., Berry, J.A., Frankenberg, C., Zarco-Tejada, P.J., 2019. Remote sensing of solar-induced chlorophyll fluorescence (SIF) in vegetation: 50 years of progress. Remote Sens. Environ. 231, 111177. https://doi.org/10.1016/j.rse.2019.04.030

Monteith, J.L., Unsworth, M.H., 1990. Principles of environmental physics, 2nd Edition. Edward Arnold, London.

Morozumi, T., Kato, T., Kobayashi, H., Sakai, Y., Nakashima, N., Buareal, K., Nasahara, K.N., Akitsu, T.K., Murayama, S., Noda, H.M., Muraoka, H., 2023. Contributions of the understory and midstory to total canopy solar-induced chlorophyll fluorescence in a ground-based study in

conjunction with seasonal gross primary productivity in a cool-temperate deciduous broadleaf forest. Remote Sens. Environ. https://doi.org/10.1016/j.rse.2022.113340

Nunes, M.H., Camargo, J.L.C., Vincent, G., Calders, K., Oliveira, R.S., Huete, A., Mendes de Moura, Y., Nelson, B., Smith, M.N., Stark, S.C., Maeda, E.E., 2022. Forest fragmentation impacts the seasonality of Amazonian evergreen canopies. Nat. Commun. 13. https://doi.org/10.1038/s41467-022-28490-7

Paul-Limoges, E., Damm, A., Hueni, A., Liebisch, F., Eugster, W., Schaepman, M.E., Buchmann, N., 2018. Effect of environmental conditions on sun-induced fluorescence in a mixed forest and a cropland. Remote Sens. Environ. 219, 310–323. https://doi.org/10.1016/j.rse.2018.10.018

Pierrat, Z., Magney, T., Parazoo, N.C., Grossmann, K., Bowling, D.R., Seibt, U., Johnson, B., Helgason, W., Barr, A., Bortnik, J., Norton, A., Maguire, A., Frankenberg, C., 2022a. Diurnal and Seasonal Dynamics of Solar-Induced Chlorophyll Fluorescence , Vegetation Indices , and Gross Primary Productivity in the Boreal Forest Journal of Geophysical Research : Biogeosciences. https://doi.org/10.1029/2021JG006588

Pierrat, Z., Magney, T., Parazoo, N.C., Grossmann, K., Bowling, D.R., Seibt, U., Johnson, B., Helgason, W., Barr, A., Bortnik, J., Norton, A., Maguire, A., Frankenberg, C., Stutz, J., 2022b. Diurnal and Seasonal Dynamics of Solar-Induced Chlorophyll Fluorescence, Vegetation Indices, and Gross Primary Productivity in the Boreal Forest. J. Geophys. Res. Biogeosciences 127. https://doi.org/10.1029/2021JG006588

Porcar-Castell, A., Tyystjärvi, E., Atherton, J., Van Der Tol, C., Flexas, J., Pfündel, E.E., Moreno, J., Frankenberg, C., Berry, J.A., 2014. Linking chlorophyll a fluorescence to photosynthesis for remote sensing applications: Mechanisms and challenges. J. Exp. Bot. 65, 4065–4095. https://doi.org/10.1093/jxb/eru191

Rajewicz, P.A., Zhang, C., Atherton, J., Wittenberghe, S. Van, Riikonen, A., Magney, T., Fernandez-marin, B., Ignacio, J., Plazaola, G., Porcar-castell, A., 2023. The photosynthetic response of spectral chlorophyll fluorescence differs across species and light environments in a boreal forest ecosystem. Agric. For. Meteorol. 334, 109434. https://doi.org/10.1016/j.agrformet.2023.109434

Reichstein, M., Falge, E., Baldocchi, D., Papale, D., Aubinet, M., Berbigier, P., Bernhofer, C., Buchmann, N., Gilmanov, T., Granier, A., Grünwald, T., Havránková, K., Ilvesniemi, H., Janous, D., Knohl, A., Laurila, T., Lohila, A., Loustau, D., Matteucci, G., Meyers, T., Miglietta, F., Ourcival, J.M., Pumpanen, J., Rambal, S., Rotenberg, E., Sanz, M., Tenhunen, J., Seufert, G., Vaccari, F., Vesala, T., Yakir, D., Valentini, R., 2005. On the separation of net ecosystem exchange into assimilation and ecosystem respiration: Review and improved algorithm. Glob. Chang. Biol. 11, 1424–1439. https://doi.org/10.1111/j.1365-2486.2005.001002.x

Ryu, Y., Berry, J.A., Baldocchi, D.D., 2019. What is global photosynthesis? History, uncertainties and opportunities. Remote Sens. Environ. 223, 95–114. https://doi.org/10.1016/j.rse.2019.01.016

Schimel, D., Pavlick, R., Fisher, J.B., Asner, G.P., Saatchi, S., Townsend, P., Miller, C., Frankenberg, C., Hibbard, K., Cox, P., 2015. Observing terrestrial ecosystems and the carbon cycle from space. Glob. Chang. Biol. 21, 1762–1776.

Sellers, P.J., Berry, J.A., Collatz, G.J., Field, C.B., Hall, F.G., 1992. Canopy reflectance, photosynthesis, and transpiration. III. A reanalysis using improved leaf models and a new canopy integration scheme. Remote Sens. Environ. 42, 187–216.

Shan, N., Zhang, Y., Chen, J.M., Ju, W., Migliavacca, M., Peñuelas, J., Yang, X., Zhang, Z., Nelson, J.A., Goulas, Y., 2021. A model for estimating transpiration from remotely sensed solar-induced chlorophyll fluorescence. Remote Sens. Environ. 252. https://doi.org/10.1016/j.rse.2020.112134

Sun, Y., Frankenberg, C., Wood, J.D., Schimel, D.S., Jung, M., Guanter, L., Drewry, D.T., Verma, M., Porcar-Castell, A., Griffis, T.J., Gu, L., Magney, T.S., Köhler, P., Evans, B., Yuen, K., 2017. OCO-2 advances photosynthesis observation from space via solar-induced chlorophyll fluorescence. Science (80-. ). https://doi.org/10.1126/science.aam5747

Sun, Y., Fu, R., Dickinson, R., Joiner, J., Frankenberg, C., Gu, L., Xia, Y., Fernando, N., 2015. Drought onset mechanisms revealed by satellite solar-induced chlorophyll fluorescence: Insights from two contrasting extreme events. J. Geophys. Res. G Biogeosciences 120, 2427–2440. https://doi.org/10.1002/2015JG003150

Swoczyna, T., Bussotti, F., Swoczyna, T., Kalaji, H.M., Bussotti, F., Mojski, J., Pollastrini, M., 2022.

Environmental stress -what can we learn from chlorophyll a fluorescence Environmental stress - what can we learn from chlorophyll a fl uorescence analysis in woody plants ? A review. https://doi.org/10.3389/fpls.2022.1048582

Van Der Tol, C., Berry, J.A., Campbell, P.K.E., Rascher, U., 2014. Models of fluorescence and photosynthesis for interpreting measurements of solar-induced chlorophyll fluorescence. J. Geophys. Res. Biogeosciences 119, 2312–2327. https://doi.org/10.1002/2014JG002713

Vitale, L., Arena, C., Virzo de Santo, A., 2012. Seasonal changes in photosynthetic activity and photochemical efficiency of the Mediterranean shrub Phillyrea angustifolia L. Plant Biosyst. https://doi.org/10.1080/11263504.2011.651507

Wang, S., Zhang, Y., Ju, W., Chen, J.M., Ciais, P., Cescatti, A., Sardans, J., Janssens, I.A., Wu, M., Berry, J.A., Campbell, E., Fernández-Martínez, M., Alkama, R., Sitch, S., Friedlingstein, P., Smith, W.K., Yuan, W., He, W., Lombardozzi, D., Kautz, M., Zhu, D., Lienert, S., Kato, E., Poulter, B., Sanders, T.G.M., Krüger, I., Wang, R., Zeng, N., Tian, H., Vuichard, N., Jain, A.K., Wiltshire, A., Haverd, V., Goll, D.S., Peñuelas, J., 2020. Recent global decline of CO2 fertilization effects on vegetation photosynthesis. Science (80-. ). 370, 1295–1300. https://doi.org/10.1126/science.abb7772

Wang, S., Zhang, Y., Ju, W., Wu, M., Liu, L., 2022a. Temporally corrected long-term satellite solar-induced fluorescence leads to improved estimation of global trends in vegetation photosynthesis during ISPRS Journal of Photogrammetry and Remote Sensing Temporally corrected long-term satellite solar-induced. https://doi.org/10.1016/j.isprsjprs.2022.10.018

Wang, S., Zhang, Y., Ju, W., Wu, M., Liu, L., He, W., Peñuelas, J., 2022b. Temporally corrected long-term satellite solar-induced fluorescence leads to improved estimation of global trends in vegetation photosynthesis during 1995–2018. ISPRS J. Photogramm. Remote Sens. 194, 222–234. https://doi.org/https://doi.org/10.1016/j.isprsjprs.2022.10.018

Wang, Y.P., Leuning, R., 1998. A two-leaf model for canopy conductance, photosynthesis and partitioning of available energy I: Model description and comparison with a multi-layered model. Agric. For. Meteorol. https://doi.org/10.1016/S0168-1923(98)00061-6

Wutzler, T., Lucas-Moffat, A., Migliavacca, M., Knauer, J., Sickel, K., Šigut, L., Menzer, O., Reichstein, M., 2018. Basic and extensible post-processing of eddy covariance flux data with REddyProc. Biogeosciences 15, 5015–5030. https://doi.org/10.5194/bg-15-5015-2018

Xiao, J., Chevallier, F., Gomez, C., Guanter, L., Hicke, J.A., Huete, A.R., Ichii, K., Ni, W., Pang, Y., Rahman, A.F., Sun, G., Yuan, W., Zhang, L., Zhang, X., 2019. Remote sensing of the terrestrial carbon cycle: A review of advances over 50 years. Remote Sens. Environ. 233, 111383. https://doi.org/10.1016/j.rse.2019.111383

Xiao, Z., Liang, S., Wang, J., Chen, P., Yin, X., Zhang, L., Song, J., 2014. Use of general regression neural networks for generating the GLASS leaf area index product from time-series MODIS surface reflectance. IEEE Trans. Geosci. Remote Sens. https://doi.org/10.1109/TGRS.2013.2237780

Yang, J.C., Magney, T.S., Albert, L.P., Richardson, A.D., Frankenberg, C., Stutz, J., Grossmann, K., Burns, S.P., Seyednasrollah, B., Blanken, P.D., Bowling, D.R., 2022. Gross primary production ( GPP ) and red solar induced fluorescence ( SIF ) respond differently to light and seasonal environmental conditions in a subalpine conifer forest. Agric. For. Meteorol. 317, 108904. https://doi.org/10.1016/j.agrformet.2022.108904

Yang, P., Prikaziuk, E., Verhoef, W., Van Der Tol, C., 2021. SCOPE 2.0: A model to simulate vegetated land surface fluxes and satellite signals. Geosci. Model Dev. 14, 4697–4712. https://doi.org/10.5194/gmd-14-4697-2021

Zaks, J., Amarnath, K., Kramer, D.M., Niyogi, K.K., Fleming, G.R., 2012. A kinetic model of rapidly reversible nonphotochemical quenching. Proc. Natl. Acad. Sci. U. S. A. 109, 15757–15762. https://doi.org/10.1073/pnas.1211017109

Zeng, Y., Badgley, G., Dechant, B., Ryu, Y., Chen, M., Berry, J.A., 2019. A practical approach for estimating the escape ratio of near-infrared solar-induced chlorophyll fluorescence. Remote Sens. Environ. https://doi.org/10.1016/j.rse.2019.05.028

Zhang, Y., Parazoo, N.C., Williams, A.P., Zhou, S., Gentine, P., 2020. Large and projected strengthening moisture limitation on end-of-season photosynthesis. Proc. Natl. Acad. Sci. U. S.

A. 117, 9216–9222. https://doi.org/10.1073/pnas.1914436117

Zhang, Y., Xiao, X., Wu, X., Zhou, S., Zhang, G., Qin, Y., Dong, J., 2017. A global moderate resolution dataset of gross primary production of vegetation for 2000-2016. Sci. data. https://doi.org/10.1038/sdata.2017.165

Zhang, Z., Chen, J.M., Zhang, Y., Li, M., 2023. Improving the ability of solar-induced chlorophyll fluorescence to track gross primary production through differentiating sunlit and shaded leaves. Agric. For. Meteorol. 341, 109658. https://doi.org/10.1016/j.agrformet.2023.109658

Zhang, Z., Zhang, Y., Porcar-Castell, A., Joiner, J., Guanter, L., Yang, X., Migliavacca, M., Ju, W., Sun, Z., Chen, S., 2020. Reduction of structural impacts and distinction of photosynthetic pathways in a global estimation of GPP from space-borne solar-induced chlorophyll fluorescence. Remote Sens. Environ. 240, 111722.

Zheng, Y., Shen, R., Wang, Y., Li, X., Liu, S., Liang, S., Chen, J.M., Ju, W., Zhang, L., Yuan, W., 2020. Improved estimate of global gross primary production for reproducing its long-Term variation, 1982-2017. Earth Syst. Sci. Data 12, 2725–2746. https://doi.org/10.5194/essd-12-2725-2020

Zhu, K., Chen, J., Wang, S., Fang, H., Chen, B., Zhang, L., Li, Y., Zheng, C., Amir, M., 2023. Characterization of the layered SIF distribution through hyperspectral observation and SCOPE modeling for a subtropical evergreen forest. ISPRS J. Photogramm. Remote Sens. 201, 78–91. https://doi.org/10.1016/j.isprsjprs.2023.05.014

Zhuang, J., Wang, Y., Chi, Y., Zhou, L., Chen, J., Zhou, W., Song, J., Zhao, N., Ding, J., 2020. Drought stress strengthens the link between chlorophyll fluorescence parameters and photosynthetic traits. PeerJ 8, 1–20. https://doi.org/10.7717/peerj.10046

## List of Figure Captions

**Figure ~~1~~1**. The performance of different models in estimating the half-hourly (or hourly) GPP. Each row represents the results of different methods, and each column represents the results of different ENF sites. (a)-(c), (d)-(f), (g)-(i), and (j)-(l) show the performance of the two-leaf,

layered, layered two-leaf, and big-leaf models, respectively. The figures in the first column show the GPP estimation tested at the CA-obs site, the figures in the second column show the results of the US-NR1 site, and those in the last column show the results of the KR-TCK site. All GPP estimations in this figure used the iterative method to estimate Ci. The color of the dots represents the corresponding air temperature, the dashed black line is the regression line, and the solid red line is the 1:1 line.

**Figure ~~2~~2.** Time series of GPP observations and GPP estimates from the (a) two-leaf, (b) layered, (c) layered two-leaf, (d) big-leaf, and (e) linear models using the empirical linear relationship between SIF and GPP and from the (f) nonlinear model based on the empirical relationship between SIF and GPP. The grey dots represent the half-hourly observations, and the pink dots represent the GPP estimates. Here, we only displayed the results from the CA-obs site using the iterative method for estimating Ci.

**Figure ~~3~~3.** Diurnal dynamics of GPP observation and GPP estimates from (a) the two-leaf, (b) layered, (c) layered two-leaf, (d) big-leaf, (e) linear, and (f) nonlinear models. Variables with the suffix "_iter" refer to GPP estimation with $C_i$ estimated using the iterative method, and variables with the suffix "_lambda" refer to GPP estimation with $C_i$ estimated via the simple λ-based method. This figure shows the results from the CA-obs site using all of the half-hourly data obtained during the entire study period. The solid lines represent the average dynamics, and the shaded areas represent 95% confidence intervals. Similar results were obtained at the other sites.

**Figure ~~4~~4.** Comparison between the diurnal dynamics of GPP estimations from the big-leaf model and the (a) layered, (b) two-leaf, and (c) layered two-leaf models and the corresponding (d) incident PAR, (e) temperature, (f) SIF, and (g) GPP on July 29, 2019, and August 2, 2019. (h) shows the changes in estimated J/SIF ratio, and (i) shows the dynamics of estimated J using the big-leaf model. The shaded areas represent the 95% interval. All the data used in this figure were obtained from the CA-obs half-hourly dataset.

**Figure ~~5~~5.** Diurnal dynamics of GPP estimation in different layers. The GPP estimations in (a) and (b) came from the layered model, and the GPP estimations in (c) and (d) came from the

layered two-leaf model. The color of the dots represents the layer index, and a larger number represents a deeper location within the canopy. The LAI of each layer in this figure can be calculated as total LAI/10.

**Figure ~~6~~6.** Depths of the layer above which the leaves contributed 80% of the total GPP on July 29, 2019, and August 2, 2019. Data used for depth estimation and plotting were half-hourly estimations from (a) the layered model and (b) the layered two-leaf model at the CA-obs site.

**Figure ~~7~~7.** (a) Diurnal variation in the GPP contribution of shaded leaves; (b) seasonal variation in the GPP contribution of shaded leaves; (c) diurnal variation in the LAI fraction of shaded leaves; (d) seasonal variation in the LAI fraction of shaded leaves. The cross-marks in the plots represent the outliers, the black dots represent the mean values of each box, and the green lines represent the median values of each box.

**Figure ~~8~~8.** The light response of single-leaf qL (in red), canopy-scale qL obtained from the layered model (in gray), and canopy-scale qL from the two-leaf model (in pink). The PAR label of the x-axis refers to the incident PAR obtained at the top of the canopy.

**Figure ~~9~~9.** The impact of LAI on the light response of the (a) canopy-scale qL from the two-leaf model; (b) canopy-scale qL of sunlit leaves; (c) canopy-scale qL of shaded leaves. The color of the dots represents the corresponding LAI. The PAR label of the x-axis refers to the incident PAR obtained at the top of the canopy.

**Figure ~~10~~10.** The diurnal patterns of single-leaf qL (red lines), canopy qL from the layered model (black lines), canopy-scale qL from the two-leaf model (green lines), and the qL in different layers of the canopy (colored scatters). The color of the dots represents the layer index, and the larger number represents the deeper location within the canopy. The LAI of each layer in this figure can be calculated as total LAI/10.

## Highlights

1. Considering vertical light gradient improves sub-daily GPP estimation via SIF.
2. Two-leaf assumption helps in capturing the diurnal variations in GPP.
3. Canopy-scale qL is less sensitive to PAR than the single-leaf qL.

# Improving estimates of sub-daily gross primary production from solar-induced chlorophyll fluorescence by accounting for light distribution within canopy

**Ruonan Chen[1,2,3], Liangyun Liu [1,2,3*], Xinjie Liu [1,2], Zhunqiao Liu[4], Lianhong Gu[5], Uwe Rascher[6]**

[1]International Research Center of Big Data for Sustainable Development Goals (CBAS), Beijing, 100049, China

[2]Key Laboratory of Digital Earth Science, Aerospace Information Research Institute, Chinese Academy of Sciences, Beijing, 100094, China;

[3]College of Resources and Environment, University of Chinese Academy of Sciences, Beijing, 100049, China

[4]State Key Laboratory of Soil Erosion and Dryland Farming on the Loess Plateau, Northwest A&F University, Yangling, Shaanxi 712100, China

[5]Environmental Sciences Division and Climate Change Science Institute, Oak Ridge National Laboratory, Oak Ridge, TN 37831, USA;

[6]Institute of Bio- and Geosciences, Plant Sciences, Forschungszentrum Jülich GmbH, Jülich, Germany.

Corresponding author: Liangyun Liu (liuly@radi.ac.cn)

## Abstract

Solar-induced chlorophyll fluorescence (SIF) has long been regarded as a proxy for photosynthesis and has shown superiority in estimating gross primary production (GPP) compared to traditional vegetation indices, especially in evergreen ecosystems. However, current SIF-based GPP estimations regard the canopy as a large leaf and seldom consider the impact of interactions among light, canopy structure, and leaf physiology. In this study, we proposed GPP estimation models with different descriptions of light–structure–physiology interactions (including the layered model, the two-leaf model, and the layered two-leaf model)

and compared their performances with the big-leaf model using half-hourly (or hourly) observations at evergreen needleleaf forest sites. First, we found that the big-leaf model underestimated GPP, especially at noon. All models showed higher accuracy than that of the big-leaf model. Second, we investigated the diurnal dynamics of GPP estimations in each canopy layer and found that models with a two-leaf assumption captured the diurnal variations in GPP better than that with the layered assumption. We also deduced that the poor performance of the big-leaf model was related to its overestimation of the overall light stress on the redox state of PSII reaction centers (qL). Finally, we noticed that the qL at the canopy scale had lower sensitivity to light change than the single-leaf qL and that the light response of canopy-scale qL was influenced by the leaf area index during seasonal cycles. Overall, this study describes methods to accurately estimate sub-daily GPP from SIF in evergreen needleleaf forests and demonstrates that the interactions among light, canopy structure, and leaf physiology regulate the SIF-GPP relationship at the canopy scale. Further, it indicates the need to consider the description of light distribution within the canopy in next-generation terrestrial biosphere models, even if they incorporate SIF to constrain their parameterization. Thus, upscaling the established leaf-scale mechanistic SIF-GPP relationship or findings to canopy-scale applications still requires much work, especially when there are significant changes in environmental conditions and their within-canopy distributions.

**Keywords:** solar-induced chlorophyll fluorescence (SIF); gross primary productivity (GPP); two-leaf model; layered model; evergreen needle forests

## 1. Introduction

Photosynthesis in terrestrial ecosystems plays an important role in the global carbon cycle, offsetting approximately 30% of anthropogenic carbon dioxide ($CO_2$) emissions over the past century (Friedlingstein et al., 2020). Compared to ocean carbon sinks, land carbon cycles are sensitive to climate change and are highly unstable (Ciais et al., 2005; Friedlingstein et al., 2020; Luijkx et al., 2015; Maia et al., 2020), making them a crucial but largely uncertain part of global change studies. As one of the largest fluxes in the terrestrial carbon cycle (Wang et al., 2022b),

gross primary production (GPP) indicates the $CO_2$-assimilation ability of vegetation and is the foundation of many ecosystem functions and services (for example, providing food and fiber, altering local climate, and regulating the land–air interaction process) (Migliavacca et al., 2021; Ryu et al., 2019; Xiao et al., 2019). However, substantial difficulties and uncertainties in GPP quantification at a large scale remain despite decades of research (Ryu et al., 2019).

Before the emergence of state-of-art solar-induced chlorophyll fluorescence (SIF) techniques, ground GPP data were mainly obtained from in situ measurements of eddy covariance flux towers with limited spatial representativeness, and global GPP products were either model-based estimates, including light use efficiency models and process models, such as VPM (Zhang et al., 2017) and BEPS (Chen et al., 1999), or upscaled values from flux tower observations (for example, FLUXCOM) (Jung et al., 2019). These traditional GPP measurements and products are either not ideal for supporting the analyses on large spatiotemporal scales due to significant regional bias or are based on multiple large simplifications and assumptions (Anav et al., 2015; Wang et al., 2022a), leading to large uncertainties and divergence in their long-term trends (Cai et al., 2014; Wang et al., 2022a; Zheng et al., 2020). Remote-sensing methods based on vegetation indices (VIs) could partly capture the dynamics of photosynthesis and assist in the estimation of GPP, buthe effectiveness of VIs-based methods is mainly related to their representativeness of vegetation greenness (Li and Xiao, 2020), indicating that they might lose their power in ecosystems with an almost invariant canopy structure (such as evergreen forests) (Magney et al., 2019). The rapid development of SIF measurement and retrieval methods has facilitated the monitoring of photosynthetic dynamics on a large scale (Guanter et al. 2021; Joiner et al. 2011, 2016; Mohammed et al. 2019; Schimel et al. 2015; Sun et al. 2017; Du et al., 2022), although some limitations still exist, such as the sparse sampling or coarse spatial resolution of current satellite-based SIF products. SIF is the electromagnetic signal emitted by chlorophyll molecules after absorbing solar radiation. Together with non-photochemical quenching (NPQ) and photochemical reactions, SIF consumes the total absorbed light inside plants. Therefore, SIF contains information on physiology that can be detected using remote sensors (Porcar-Castell et al., 2014). Numerous studies have demonstrated the tight link between SIF and GPP, although

studies also show the decoupling of SIF and GPP during mild stress events (Helm et al., 2020; Marrs et al., 2020) and changes in their relationship at different spatiotemporal scales (Magney et al., 2020). Further, SIF is employed as a proxy for photosynthesis in many agricultural, ecological, and Earth system studies (Sun et al., 2015; Wang et al., 2020; Y. Zhang et al., 2020). Several studies have directly used the empirical relationship to estimate GPP via SIF observations, even though this relationship has been proven to be biome-specific (Damm et al., 2015; Liu et al., 2017).

Although both SIF and GPP are largely driven by absorbed photosynthetic active radiation (APAR) at the canopy scale (Du et al., 2017; Miao et al., 2018), discrepancies between them remain. The possible discrepancy between LUE and $\Phi F \times fesc$ is one of the essential explanations for the dynamic relationship or decoupling between SIF and GPP. The physiological dynamics in the ΦF-LUE relationship (Porcar-Castell et al., 2014) theoretically influence the SIF-GPP relationship, and the positive correlation between LUE and fesc (for far-red SIF) found at the seasonal scale also strengthens the link between SIF and GPP (Liu et al., 2020). These mechanisms result in the coupling of SIF and GPP as a mixture of canopy structure interference and physiological processes. Recent studies have demonstrated the variant physiological linkage between SIF and GPP (Magney et al., 2020), which can be influenced by the environment and the status of the plant (for example, stress conditions and development stages) (Chen et al., 2022b, 2022a; Kim et al., 2021; Paul-Limoges et al., 2018; Zhuang et al., 2020). Even for evergreen needleleaf forests (ENF) with little variation in fesc during seasonal cycles, SIF does not change in perfect agreement with GPP and shows lower sensitivity to environmental changes (Pierrat et al., 2022b; Yang et al., 2022).

Therefore, accurate estimation of GPP using SIF requires the construction of a mechanistic model with the help of physiological findings. The mechanistic light response (MLR) model proposed by Gu (2019) links the quantitative SIF-GPP relationship to active fluorescence parameters with specific physiological meanings, such as qL (the fraction of opened PSII reaction centers) and $\Phi_{PSIImax}$ (the maximum photochemical quantum yield of PSII). In this model, qL is a key parameter influenced by the actual illumination condition of leaves; thus, the dynamics of qL are crucial to SIF-based GPP estimations in diurnal cycles. The

effectiveness of the MLR model has already been demonstrated by a previous leaf-scale study (Han et al., 2022b) but has not been extensively tested at the canopy scale or long time scales.

One study has attempted to directly estimate GPP from canopy SIF in a winter-wheat field (Liu et al., 2022), but it is based on the big-leaf assumption. The big-leaf assumption regards vegetation as a large flat leaf and assumes the same leaf property and the same direct and diffuse radiation conditions in the canopy (Guan et al., 2022; McCallum et al., 2013; Sellers et al., 1992). Therefore, GPP estimations using this method neglect the possible impact of the light distribution (caused by the three-dimensional structure) within the canopy. This assumption is acceptable for crops with a simple structure and low height (anthropogenic ecosystems), as indicated by the model's success in direct SIF-based estimation in Liu's study (2022), but it may be unsuitable for natural ecosystems with complex canopy structures. The big-leaf assumption does not cause much uncertainty at the seasonal scale, but is unsuitable for the half-hourly estimation of GPP in forests (Chen et al., 1999). Diurnal changes in incident light interplay with the canopy structure, leading to a dynamic vertical gradient (redistribution) of light within the canopy. This interaction changes the actual light environment faced by each leaf, thereby causing vertical variations in the biophysical status of leaves and influencing the diurnal patterns of SIF and GPP (Chang et al., 2021). Therefore, it is necessary to consider the dynamic light and its interaction with the canopy structure and leaf physiology along the vertical dimension when using canopy SIF observations to estimate the half-hourly GPP in forest ecosystems. Recently, some studies using the LUE framework considered the impact of vertical light gradient on LUE and improved the GPP estimation(Guan et al., 2022, 2021), but there are no study directly considering the impact of vertical light gradient on SIF-GPP relationship to improve SIF-based GPP estimation at sub-daily scales.

Previous leaf-scale observations at two ENF sites have demonstrated that knowledge of sub-canopy and diurnal patterns of irradiance can assist in the investigation of physiological constraints on fluorescence (Maguire et al., 2020), but there have been few canopy-scale studies accounting for this issue. Recently, an observational study investigated the contributions of understory and midstory SIF to the total SIF, and it showed the different relationships between GPP and SIF in different layers (Morozumi et al., 2023). In addition, total emitted SIF was

found to outperform top-of-canopy SIF in GPP estimation in many observational studies (Liu et al., 2020; Lu et al., 2020; Zhang et al., 2020), which indicate the importance of considering vertical variations within the canopy. There was also a study combining hyperspectral observations at different canopy layers with SCOPE modeling to estimate the total SIF in a subtropical evergreen forest. The results of that study showed that using the layered SIF benefits GPP estimation (Zhu et al., 2023). These studies highlight the importance of considering canopy vertical heterogeneity in the interpretation and application of SIF (Chang et al., 2021).

The vertical distribution of light plays an important role in the canopy's vertical heterogeneity. It should be considered in SIF-based GPP estimation since it impacts both the source energy for photosynthesis and the photosynthetic response of spectral fluorescence (Rajewicz et al., 2023). Dividing the canopy into several layers and estimating the GPP for each layer separately may be a solution that can be used to consider the vertical distribution of light, but does not consider the situation in which there may be two types of leaves irradiated by direct light or scattered light at the same depth in the canopy. Under high light conditions, leaves exposed to direct light are likely to be light-saturated or even photoinhibited, whereas leaves exposed to scattered light can still photosynthesize efficiently. Therefore, differentiating sunlit and shaded leaves can improve the SIF-based GPP estimation (Zhang et al., 2023). Being widely used in terrestrial biosphere models, the two-leaf model divides the leaves into shaded and sunlit leaves and describes the different light environments faced by them (Chen et al., 1999; Guan et al., 2022; He et al., 2013). Thus, this method considers the different effects of direct and scattered light on plant photosynthesis. However, because it uses the overall light environment of shaded leaves and does not explicitly describe the scattered light gradient in the vertical direction, we are unsure whether this simplification will significantly impact the SIF estimation of GPP. The methods described above illustrate within-canopy light distribution in different ways, but we cannot directly determine the description that is more suitable for SIF-based half-hourly GPP estimation in ENFs.

Therefore, in this study, we used SIF to estimate GPP using tower-based observations at ENF sites under the framework of the MLR model. We employed a layered model (separating leaves into several layers), a two-leaf model (separating leaves into sunlit and shaded groups), and a

layered two-leaf model (separating leaves into sunlit and shaded groups for each layer) to describe the interaction among the light conditions, canopy structure, and leaf physiology to estimate half-hourly GPP. We then compared the effectiveness of these three models with that of the big-leaf assumption and analyzed their performances in tracking GPP dynamics during the day. With the help of accurate GPP estimation results, we obtained the canopy-scale qL, determined its light response pattern, and compared it with the leaf-scale pattern. In this study, we attempted to answer the following questions:1. How can SIF-based GPP estimates be improved at the half-hourly scale, and how does the big-leaf assumption affect the SIF-based GPP estimation at ENF sites? 2. What are the differences in the performance of models with different descriptions of light–structure–physiology interactions (including layered, two-leaf, and layered two-leaf models)? 3. How does the redistribution of light within the canopy affect the diurnal variation and vertical distribution pattern of GPP and plants' physiological properties (qL)? 4. What is the difference in the light responses of the overall qL (referred to as "canopy-scale qL" in the following part) and the single-leaf qL, and what factors can explain this difference?

## 2. Materials and Methods

### 2.1 Study Sites

In this study, we used tower-based SIF and GPP observations from three open-access ENF sites to examine the performance of our methods; to investigate the dynamics of the estimated GPP, light conditions, and qL at different canopy depths; and to obtain the canopy-scale qL. Among these sites, the data for the boreal forest site (Southern Old Black Spruce, located in Canada, site ID: CA-Obs) was obtained from FLUXNET and spanned September 2018 to December 2020 (Pierrat et al., 2022); the data for subalpine conifer forest site (Niwot Ridge, located in America, site ID: US-NR1) was obtained from AmeriFlux, and had observations from September 2017 to June 2018 (Magney et al., 2019); and the data for the temperate ENF site (located in Taehwa Mountain in South Korea, site ID: KR-TCK) was obtained from AsiaFlux, covering measurements from September 2018 to December 2018 (Kim et al., 2021). The

photosynthetic active radiation (PAR) averages of the observations were similar during the study period (for the KR-TCK site, 680.59 μmol/$m^2$/s; for the CA-obs site, 607.22 μmol/$m^2$/s; for the US-NR1site, 689.06 μmol/$m^2$/s). The annual average air temperature at these sites was 1.4 °C (CA-obs), 1.5 °C (US-NR1), and 12.7 °C (KR-TCK). Other detailed information regarding these sites is provided in Table S1. We tested the landscape heterological conditions around the sites via visual interpretation using the Google Earth platform, and images of the landscape conditions around these sites are shown in Figure S1. Using the ratio of 30 m NDVI (the normalized difference vegetation index) to 250 m NDVI as the indicator of representativeness, we found that all sites are generally homogeneous and have fine representativeness (close to 1; Figure S2).

**2.2 Datasets**

All the SIF data used in this research were obtained from canopy-scale measurements using tower-based monitoring systems. For the CA-obs site, the average canopy height was approximately 16 m, and a scanning spectrometer system (Photospec) was installed at the top of a 26 m tower to obtain the canopy SIF (Pierrat et al., 2022). The PhotoSpec system enables SIF retrieval in the red (680–686 nm) and far-red (745–758 nm) wavelength ranges (Grossmann et al., 2018), as well as supports the calculation of vegetation indices due to its moderate resolution at the corresponding wavelengths. The US-NR1 site also used the Photospec system fixed on the top of a tower (also 26 m above the ground) and measured the spectra with a time resolution of ~20 s per measurement (Magney et al., 2019). SIF values at both CA-obs and US-NR1 sites were retrieved using a Fraunhofer-line-based based fitting algorithm (Grossmann et al., 2018), and the SIF retrieval error was lower than 0.2 W$m^2$/sr/μm at the CA-obs site. For the KR-TCK site, the average canopy height was approximately 20 m, and observations were measured using a QE Pro system installed at the top of the 40 m tower. At this site, only far-red SIF (760 nm) was retrieved using the Singular Vector Decomposition (SVD) method, and SIF values with rRMSE larger than 25% were removed to ensure data quality. The spectral reflectance at this site was collected using Jaz spectroradiometers (Ocean Insight, Dunedin, FL, USA), which cover a spectral range of 350–1020 nm (Kim et al., 2021). Notably, the unit of

SIF measurements at both the CA-obs and US-NR1 sites was mW/m$^2$/nm/sr due to the hemispherical–conical configuration of Photospec, whereas the unit of SIF measurements at the KR-TCK site was mW/m$^2$/nm because two cosine correctors were used to obtain the hemispheric SIF.

GPP measurement relies on the eddy covariance technique. For all sites, a 3-D sonic anemometer and infrared gas analyzer fixed on the flux towers were used to measure the wind speed and $CO_2$ concentration, which allowed calculation of the 30 min net ecosystem exchange (NEE) using Eddy-Pro software. Then, various preprocessing procedures, including data quality control, night-time $CO_2$ flux corrections, and gap filling, were employed on the NEE time series; finally, GPP was obtained after the partition step (Barr et al., 2004; Reichstein et al., 2005; Wutzler et al., 2018).

In addition to GPP observations, the flux tower provides meteorological data every 30 min. In this study, we mainly used air temperature, PAR, and relative humidity data. Using air temperature and relative humidity, we further determined the vapor pressure deficit according to Tetens's formula (Monteith and Unsworth, 1990) for describing atmospheric dryness and calculating carbon-reaction-related parameters:

$$VPD = 0.61078 \times e^{\frac{17.27 \times T_a}{T_a + 237.3}} \times (1 - RH) \quad (1)$$

where $T_a$ is the air temperature (°C), RH is relative humidity (%), and VPD is the vapor pressure deficit (kPa). In our study, the unit of VPD was converted to Pa. By averaging the records every half hour, all these sites provided a continuous time series of observations at a temporal resolution of 30 min, except US-NR1 (because only hourly GPP was obtained at this site). Based on the 30 min incident PAR and the PAR at the top of the atmosphere (which was calculated using the latitude, longitude, and corresponding time), we calculated the clearness index following the method in Chen et al. (1999) to describe the weather condition and determine the ratio of direct to diffuse light in the two-leaf model:

$$\mathrm{CI} = \frac{\mathrm{PAR}}{\mathrm{PAR_{TOA}}} = \frac{\mathrm{PAR}}{S_0 \times 0.46} \quad (2)$$

where $S_0$ represents the solar constant (1367 W/m$^2$), and 0.46 is the fraction of PAR in the incoming solar radiance. We used 0.219 covert the unit of PAR (from μmol/m$^2$/s to W/m$^2$) in this equation.

In this study, we also used the leaf area index (LAI) and clumping index (Ω) to describe canopy structure. The LAI data used in this research were obtained from a GLASS LAI product with 500 m spatial resolution (Xiao et al., 2014), and the Ω data were also from a 500 m satellite product generated based on MODIS products (Jiao et al., 2018). The time series of LAI and Ω were extracted according to the location of each site, and the possible uncertainties introduced by satellite products were tested using ground measurement LAI data at the KR-TCK site. We also used another clumping index dataset to clarify the uncertainties introduced by different satellite clumping index products (Li and Fang, 2022). To estimate the escape probability of SIF photons (details in Section 2.5, equation 18), we also employed NDVI, NIR (near-infrared reflectance), and fPAR using the in situ measurements provided by each site (Kim et al., 2021; Magney et al., 2019; Pierrat et al., 2022a). More details can be found in the original papers (Kim et al., 2021; Magney et al., 2019; Pierrat et al., 2022a).

### 2.3 The framework of SIF-based GPP estimation

In this study, we used the framework of the MLR model to estimate GPP at three ENF sites. According to previous work (Gu et al., 2019), the electron transportation rate (J) can be expressed using the full-band PSII SIF ($SIF_{full}$) and fluorescence kinetics parameters:

$$J = \frac{(1 + k_{df}) q_L \Phi_{PSIImax}}{1 - \Phi_{PSIImax}} SIF_{full} \quad (3)$$

where $SIF_{full}$ refers to the total full-band PSII SIF (unit: μmol/m$^2$/s, calculation details in Section 2.5); qL is the fraction of opened PSII reaction centers; $\Phi_{PSIImax}$ is the maximum photochemical quantum yield of PSII; and $k_{df}$ is the ratio of the rate constant for constitutive heat loss to the rate constant for fluorescence emission, which is almost a constant (Zaks et al., 2012). In this study, we used $k_{df}$ = 9, which was in accordance with previous measurements (Liu et al., 2022). qL can be expressed as an exponential function of light (Liu et al., 2021a), and $\Phi_{PSIImax}$ can be estimated using a quadratic function of temperature due to its high correlation with temperature

(Swoczyna et al., 2022; Vitale et al., 2012):

$$q_L = a_L\, e^{-b_L PAR} \tag{4}$$

$$\Phi_{PSIImax} = a\, {T_a}^2 + bT_a + c \tag{5}$$

where Ta represents the temperature, and PAR is the photosynthetic active radiance. We took $a_L = 1$, $b_L = 0.001$, a = -0.0011, b = 0.036, and c = 0.44, according to previous studies (Feng et al., 2021). The values of aL and bL are consistent with previous studies (Feng et al., 2021), and the values of a, b, and c were fitted based on long-term pulse amplitude modulation (PAM) observations (for details, see Text S1).

Notably, J in the MLR model represents the actual electron transport rate, which is possible because the SIF in this model already contains information about the light reaction in photosynthesis. Thus, this SIF-based model does not require the complex estimation of $J_{max}$ (maximum electron transport rate) and comparison of Ac (rubisco-limited photosynthesis) and Aj (RuBP-limited photosynthesis), which is crucial in the widely used FvCB model (Farquhar et al., 1980).

For the quantitative relationship between J and GPP, we referred to the FvCB model and used the following equation:

$$GPP = J\frac{C_i - \Gamma^*}{4C_i + 8\Gamma^*} \tag{6}$$

where $C_i$ is the intercellular $CO_2$ partial pressure, and Γ* is the photocompensation point of $CO_2$ in the absence of dark respiration. The estimation of $C_i$ and Γ* is included in Section 2.6.

Finally, combining Equations 3 and 6, we used the following model to estimate GPP (Gu et al., 2019):

$$GPP = \frac{C_i - \Gamma^*}{4C_i + 8\Gamma^*}\frac{\left(1 + k_{df}\right)q_L\Phi_{PSIImax}}{1 - \Phi_{PSIImax}}SIF_{full} \tag{7}$$

### 2.4 Description of interactions among light, canopy structure, and leaf physiology

Compared to the vertical distribution of environmental factors such as temperature and moisture,

the vertical distribution of light exposure of leaves within the canopy is highly dynamic during diurnal cycles. Because the intensity and angle of incident light vary significantly with time, light is redistributed when it penetrates the canopy, resulting in a changing vertical gradient and horizontal heterology in within-canopy illumination. Furthermore, one of the key parameters in the MLR model, qL, is highly sensitive to changes in light. Therefore, diurnal variation in light affects SIF and GPP by interfering with the canopy-scale APAR, and it also alters the relationship between SIF and GPP by regulating the qL of individual leaves. Therefore, the dynamics of the SIF-GPP relationship and canopy-scale qL (the overall qL) at the half-hourly scale are the result of the interaction among light, canopy structure, and plants' physiological properties, which should be described well for the accurate estimation of half-hourly (or hourly) GPP. In this study, we proposed and compared methods with different assumptions (layered, two-leaf, and layered two-leaf assumptions) to describe the manner in which the canopy structure affects light distribution and qL.

### 2.4.1 Construction of a layered model

First, we used a layered model to capture the vertical gradient of light. This method separates the canopy into several layers and estimates the GPP for each layer. Adding these GPP values, we obtained the GPP of the entire canopy (the layered GPP in this study). The canopy layers were divided according to the canopy optical depth of LAI rather than vertical height. Therefore, a layer with a higher index indicated a location in a deeper canopy. The GPP estimation in each layer followed the MLR framework in Equation 7, and product of APAR and ΦF was used to divide $SIF_{full}$ of the whole canopy into the full-band PSII SIF of different layers:

$$SIF_i = SIF_{full} \times \frac{APAR_i \times \Phi F_i}{\sum_{L=1}^{n} APAR_L \times \Phi F_L} \quad (8)$$

where n represents the total number of layers; i is the layer index (ranging from 0 to n-1, where i = 0 represents the top layer); and $SIF_i$, $APAR_i$, and $\Phi F_i$ represent the full-band PSII SIF, APAR, and ΦF in layer i, respectively. We used n = 10 in this research, and to assess the uncertainty introduced by the value of n, we tested different values (n = 5, 10, 20, 40, 80, 160, 320, and 640) to examine the impact of the model performance.

In this method, we simplified the radiative transmission process and did not account for the impacts of leaf single scattering albedo, the fraction of diffused light, and the absorption and reflectance of soil backgrounds. Therefore, the APAR for each canopy layer can be expressed as the difference between the PAR at the top of this layer and the PAR at the top of the next layer (Chang et al., 2021). Here, $APAR_i$ is represented as the difference between the PAR in layer i+ 1 ($PAR_{i+1}$) and that in layer i ($PAR_i$), $\Phi F_i$ can be estimated using a fitted function of $PAR_i$ (Liu et al., 2021), and $PAR_i$ can be obtained according to Lambert–Beer's law:

$$APAR_i = PAR_i - PAR_{i+1} \tag{9}$$

$$PAR_i = PAR \times e^{-\frac{0.5 \times \Omega \times LAI_{ai}}{\cos(SZA)}} \tag{10}$$

where PAR is the incident PAR at the top of the canopy, $LAI_{ai}$ is the accumulated LAI from the top to layer i (equal to LAI × i/n), $\Omega$ is the clumping index, and SZA is the solar zenith angle. Combining Equations 9 and 15, we can obtain the qL of layer i and use it to estimate the GPP of layer i ($GPP_i$). Although $\Phi F_i$ can be influenced by many other factors, PAR contributes significantly to its vertical variation. Compared to the variation in APAR, variation in ΦF is usually small (Van der Tol et al., 2014) and may not significantly influence the results. We examined the model's performance when solely APAR was used for the SIF partition to clarify the contribution of ΦF to the model's performance.

### 2.4.2 Construction of the two-leaf model

The second method used to describe light–structure interaction is based on the two-leaf model proposed by Chen et al. (1999), which considers different illumination conditions in the horizontal direction. In the two-leaf model, the leaves are separated into sunlit and shaded groups, and the total GPP is calculated using the sum of GPPs from sunlit and shaded leaves. Similar to the layered model, we divided the $SIF_{full}$ of the entire canopy into $SIF_{shade}$ and $SIF_{sun}$ according to APAR × ΦF. Here, $APAR_{shade}$, and $APAR_{sun}$ could be estimated using the following equations:

$$\mathrm{APAR}_{sun} = (1 - \mathrm{a}) * \mathrm{PAR}_{sun} * \mathrm{LAI}_{sun} \tag{11}$$

$$\mathrm{APAR}_{shade} = (1 - \mathrm{a}) * \mathrm{PAR}_{shade} * \mathrm{LAI}_{shade} \tag{12}$$

where a represents the leaf albedo, taken as 0.15 for evergreen needle forests according to a previous study (He et al., 2013), and $PAR_{sun}$, $PAR_{shade}$, $LAI_{sun}$, and $LAI_{shade}$ are directly calculated using the equations in the work of Chen et al. (1999) (Details in Supplementary Text S2). Because the two-leaf model includes the effects of direct PAR and diffuse PAR, calculating these parameters requires the clearness index for the partition of PAR:

$$PAR_{dif} = PAR \times (0.7527 + 3.8453CI - 16.316CI^2 + 18.962CI^3 - 7.0802CI^4) \quad (13)$$

$$PAR_{dir} = PAR - PAR_{dif} \quad (14)$$

where $PAR_{dif}$ is the diffuse PAR, $PAR_{dir}$ is the direct PAR, and CI is the clearness index.

### 2.4.3 Construction of the layered two-leaf model

Finally, although the two-leaf model considered the different light conditions for sunlit and shaded leaves, it only divided the leaves into two groups and used $PAR_{shade}$ to represent the overall illumination of shaded leaves. This simplification neglected the vertical gradient of diffuse PAR in the canopy, which may introduce uncertainty in ecosystems with large tree heights. To examine whether this issue will influence GPP estimation, we combined the layered model and the two-leaf model to establish a layered two-leaf model. In this model, $SIF_i$ in layer i was still allocated to $SIF_{shade\_i}$ and $SIF_{sun\_i}$ based on APAR×ΦF. Therefore, $SIF_{sun}$ and $SIF_{shade}$ in layer i and were expressed as the following equations:

$$SIF_{sun\_i} = SIF_{full} \times \frac{APAR_{sun\_i} \times \Phi F_{sun\_i}}{\sum_{L=1}^{n} APAR_{shade\_L} \times \Phi F_L + \sum_{L=1}^{n} APAR_{sun\_L} \times \Phi F_{sun\_L}} \quad (15)$$

$$SIF_{shade\_i} = SIF_{full} \times \frac{APAR_{shade\_i} \times \Phi F_{shade\_i}}{\sum_{L=1}^{n} APAR_{shade\_L} \times \Phi F_L + \sum_{L=1}^{n} APAR_{sun\_L} \times \Phi F_{sun\_L}} \quad (16)$$

By replacing LAI with $LAI_{ai}$ (accumulated LAI from the top to the layer i, equals to LAI×i/n) in Chen's work (1999), we calculated $PAR_{sun\_i}$ and $PAR_{shade\_i}$ in layer i; by dividing the $LAI_i$ into sunlit fraction and shaded fraction, we obtained $LAI_{sun\_i}$ and $LAI_{shade\_i}$; finally, using equations similar to Equations 11 and 12, we obtained $APAR_{sun\_i}$ and $APAR_{shade\_i}$. In the combined model (layered two-leaf model), we estimated the $GPP_{shade}$ and $GPP_{sun}$ for each layer, and the sum of these GPPs from different leaf groups was the final GPP estimated using the third method.

## 2.5 Conversion from SIF observations to full-band PSII SIF ($SIF_{full}$)

Due to the multi-scattering and reabsorption effects during radiative transfer in the canopy, the SIF signal observed by sensors is only a small fraction of the total SIF and is also a mixture of the signals emitted by different photosystems (PSI and PSII). Therefore, we first partitioned the observed SIF into $SIF_{PSII}$ and $SIF_{PSI}$ using the ratio of PSII fluorescence to the PSI+PSII fluorescence given wavelength (fPSII):

$$SIF_{PSII\_obs} = SIF_{obs} \times fPSII \quad (17)$$

For the KR-TCK site, fPSII was calculated at 760 nm wavelength; for the CA-obs and US-NR1 sites, fPSII was calculated as the ratio of the integrated PSII SIF to the integrated total SIF from 745 to 758 nm. We calculated the fPSII values based on the Soil Canopy Observation of Photosynthesis and Energy (SCOPE) model simulations considering various canopy structure conditions described by Liu et al. (2022), and obtained values of 0.6676 for the Ca-obs and US-NR1sites and 0.6481 for the KR-TCK site.

Then, to downscale the canopy-scale PSII SIF, we calculated the escape probability of SIF photons from the leaf surface to the top of the canopy (fesc) using the method proposed by Zeng et al. (2019):

$$fesc = \frac{NIRv}{fPAR} = \frac{NDVI \times NIR}{fPAR} \quad (18)$$

where NIRv is the near-infrared reflectance of vegetation, NDVI is the normalized difference vegetation index, and fPAR is the fraction of absorbed photosynthetic active radiation. This method is based on the similar radiative transfer of reflectance and emitted SIF at the near-infrared wavelengths. Upon dividing the canopy-scale SIF observations ($SIF_{PSII\_obs}$) using fesc, we obtained the total SIF signals on the leaf surface ($SIF_{PSII\_leaf}$). We then used the escape probability of the SIF photons from the photosystems to the leaf surface (fLp) to further downscale $SIF_{PSII\_leaf}$ to the total SIF at the photosystem scale ($SIF_{PSII\_ps}$). In this study, we only employed the far-red SIF and regarded fLp as a constant (approximately 0.9) according to previous studies (Liu et al., 2022; Liu et al., 2020c; Lu et al., 2020). In summary, PSII SIF at the photosystem scale ($SIF_{PSII\_ps}$) was obtained using the following equation:

$$SIF_{PSII\_ps} = \frac{SIF_{PSII\_obs}}{fesc \times fLp} \quad (19)$$

Because the wavelength of SIF emission ranged from 650 to 800 nm, but $SIF_{PSII\_ps}$ only represents the SIF signal at the specific wavelength (745 to 758 nm for CA-obs and US-NR1 site, 760 nm for the KR-TCK site), we converted $SIF_{PSII\_ps}$ to obtain the total full-band PSII SIF ($SIF_{full}$, the integration of SIF in the wavelengths from 640 to 850nm, unit: μmol/m$^2$/s) to estimate photosynthesis according to a previous study (Liu et al., 2022):

$$SIF_{full} = \sum_{\lambda=640}^{850} \left( SIF_{PSII\_ps} \times fc(\lambda) \times \frac{\lambda \times 10^6}{h \times c \times N_A \times 10^3 \times 10^9} \right) \quad (20)$$

where $fc(\lambda)$ is the conversion factor used for calculating SIF at the $\lambda$ wavelength, $h$ is the Planck constant ($6.63 \times 10^{-34}$ J·s), c is the speed of light t ($3 \times 10^8$ m/s), λ is the wavelength (nm), and $N_A$ is the Avogadro constant ($6.02 \times 10^{23}$ mol$^{-1}$). The conversion factor $fc(\lambda)$ was determined by the first principal component of the PSII SIF spectrum simulations, as described by Liu (2022).

Combing equation 17, 19, and 20, we completed the conversion of observed SIF ($SIF_{obs}$) to full-band PSII SIF ($SIF_{full}$).

### 2.6 Determination of carbon-reaction-related parameters in GPP estimations

The carbon-reaction-related parameters in our MLR-based model refer to the intercellular $CO_2$ concentration (Ci) and the photocompensation point of $CO_2$ without dark respiration (Γ*). To estimate Γ*, we followed the previously described altitude-dependent temperature function (Bernacchi et al., 2001; G D Farquhar et al., 1980), and to estimate Ci, we used a method based on iteration.

To estimate Ci, we first selected records with PAR higher than the 90$^{th}$ percentile for each day and regarded the photosynthesis at that time as Rubisco-limited (the photosynthetic apparatus should be light-saturated when there is abundant light; otherwise, it is wasting energy to develop a high photosynthetic capacity that can seldom be reached). At this time, the actual GPP equals the Rubisco-limited GPP:

$$J \frac{C_i - \Gamma^*}{4C_i + 8\Gamma^*} = V_{cmax} \frac{C_i - \Gamma^*}{C_i + K} \quad (21)$$

Thus, we can calculate $V_{cmax}$ (maximum carboxylation rate) using the actual electron transport rate (J) estimated using $SIF_{full}$ and other biophysical properties of plants:

$$V_{cmax} = \mathrm{J}\frac{C_i + K}{4C_i + 8\Gamma^*} = \frac{(1 + k_{df})q_L\Phi_{PSIImax}(C_i + K)}{1 - \Phi_{PSIImax}(4C_i + 8\Gamma^*)}\, SIF_{full} \quad (22)$$

where K is the effective Michaelis–Menten coefficient of Rubisco-limited photosynthesis, which can be estimated using the Michaelis–Menten constants for the carboxylation and oxygenation reactions (Farquhar et al., 1980). In this equation, K, $\Gamma^*$, and $C_i$ are daily values calculated based on the average of records above the 90$^{th}$ percentile PAR, and all of their units are Pa. During this process, we excluded observations with 90$^{th}$ percentile PAR below 500 μmol/m$^2$/s and observations obtained on cloudy days (CI < 0.5) to ensure the Rubisco-limited condition; further, linear interpolation was conducted for the gap-filling of $V_{cmax}$. Then, based on the instantaneous temperature response of $V_{cmax}$, we converted $V_{cmax}$ to $V_{cmax25}$ (Kattge and Knorr, 2007), which will be used in the following iteration process to estimate the half-hourly real-time $C_i$.

Notably, $C_i$ in Equation 22 is a daily value calculated using a method based on the theory of optimal stomatal behavior (Harrison et al., 2021) and cannot capture the light response of stomata during diurnal cycles. Therefore, we used the following iteration to estimate the real-time $C_i$ for every half-hour record for comparison:

Step 1: Set the initial $C_i = 0.7 \times C_a$, where $C_a$ stands for the ambient $CO_2$ concentration;

Step 2: Estimate the net assimilation rate $A_{net}$ (the analog of GPP minus dark respiration at the leaf scale) using the following equation:

$$A_{net} = \mathrm{J}\frac{C_i - \Gamma^*}{4C_i + 8\Gamma^*} - R_d = \frac{(1 + k_{df})q_L\Phi_{PSIImax}(C_i - \Gamma^*)}{1 - \Phi_{PSIImax}(4C_i + 8\Gamma^*)}\, SIF_{full} - R_d \quad (23)$$

where Rd is the dark respiration derived from its temperature response and $R_{d25}$ (the dark respiration rate at 25 °C), and $R_{d25}$ equals $0.015 \times V_{cmax25}$.

Step 3: Estimate the stomatal conductance for $CO_2$ ($G_c$, unit: mol/m$^2$/s) according to previous studies on stomatal behavior (Wang and Leuning, 1998):

$$G_c = 0.64 \times (G_0 + \frac{(a-1) f_w A_{net}}{C_i \left(1 + \frac{VPD}{D_0}\right)}) \quad (24)$$

where $G_0$ is the residual conductance (0.01, unit: mol/m$^2$/s); a is a parameter related to $CO_2$ diffusion on the leaf surface, which is assumed to be 11; fw is related to the soil moisture and is taken as 1; VPD is the vapor pressure deficit (unit: kPa); and $D_0$ is regarded as a constant showing the stomatal sensitivity to VPD (1.5, unit: kPa).

Step 4: Update $C_i$ using the diffusion model (Ju et al., 2006):

$$C_i = C_a - \frac{A_{net}}{G_c} \quad (25)$$

By repeating Steps 2–4 until $C_i$ becomes stable, we can obtain the final half-hourly $C_i$. This iteration was performed for every leaf group (both sunlit and shaded leaves for the two-leaf model and all leaves at different canopy depths for the layered model) to consider the impact of light conditions on gas exchange. The estimations using this method to calculate $C_i$ were labeled with the suffix "_iter".

In this study, we also used another simple method to estimate $C_i$ for comparison (Shan et al., 2021):

$$C_i = \frac{3C_a\Gamma^* - \Gamma^* \frac{1.6VPD}{\lambda} - C_a\sqrt{3\Gamma^* \frac{1.6VPD}{\lambda}}}{3\Gamma^* - \frac{1.6VPD}{\lambda}} \quad (26)$$

where $\lambda$ is a parameter describing the marginal water cost of plant carbon assimilation, and the unit of VPD in this equation is hPa. Because $\lambda$ is almost constant for a specific vegetation type, we simply used $\lambda$ = 900 in this study. Compared to the iterative method, this simple method does not consider the possible influence of light conditions on stomatal closure. The estimations using this simple λ-based method to calculate $C_i$ were labeled with the suffix "_lambda".

Finally, for comparison, we also used two empirical SIF-based GPP models to estimate GPP: one of them used the linear regression to fit the SIF—GPP relationship, and the other used a

nonlinear function (quadratic function) to describe the SIF—GPP relationship. GPP estimates from the linear model are GPP_linear, and GPP estimates from the model are GPP_nonlinear.

## 3. Results

### 3.1 Performances of different SIF-based GPP estimation models

In this study, we used different strategies to describe the interaction between light and canopy structure to estimate the half-hourly (or hourly) GPP from tower-based SIF observations at three ENFs. Here, we evaluated and compared the performances of these different models, and the results are shown in Figure 1.

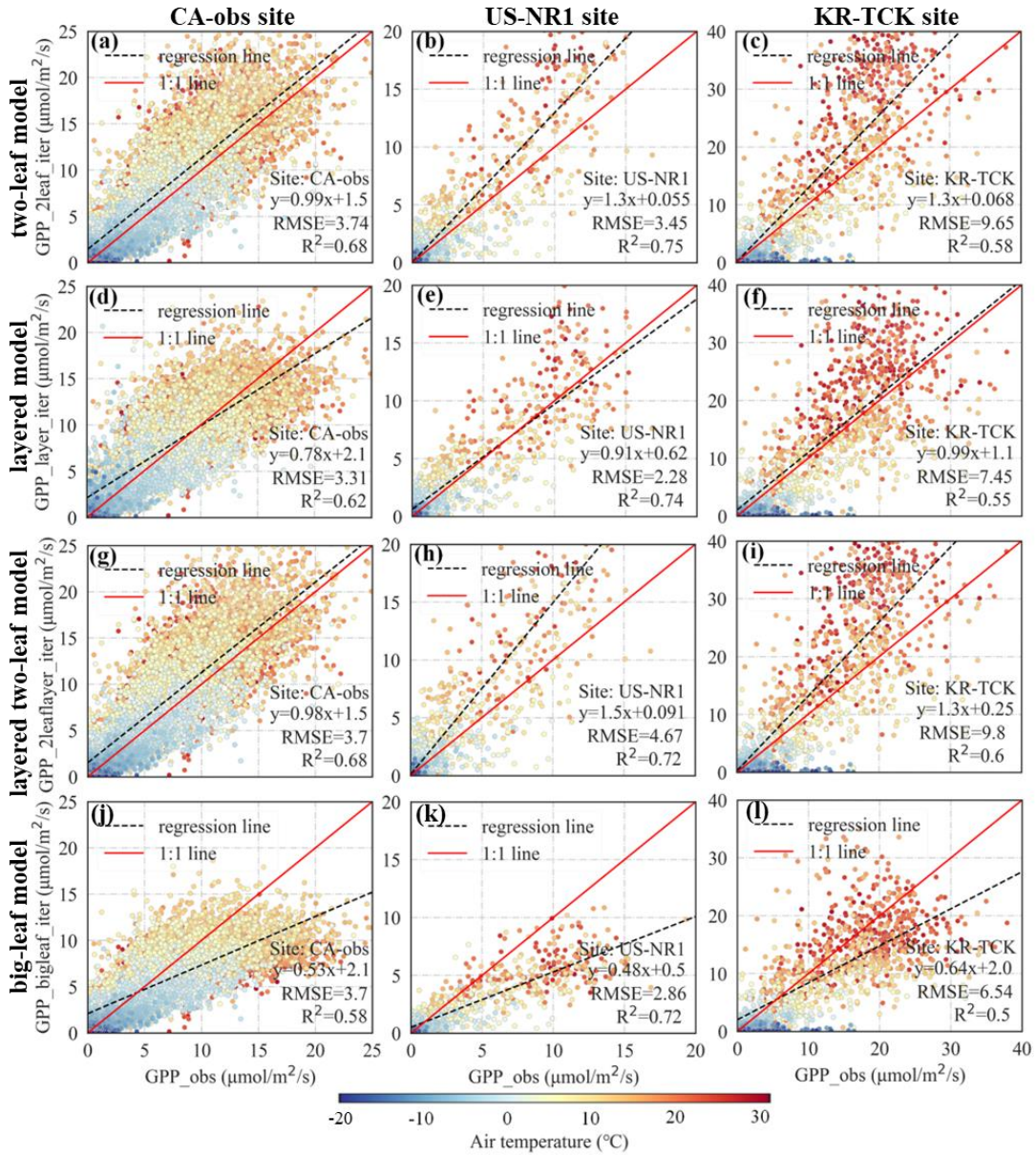


491

492 Figure 1. The performance of different models in estimating the half-hourly (or hourly) GPP.
493 Each row represents the results of different methods, and each column represents the results
494 of different ENF sites. (a)-(c), (d)-(f), (g)-(i), and (j)-(l) show the performance of the two-leaf,
495 layered, layered two-leaf, and big-leaf models, respectively. The figures in the first column show
496 the GPP estimation tested at the CA-obs site, the figures in the second column show the results
497 of the US-NR1 site, and those in the last column show the results of the KR-TCK site. All GPP
498 estimations in this figure used the iterative method to estimate Ci. The color of the dots

represents the corresponding air temperature, the dashed black line is the regression line, and the solid red line is the 1:1 line.

As displayed in the last row (Figure 1j-1l), the big-leaf model significantly underestimated GPP and had the lowest $R^2$ among the tested models. For all three sites in this study, GPP estimations from the big-leaf model exhibited a nonlinear relationship with GPP observations, and the slopes of the regression lines indicated that the big-leaf assumption would lead to approximately 45% underestimation, especially when the GPP value was high. In contrast, the models with a better description of the vertical or horizontal light distribution (including the layered model, the two-leaf model, and the layered two-leaf model) showed better performances (Figure 1a-1i), and the GPP estimates showed more linear relationships with the observed values. For the CA-obs site, the two-leaf model (Figure 1a) showed the best performance, with $R^2 = 0.68$, and a regression line close to the 1:1 line (slope:0.99); for the US-NR1 and KR-TCK sites, although the two-leaf model had high $R^2$, the layered model showed regression lines closest to the 1:1 line (for US-NR1, slope = 0.91; for KR-TCK, slope = 0.99). Compared with the results of the layered model, the GPP estimates from the two-leaf model were higher when the GPP and temperature were high (according to the distribution of scatters) and lower when the GPP and temperature were low (according to the interception of regression lines). Although the layered two-leaf model also avoided the underestimation problem and had a relatively high $R^2$, it did not show better performance than the two-leaf model at the CA-obs and US-NR1 sites and even increased the overall RMSE at the US-NR1 and KR-TCK sites. We also tested the results of different models using the simple λ-based method for $C_i$ estimation (Figure S3) and obtained similar results. In addition, we investigated the model's performance under sunny (clearness index >0.5) and cloudy conditions (clearness index <0.5) and found that the results do not change significantly (Figures S4-S5).

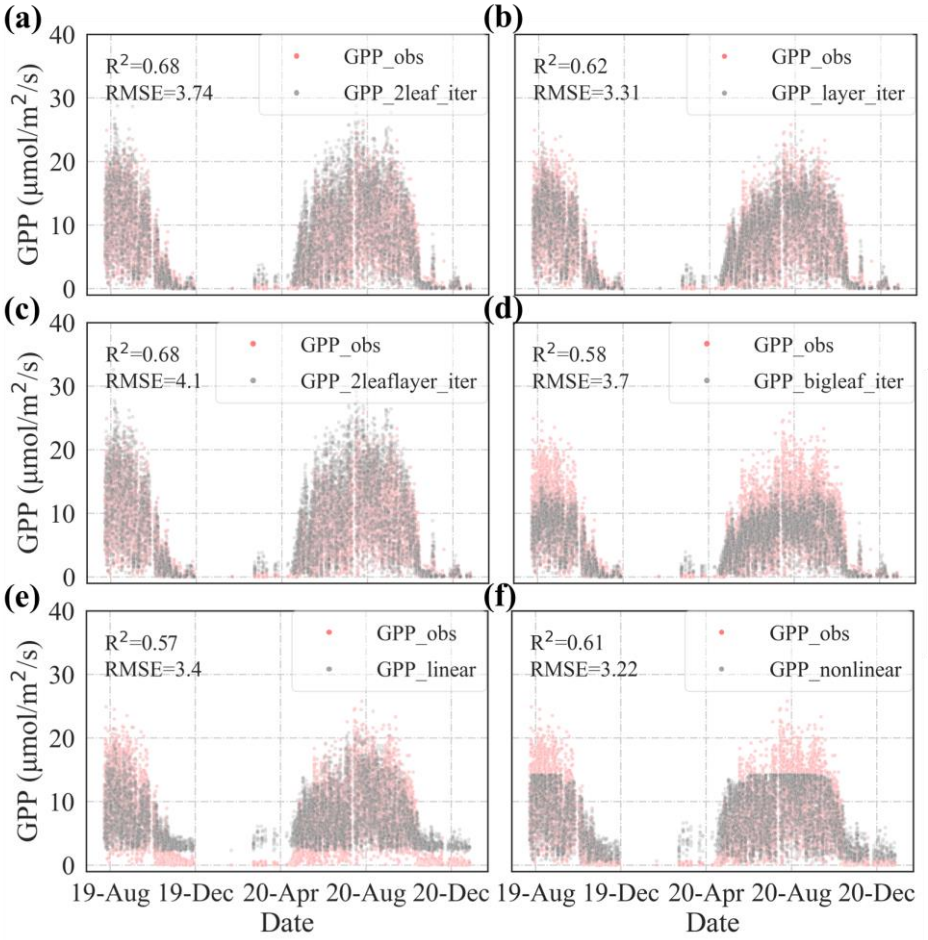


524

525 Figure 2. Time series of GPP observations and GPP estimates from the (a) two-leaf, (b) layered,
526 (c) layered two-leaf, (d) big-leaf, and (e) linear models using the empirical linear relationship
527 between SIF and GPP and from the (f) nonlinear model based on the empirical relationship
528 between SIF and GPP. The grey dots represent the half-hourly observations, and the pink dots
529 represent the GPP estimates. Here, we only displayed the results from the CA-obs site using
530 the iterative method for estimating Ci.

531
532 Figure 2 shows the time series of the observed and estimated GPP of different models. Here,
533 we can see that the two-leaf, layered, and layered two-leaf models all managed to capture the
534 dynamics of GPP observations, and there was no significant difference among their
535 performances (Figure 2a-2c). However, the big-leaf model underestimated GPP, which was
especially significant during the middays of summer (Figure 2d). In addition, empirical models

based on the empirical relationship between SIF and GPP also failed to track the dynamics of half-hourly GPP. In Figure 2e, the linear model overestimated the low GPP values during the entire study period. In Figure 3f, the nonlinear model showed truncation when the GPP estimation reached a certain value (~ 15 μmol/$m^2$/s) and thus underestimated the high GPP values in summer. Furthermore, the nonlinear model also overestimated the low GPP values, even though this overestimation problem in the nonlinear model was not as significant as that in the linear model.

Further analysis of the difference between the big-leaf and two-leaf models showed that their discrepancy was higher under conditions with high light intensity (and thereby higher GPP). Compared to environmental factors such as VPD and temperature, PAR showed the highest correlation with GPP bias (GPP estimation from the two-leaf model minus GPP estimations from the big-leaf model; $R^2$ = 0.15; Figure S6a), whereas the GPP relative bias (obtained by dividing GPP bias by GPP values) showed a much lower correlation with PAR ($R^2$ = 0.001, Figure S6b). Similarly, the difference between the big-leaf and layered models was also highly related to incident light. In addition, while a better description of the light–structure–physiology interaction within the canopy improved the accuracy of GPP estimation (Figure 1, 2), we found that the estimation of $C_i$ did not influence the results significantly (Figure 1 vs. Figure S3). Indeed, there was a difference in the GPP estimations using different $C_i$ estimations, and it showed a high correlation with VPD, but this difference was very small. Therefore, the uncertainties caused by the change in stomatal behavior under different light conditions (which influences $C_i$) were not the most important factor influencing GPP estimation at the half-hourly scale.

### 3.2 Diurnal dynamics of GPP estimations from different models

As the intensity and angle of incident light change significantly during the day, the within-canopy illumination and its distribution vary with time, which may thereby modify the diurnal dynamics of the whole-canopy GPP and its estimation. Figure 3 shows the dynamics of the observed and estimated GPP from different models during the day (composited using all observations during the study period). Although the GPP estimations using iterative methods

to calculate $C_i$ were slightly higher than those obtained using the simple λ-based method at midday, there was high consistency in GPP estimations using different $C_i$ calculation methods (Figure 3a-d, GPP_lambda vs. GPP_iter). In contrast, the diurnal dynamics of GPP estimates from models assuming different light–structure–physiology interactions varied significantly. GPP estimations from both the two-leaf and layered two-leaf models tracked the bell-shaped dynamics of GPP observations (Figure 3a, 3c), but the layered model underestimated GPP at midday and overestimated GPP in the early morning and late afternoon (Figure 3b). As depicted in Figure 3d, the big-leaf model showed the most significant underestimation at midday but performed well when the light was relatively weak (before 8:00 and after 18:00). In contrast to their poor performance in Figure 2, both the empirical linear and nonlinear models tracked the diurnal dynamics of GPP well (Figure 3e, 3f), probably because they were based on the statistical relationship and were thus able to capture the "overall" pattern.

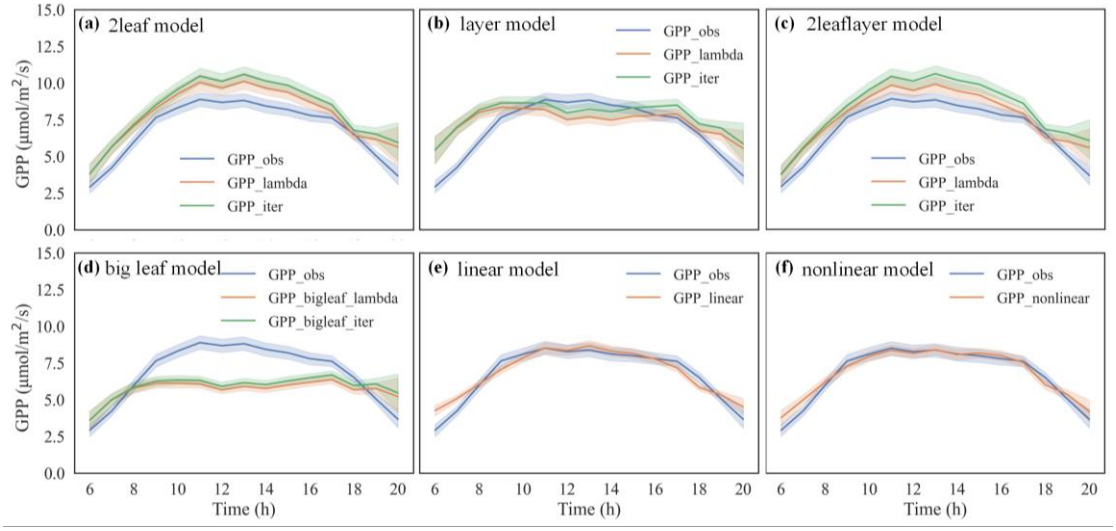


Figure 3. Diurnal dynamics of GPP observation and GPP estimates from (a) the two-leaf, (b) layered, (c) layered two-leaf, (d) big-leaf, (e) linear, and (f) nonlinear models. Variables with the suffix "_iter" refer to GPP estimation with $C_i$ estimated using the iterative method, and variables with the suffix "_lambda" refer to GPP estimation with $C_i$ estimated via the simple λ-based method. This figure shows the results from the CA-obs site using all of the half-hourly data obtained during the entire study period. The solid lines represent the average dynamics, and

the shaded areas represent 95% confidence intervals. Similar results were obtained at the other sites.

In Figure 4, we selected two sunny days during summer to further examine the differences in GPP estimations using the big-leaf model and other models. On those two days, PAR, SIF, and GPP showed "bell-shaped" patterns (Figure 4d, 4f, 4g), even though GPP had higher uncertainty and exhibited a less-smooth curve. Similar to the results in Figure 3, the layered, two-leaf, and layered two-leaf models all capture the midday increase in GPP, whereas the big-leaf model underestimated the GPP from 8:00 to 17:00 (Figure 4a-4c). This underestimation was more significant when the PAR was higher and was not significantly related to temperature changes, as exhibited in Figure 4e (because the temperature kept increasing in the afternoon, but the underestimation was weaker at that time). We further investigated the daily cycles of the estimated J/SIF ratio and J using the big-leaf model to understand the reasons for its poor performance. Figure 4h shows a significant midday reduction in the J/SIF ratio estimated by the big-leaf model, and Figure 4e indicates that the big-leaf assumption "suppressed" the ratio so strongly that even the estimated J (which equals J/SIF ratio times SIF) cannot capture the midday increase in photosynthesis.

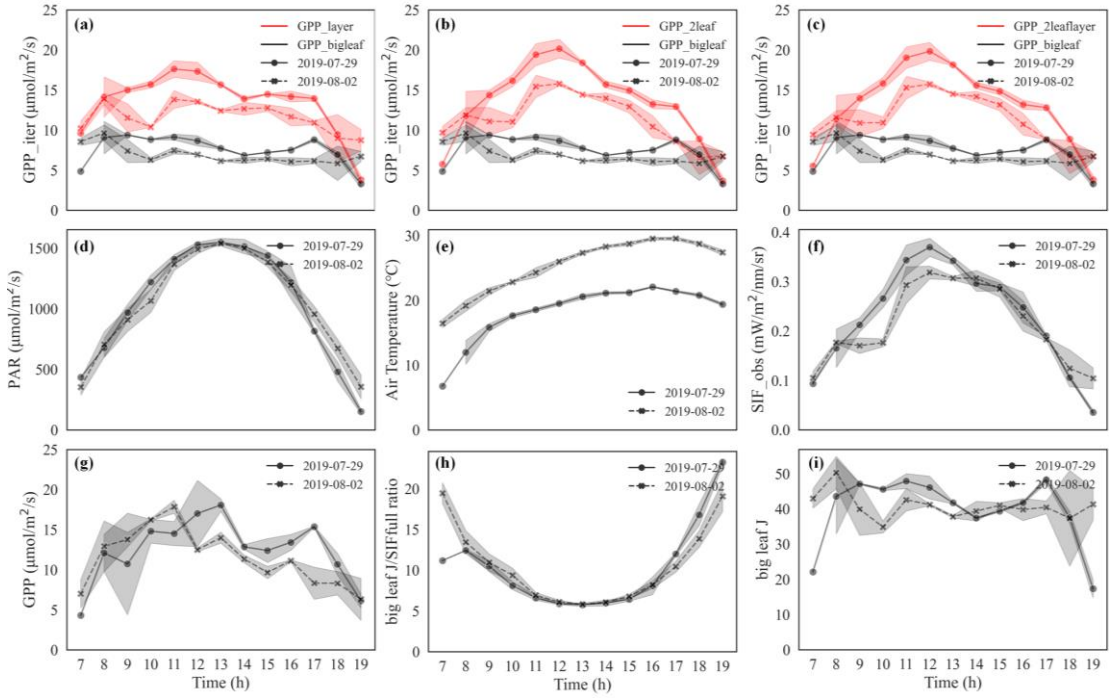


Figure 4. Comparison between the diurnal dynamics of GPP estimations from the big-leaf

model and the (a) layered, (b) two-leaf, and (c) layered two-leaf models and the corresponding (d) incident PAR, (e) temperature, (f) SIF, and (g) GPP on July 29, 2019, and August 2, 2019. (h) shows the changes in estimated J/SIF ratio, and (i) shows the dynamics of estimated J using the big-leaf model. The shaded areas represent the 95% interval. All the data used in this figure were obtained from the CA-obs half-hourly dataset.

### 3.3 Diurnal dynamics of GPP in different canopy layers (under different light conditions)

Due to the changing illumination and its distribution in the canopy, photosynthesis from different leaf groups (specifically, in different layers or under different light conditions) varies during the day, leading to the heterogeneity of GPP within the canopy. In Figure 5, we investigated the vertical variation in the diurnal dynamics of GPP estimations in each layer (depth) of the canopy to determine the reason for the midday underestimation and early morning overestimation in the layered model (as indicated in Figure 3b and 4a). Figure 5a and 5b display the estimated GPP dynamics derived from the layered model on July 29, 2019, and August 2, 2019, respectively. The results showed that the layered model successfully captured the increased GPP at noon in the bottom layers but showed a significant reduction in midday GPP in the top layers. Therefore, the discrepancy between GPP estimation from the layered model and GPP observations (Figure 3b) was mainly related to its unsatisfactory estimation in the top layers. The underestimation problem in the top layers (the top 5) was so severe that the GPP estimations even exhibited a reduction trend at noon and became smaller than the GPP estimations in the bottom layers. However, the results derived from the layered two-leaf model showed an increase in GPP at noon in both the bottom and top layers (Figure 5c and 5d). As the only difference between these two models was their assumption of light distribution, the different results in Figure 5a and 5c, 5b, and 5d indicated that the description of light–canopy–physiological interaction was important in the half-hourly GPP estimations, especially when considering the diurnal patterns of photosynthesis. The layered model assumes that all the leaves were not shaded and received direct light (even though the light decayed when it

penetrated the canopy); thus, this model may have overestimated the overall high light stress on the top leaves and "over-penalized" their qL at midday; simultaneously, because it does not consider that gaps among leaves could cause light spots in the deep canopy and high light conditions for some leaves, it might have underestimated the overall light condition in the bottom layers and thus slightly overestimated the qL and thereby GPP in the bottom layers at noon.

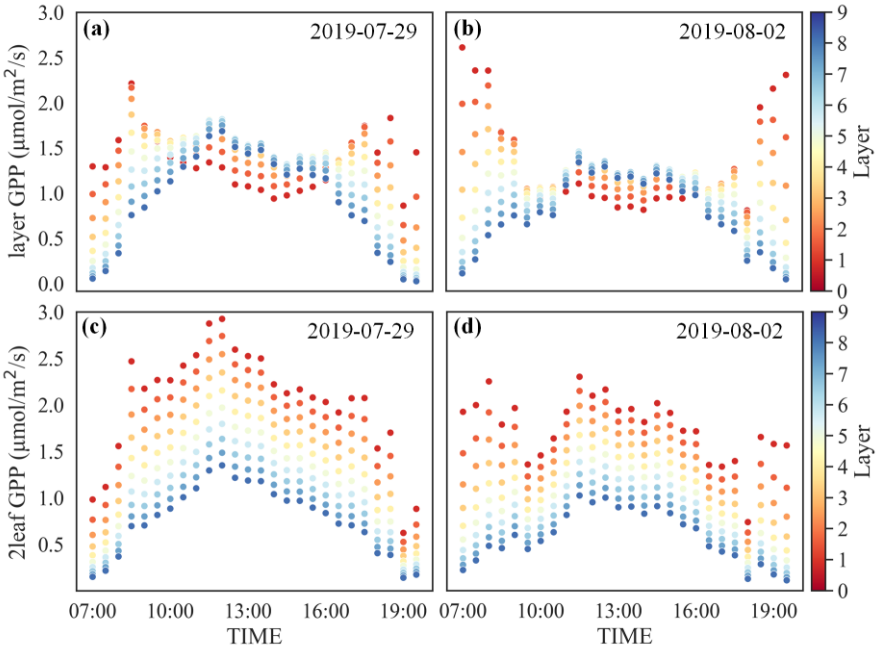


Figure 5. Diurnal dynamics of GPP estimation in different layers. The GPP estimations in (a) and (b) came from the layered model, and the GPP estimations in (c) and (d) came from the layered two-leaf model. The color of the dots represents the layer index, and a larger number represents a deeper location within the canopy. The LAI of each layer in this figure can be calculated as total LAI/10.

To investigate the dynamic distribution of GPP within the canopy, we further studied the depths of the layer above which the leaves contributed 80% of the total GPP during two sunny days (Figure 6). Using the vertical GPP estimations displayed in Figure 5, we found that both the layered and layered two-leaf models indicated that the GPP contribution at midday came from deeper layers than that in the morning or afternoon, which led to the "bell-shaped" curve in

Figure 6a and 6b. That is, the incident PAR (including direct and diffused fractions) can penetrate deeper into the canopy at noon and trigger increased photosynthesis in the bottom layer leaves. The deepest 80% GPP contribution depth estimated from the layered model is 8, which is slightly deeper than the depth of 7 from the layered two-leaf model; meanwhile, the 80% GPP contribution depths before 8:00 and after 18:00 estimated by the layered model were shallower than those estimated by the layered two-leaf model, which may relate to the lack of consideration of diffused light in the layered model.

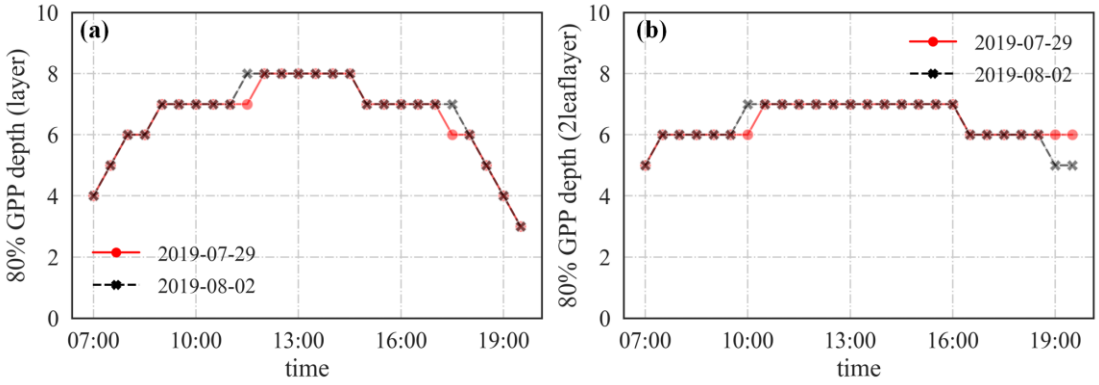


Figure 6. Depths of the layer above which the leaves contributed 80% of the total GPP on July 29, 2019, and August 2, 2019. Data used for depth estimation and plotting were half-hourly estimations from (a) the layered model and (b) the layered two-leaf model at the CA-obs site.

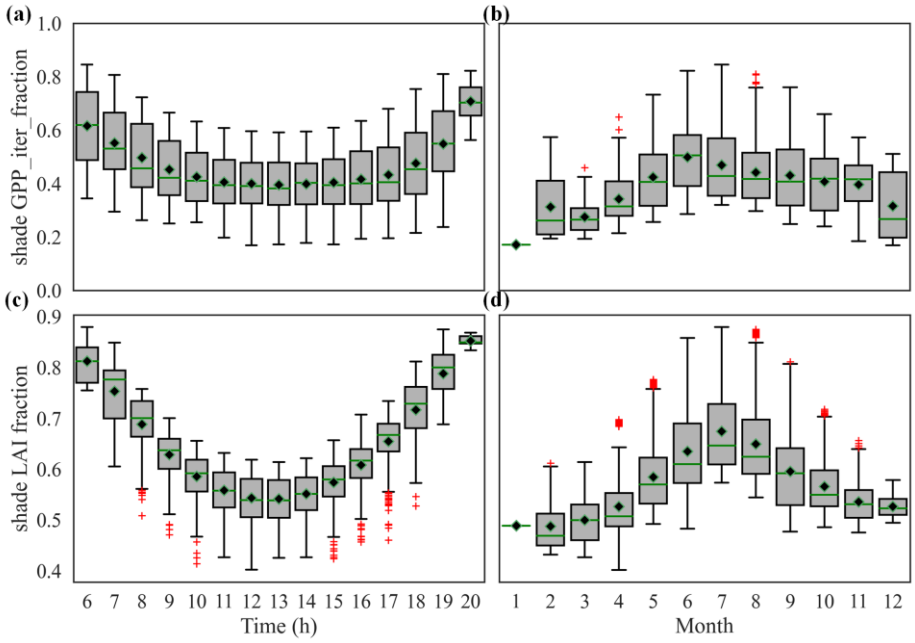

Figure 7. (a) Diurnal variation in the GPP contribution of shaded leaves; (b) seasonal variation in the GPP contribution of shaded leaves; (c) diurnal variation in the LAI fraction of shaded leaves; (d) seasonal variation in the LAI fraction of shaded leaves. The cross-marks in the plots represent the outliers, the black dots represent the mean values of each box, and the green lines represent the median values of each box.

In Figure 7a and 7b, we investigated the diurnal change in the GPP contribution of the shaded leaves and compared it with their seasonal dynamics. Here, we found that the GPP fraction from shaded leaves decreased in the morning and increased in the afternoon, while it increased from spring to summer and decreased from autumn to winter. These dynamics were consistent with the dynamics of the shaded LAI fraction at the diurnal and seasonal scales displayed in Figure 7c and 7d, respectively. These results indicate that the contribution of shaded leaves was more important in the morning and afternoon, when there was an apparent change in the solar zenith angle during the day; however, at the seasonal scale, the denser canopy led to a higher shaded LAI fraction and thus made GPP from shaded leaves (which used diffused light for photosynthesis) more crucial in summer. According to the result in Figure 7a, we deduced that the reason for the higher contribution of the bottom layers at noon in Figure 6b (compared to the morning and evening) should not only be attributed to the increase in the total intensity of diffused light but also to the direct light penetrating to the deeper layers through the gaps among leaves (indicated by the increase in the sunlit leaf fraction and reduction in the shaded leaf fraction) at midday.

### 3.4 Comparison of single-leaf qL and “canopy-scale qL”

To clarify the possible differences between single-leaf qL and canopy-scale qL, we used the framework of the big-leaf model but GPP estimations from the layered model or layered two-leaf model as input to calculate the canopy-scale qL. Figure 8 shows the different light responses of single-leaf qL (red dots), canopy-scale qL calculated from the results of the two-leaf model (pink dots), and canopy-scale qL calculated from the results of the layered model

682 (gray dots). Compared to the canopy-scale qL, the single-leaf qL (directly estimated using
683 Equation 4) was more sensitive to the change in illumination and showed a faster decrease as
684 the incident light increased. The scatterplot also showed that the distribution of canopy-scale
685 qL from the two-leaf model was more dispersed than that of the canopy-scale qL from the
686 layered model, which should be attributed to their different description of light–structure–
687 physiology interactions because both of them used the same function (Equation 4) to estimate
688 the qL of individual leaf groups.

689

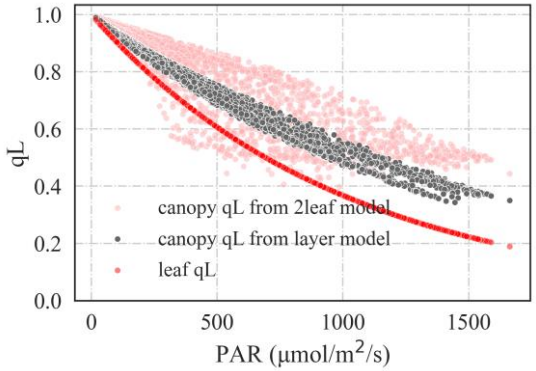


690

691 Figure 8. The light response of single-leaf qL (in red), canopy-scale qL obtained from the
692 layered model (in gray), and canopy-scale qL from the two-leaf model (in pink). The PAR label
693 of the x-axis refers to the incident PAR obtained at the top of the canopy.

694 We further investigated how LAI impacts the light response of canopy-scale qL estimated from
695 the two-leaf model in Figure 9a (and the canopy-scale qL estimated from the layered model in
696 Figure S7). We found that the LAI largely explained the variation in the light response of canopy
697 qL and that a higher LAI corresponded to a less-sensitive light response of canopy qL (a less-
698 steep slope in the relationship between qL and PAR) (Figure 9 and S5). We further compared
699 the canopy-scale qL of sunlit leaves (using GPP of sunlit leaves) and that of shaded leaves
700 (Figure 9b, 9c) and found that the qL of the shaded leaves showed a less-sensitive response to
701 changes in light than sunlit leaves and that the impact of LAI on the light response of canopy-
702 scale qL was more significant for sunlit leaves.

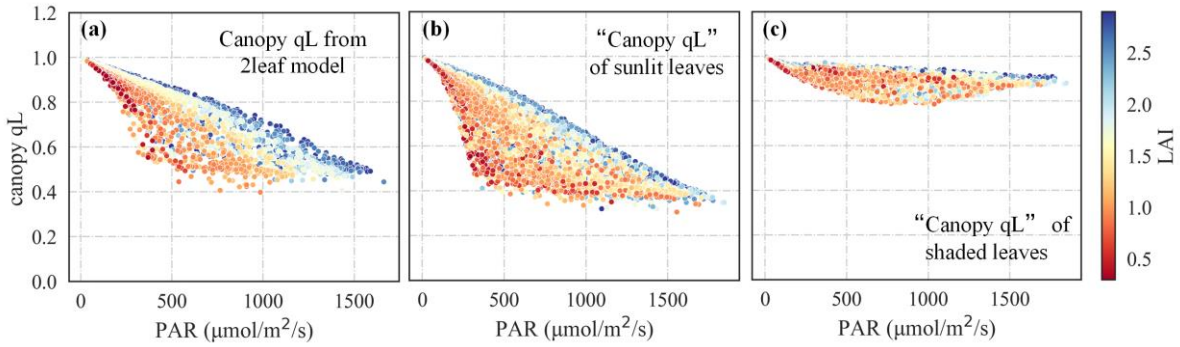


703

704 Figure 9. The impact of LAI on the light response of the (a) canopy-scale qL from the two-leaf

705 model; (b) canopy-scale qL of sunlit leaves; (c) canopy-scale qL of shaded leaves. The color of

706 the dots represents the corresponding LAI. The PAR label of the x-axis refers to the incident

707 PAR obtained at the top of the canopy.

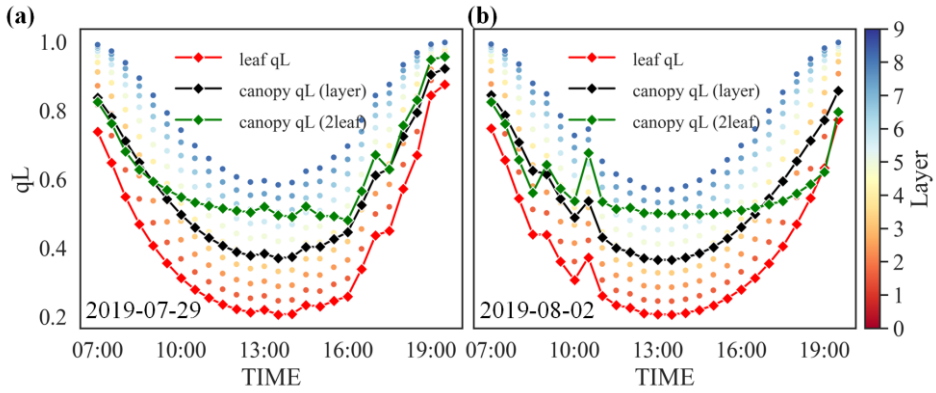


708

709 Figure 10. The diurnal patterns of single-leaf qL (red lines), canopy qL from the layered model

710 (black lines), canopy-scale qL from the two-leaf model (green lines), and the qL in different

711 layers of the canopy (colored scatters). The color of the dots represents the layer index, and

712 the larger number represents the deeper location within the canopy. The LAI of each layer in

713 this figure can be calculated as total LAI/10.

714 Using the observations from two sunny days, we compared the diurnal patterns of single-leaf

715 qL, canopy qL from the layered model, canopy-scale qL from the two-leaf model, and qL in

716 different canopy layers in Figure 10. Here, we found that the single leaf showed the same pattern

as the qL in the first layer of the canopy, with lower values than those in the other layers due to their higher light exposure (the incident PAR at the top of the canopy). The qL values in the top layers were higher than those in the bottom layers, and the difference was greater at noon. The canopy-scale qL from the layered model showed moderate qL dynamics (compared to the qL in the top and bottom layers) and was lower than the canopy-scale qL from the two-leaf model at noon. The differences in these qL dynamics indicated that the interaction between light and canopy structure (which leads to light redistribution within the canopy) could influence the dynamics of canopy-scale qL (the "overall qL") and that underestimation of GPP in big-leaf models could be mainly attributed to the utility of single-leaf qL rather than the canopy-scale qL during calculation.

## 4. Discussion

In this study, we found that employing the big-leaf assumption in the SIF-based GPP estimation would lead to significant underestimation at the half-hourly scale (Figure 1j-1l, Figure 2d), and this underestimation mainly appeared under intense light conditions (at noon), which thereby distorted the diurnal patterns of estimated GPP (Figure 3d, Figure 4a-4c). However, when the interaction of light, canopy structure, and plants' physiological factors was considered to provide a more accurate description of the light redistribution within the canopy, the accuracy of half-hourly GPP estimation could be significantly improved, and the estimation results could better capture the diurnal pattern of GPP (Figure 1a-1i, Figure 2a-2c, and Figure 3a-3c). The success of our attempt demonstrated that the unsuitable description of light–structure–physiologica interactions in the big-leaf model is responsible for the poor estimation of the J/SIF ratio (Figure 4h-4i), thereby influencing the half-hourly GPP estimation.

Due to the shading and absorption effects in the radiation transmission process, incident light is attenuated from the top to the bottom of the canopy layers and causes vertical gradients of the light condition and photosynthesis within the canopy (Chen et al., 1999; Yang et al., 2021). During diurnal cycles, variation in the combination of light intensity and incident angle leads to the redistribution of light and changes the vertical gradients, which affects the dynamics of

qL at different canopy depths (Chang et al., 2021). This can be proved by the simulated diurnal patterns of PAR and qL (a crucial parameter in MLR-based GPP estimation models) in different layers under clear sky conditions (Figures S8 and S9). To clarify the impacts of the light intensity and incident angle (solar zenith angle) on the variation patterns of qL in different layers, we further controlled the variation in light intensity and incident angle by fixing them before the simulation and found that the dynamics of light and qL in the upper layers of the canopy were mainly influenced by the daily variation pattern of light intensity, whereas those in the lower layer were mainly influenced by the change in the incident angle (Figures S8 and S9). We also found that the difference in qL at different depths was greater at midday (smaller SZA) than in the morning and evening (larger SZA), which partly explained the more significant GPP underestimation at noon (Figure S9). Therefore, the pattern of qL results from interactions among light, canopy structure, and leaf physiology, which explains why considering this interaction improved the GPP estimation accuracy in our research.

Our study demonstrated that it is important to select a proper light-canopy interaction assumption when SIF is used to estimate the half-hourly GPP. The widely used big-leaf model assumes that the canopy is a big foliage, and thus, all of the leaves in the canopy are considered sunlit leaves and have the same physiological properties (Gu et al., 2019; Liu et al., 2022). Therefore, all the leaves in the canopy are considered to be under high-light conditions and even in a photoinhibition state at midday in summer. As there is a monotonical negative correlation between qL and light intensity (Han et al., 2022a; Liu et al., 2021), this assumption would make the qL "over-penalized" at noon, which causes underestimation of the high GPP values. In comparison, the layered model determines the light levels at different depths so that not all leaves are assumed to be in a high-light intensity state; thus, it improves the estimation accuracy and is more consistent with reality. The two-leaf model further counts the effects of direct light, diffused light, and the clumping condition of leaves to improve the model's accuracy. As the model assumes that only a fraction of leaves receives high-intensity direct light and that many other leaves are under milder diffused light, it describes the real condition well and can avoid significant underestimation under high-light conditions.

The two-leaf model and layered two-leaf model should be attributed to the merit of two-leaf

assumptions; however, we used this assumption here differently from that in previous studies. The two-leaf assumption has been applied in light use efficiency (LUE) photosynthetic modules integrated into terrestrial ecosystem models (e.g., BEPS models) or SIF simulation models in previous studies (Cui et al., 2020; Liu et al., 1997) and has been demonstrated to perform well (Zheng et al., 2020). Previous LUE models used different LUEs to describe the different physiological characteristics of sunlit and shaded leaves, and the LUE values ($LUE_{shade}$ and $LUE_{sun}$) were mostly obtained from calibration or empirical results. As the variations in the angle and intensity of incident light during the day alter the amount of light penetrating the lower canopy and lead to highly dynamic overall light conditions, the determination of $LUE_{shade}$ and $LUE_{sun}$ (which respond to the light condition) without the support of clear mechanisms will introduce uncertainty in the results. In contrast, our method contains a clear mechanistic expression of the SIF-GPP relationship. Except for the physiological information included in the SIF signal, we mainly used qL to capture the differences in the physiological properties of shaded and sunlit leaves. Because the difference in qL between shaded and sunlit leaves can be calculated directly using their incident light, our model can show the difference in the physiological characteristics of shaded and sunlit leaves more clearly and directly; thus, it can consider the fertilization effect of diffused light without the need for calibration. We acknowledge that other physiological factors may also contribute to the different photosynthetic capacities between sunlit and shaded leaves, but we do not consider these contributions in this study. Nevertheless, recent studies have proven the importance of considering the impact of light on LUE (Guan et al., 2022, 2021), and the good performance of their modified LUE model with radiation scalar confirmed that the differences in LUE between sunlit and shaded leaves are mainly caused by the differences in light conditions, which means that consideration of light impacts should be good enough to provide relatively accurate estimations.

Even though physiological differences remain between sunlit and shaded leaves that were not considered in this study, they may influence the performance of two-leaf models. As the different micro-environments and long-term adaptation may cause differences in physiological properties (such as the light response) of sunlit and shaded leaves, we evaluated this effect by using different qL light response curves in sunlit and shaded leaves (Chang et al., 2021) and

found that it did not significantly influence our results (Figure S10a,b vs. Figure 1a). In addition, we tried to assign SIF using APAR without considering the different physiological signals of sunlit and shaded leaves (sunlit ΦF vs. shaded ΦF), and we found that the effect was not significant (Figure S10c vs. Figure 1a). This result suggests that the differences or estimation uncertainty in the physiological signals in SIF (ΦF) do not significantly affect the GPP estimation from the two-leaf model, whereas the difference in qL matters.

Unlike other models proposed in this study, the big-leaf model directly uses the single-leaf qL to estimate GPP. However, the canopy-scale qL obtained from the relatively accurate GPP estimations in our study showed a lower sensitivity to incident light than the single-leaf qL (Figures 8 and 10). The light response of canopy-scale qL is influenced by LAI, but when the canopy density decreases (with low LAI), it is closer to the single-leaf pattern (Figures 8, 9a). Therefore, we deduce that the big-leaf assumption might be more acceptable for sparser canopies with simple structures but not for dense canopies with complex structures. In addition, as the light response of canopy-scale qL is too complicated to be described by merely one function (Figures 8 and 9), it might be inefficient to simply correct the leaf-scale response function (or even use another function type) and then apply it at the canopy scale. This result is echoed by a previous study showing depression in fluorescence at the leaf level but not in the canopy of a pine forest (Louis et al., 2006). In that study, the canopy structure also impacts the canopy-scale pattern by modulating the light penetrating into deeper canopy layers.

Although models with an improved description of the light–structure–physiology interactions in our study performed well in capturing the diurnal dynamics of GPP, we have to admit that there are still some uncertainties. First, we used satellite-based LAI rather than ground observations collected at each site in our study. The possible mismatch or error in these satellite data may affect the accuracy of GPP estimation. To clarify these problems, we replaced the GLASS LAI with the ground LAI measurement at the KR-TCK site (only this site had ground observation of LAI) and found that this did not significantly influence GPP estimation (Figure S11). Second, there were uncertainties in the satellite-based Ω dataset. Therefore, we also tested another satellite clumping index dataset at the CA-obs site and found that although there were differences in the clumping index results, this discrepancy was not passed down to the model

outputs (Figure S10d vs. Figure 1a). Third, although the comparison between Figure 1 and Figure S3 demonstrated that the methods used to estimate $C_i$ and the consideration of light response of stomatal behaviors do not introduce much difference in GPP estimation, and the iterative method still slightly increased the accuracy. Third, for the layered model, the number of layers (n) also influences the model performance, and we found that the increase in layer numbers increased the $R^2$, RMSE, and regression slope but reduced the regression interception of the relationship between the observed and estimated GPP (Figure S12). However, when the number of layers was greater than 320, it no longer impacted the accuracy of GPP estimation. For the layered model using the interactive method to estimate $C_i$, $R^2$ dropped significantly as the number of layers continued to increase after reaching 80, but this phenomenon was not found in the layered model using the simple λ-based method. This result indicated that using the interactive method makes the model more sensitive to uncertainties in SIF (SIF in each layer has larger uncertainty as the number of layers increases), even though it had a higher $R^2$ compared to the simple λ-based method. Finally, although we employed the widely accepted Lambert–Beer's law and the method proposed by Chen et al. (1999), uncertainty remains in the description of vertical variation in light. For the quantification of such uncertainty, we employed the 3-D Discrete Anisotropic Radiative Transfer Model (DART) to validate the PAR estimation in each layer for three different scenes (Appendix A). The results demonstrated the effectiveness of Lambert–Beer's law in describing the vertical profile of PAR for ENF sites ($R^2$ higher than 0.9; Figures A1, A2). However, the results also indicated that violating the canopy homogenous assumption in the real world would undermine the effectiveness of Lambert–Beer's law, leading to a less-credible estimation of light distribution in relatively sparse and highly heterogeneous canopies. Nevertheless, the key point of this study is to highlight the importance of considering vertical light distribution when using SIF to estimate GPP. Although we only used the 1-D radioactive transfer models and highly simplified the canopy structure in this study, the GPP estimates still showed high consistency with the GPP observation. In the future, combining 3-D models and Lidar measurements would enable a more accurate estimation of the PAR profile, thereby assisting in a more accurate estimation of GPP via SIF.

There are also some limitations in our study. Although the layered model and two-leaf model

considered the vertical and horizontal heterogeneity of light conditions and leaf biophysical properties (mainly the redox state of PSII reaction centers indicated by qL), they do not indicate that we thoroughly considered the variations in leaf biophysical properties. The inherent differences in leaves (for example, age, status, and nutrient conditions) were not considered. In this study, we used the empirical relationship between PAR and qL; however, previous studies have shown that temperature could also influence qL (Han et al., 2021). We could not consider the impacts of temperature heterogeneity or other environmental factors within the canopy, mainly because of the lack of a modeled relationship between qL and temperature and the difficulty in obtaining the temperature distribution in canopies. This might make the models incapable of reproducing photoinhibition under high temperatures, which probably explains the decreased GPP in the afternoon of August 2, 2019, at the CA-obs site (Figure 4g). In addition, none of the models in our study considered the contribution of understory species, but they are important for the total photosynthesis of the whole ecosystem (Nunes et al., 2022). As there are many non-photosynthetic organisms (such as branches and trunks) that block light transmission within the canopy, the woody fraction, the space among trees, and the orientation of the terrain slope are also issues that need further consideration (Chang et al., 2021).

## 5. Conclusion

In this study, we developed SIF-based GPP estimation models with different descriptions of light–structure–physiological interactions, including a layered model, a two-leaf model, and a layered two-leaf model. We compared their performances with the big-leaf model on a half-hourly scale at three ENF sites. The results showed that the big-leaf model significantly underestimated the half-hourly GPP. The underestimation mainly occurred at midday, which distorted the diurnal dynamics of the estimated GPP. In contrast, the layered model, two-leaf model, and layered two-leaf model all improved the estimation accuracy. Compared with the layered model, both the two-leaf model and the layered two-leaf model showed daily patterns closer to reality, with no significant differences between them. We further investigated the diurnal dynamics of GPP and qL in different layers and found that the big-leaf and layered assumptions overestimated the overall light stress at noon and thus “over-penalized” qL,

leading to the underestimation of GPP. In the morning and afternoon, the leaves on the top layers of the canopy contributed significantly to the total GPP, but as the solar zenith angle decreased at noon, leaves from the deeper layers also played an important role. Finally, by comparing the single-leaf scale qL with the canopy-scale qL (obtained from relatively accurate GPP estimations), we demonstrated that the canopy-scale qL was less sensitive to light than the single-leaf scale qL and that the difference was larger for the shaded leaf group or when the LAI was high.

## Appendix

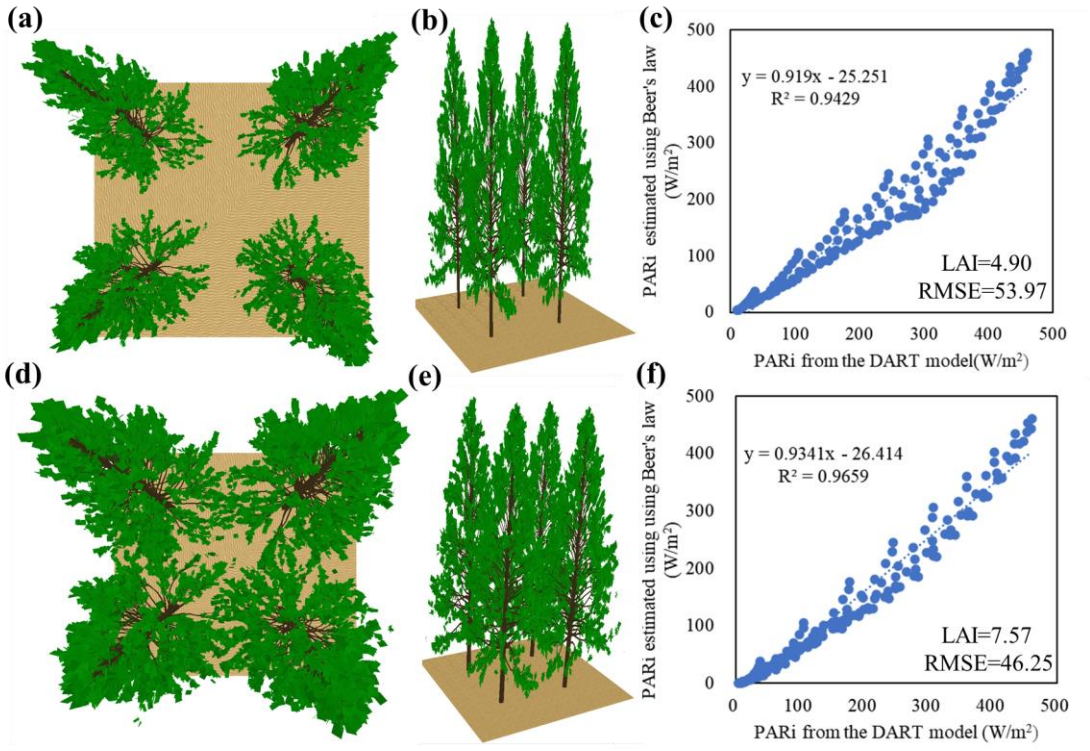


Figure A1. The nadir view (a, d) and the side view (b, e) of the 3-D scene, and the accuracy of $PAR_i$ estimated using Lambert–Beer's law (c, f). The method was examined in canopies with different densities. Canopies were divided into 16 layers, and the PAR in each layer ($PAR_i$ for layer i) was calculated when SZA =0°, 9°, 18°, 27°, 36°, 45°, 54°, 63°, 81°. (a-c) shows the condition in a relatively sparse canopy, and (d-f) shows the condition in a dense canopy.

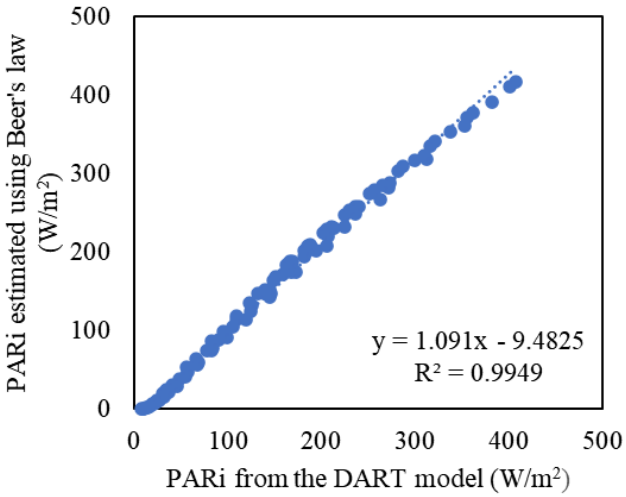


Figure A2. The accuracy of $PAR_i$ estimated using Lambert–Beer's law in a turbid canopy (more homogenous; LAI=2). PAR in each layer ($PAR_i$ for layer i) was calculated when SZA =0°, 9°, 18°, 27°, 36°, 45°, 54°, 63°, 81°.

## Conflicts of interest

The authors declare that they have no conflict of interest.

## Acknowledgement

We appreciate Prof. Juliane Bendig from Institute of Bio- and Geosciences, Plant Sciences, Forschungszentrum Jülich GmbH, Prof. Zbynek Malenovsky, Dr. Omar Regaieg, and Dr. Thang Nguyen from University of Bonn for their kind help in the technical details in the application of DART model. We also thanks Prof. Troy Magney from the University of California Davis, Dr Zoe Pierrat and Prof. Jochen Stutz from the University of California, Los Angeles, and Prof. Youngryel Ryu, Prof. Hyun Seok Kim from Seoul National University, and Dr. Jongmin Kim from University of Virginia, for they recommended datasets with high-quality. This research was funded by the National Natural Science Foundation of China (42071310) and the Innovative Research Program of the International Research Center of Big Data for Sustainable Development Goals (CBAS2022IRP01).

## References


Anav, A., Friedlingstein, P., Beer, C., Ciais, P., Harper, A., Jones, C., Murray-Tortarolo, G., Papale, D., Parazoo, N.C., Peylin, P., Piao, S., Sitch, S., Viovy, N., Wiltshire, A., Zhao, M., 2015. Spatiotemporal patterns of terrestrial gross primary production: A review. Rev. Geophys. https://doi.org/10.1002/2015RG000483

Barr, A.G., Black, T.A., Hogg, E.H., Kljun, N., Morgenstern, K., Nesic, Z., 2004. Inter-annual variability in the leaf area index of a boreal aspen-hazelnut forest in relation to net ecosystem production. Agric. For. Meteorol. https://doi.org/10.1016/j.agrformet.2004.06.011

Bernacchi, C.J., Singsaas, E.L., Pimentel, C., Portis, A.R., Long, S.P., 2001. Improved temperature response functions for models of Rubisco-limited photosynthesis. Plant, Cell Environ. https://doi.org/10.1046/j.1365-3040.2001.00668.x

Cai, W., Yuan, W., Liang, S., Zhang, X., Dong, W., Xia, J., Fu, Y., Chen, Y., Liu, D., Zhang, Q., 2014. Improved estimations of gross primary production using satellite-derived photosynthetically active radiation. J. Geophys. Res. Biogeosciences. https://doi.org/10.1002/2013JG002456

Chang, C.Y., Wen, J., Han, J., Kira, O., LeVonne, J., Melkonian, J., Riha, S.J., Skovira, J., Ng, S., Gu, L., Wood, J.D., Näthe, P., Sun, Y., 2021. Unpacking the drivers of diurnal dynamics of sun-induced chlorophyll fluorescence (SIF): Canopy structure, plant physiology, instrument configuration and retrieval methods. Remote Sens. Environ. 265. https://doi.org/10.1016/j.rse.2021.112672

Chen, J.M., Liu, J., Cihlar, J., Goulden, M.L., 1999. Daily canopy photosynthesis model through temporal and spatial scaling for remote sensing applications. Ecol. Modell. 124, 99–119. https://doi.org/10.1016/s0304-3800(99)00156-8

Chen, R., Liu, L., Liu, X., 2022a. Leaf chlorophyll contents dominates the seasonal dynamics of SIF/GPP ratio: Evidence from continuous measurements in a maize field. Agric. For. Meteorol. 323, 109070. https://doi.org/10.1016/j.agrformet.2022.109070

Chen, R., Liu, X., Chen, J., Du, S., Liu, L., 2022b. Solar-induced chlorophyll fluorescence imperfectly

945 tracks the temperature response of photosynthesis in winter wheat. J. Exp. Bot. erac388.
946 https://doi.org/10.1093/jxb/erac388

947 Ciais, P., Reichstein, M., Viovy, N., Granier, A., Ogée, J., Allard, V., Aubinet, M., Buchmann, N.,
948 Bernhofer, C., Carrara, A., Chevallier, F., De Noblet, N., Friend, A.D., Friedlingstein, P.,
949 Grünwald, T., Heinesch, B., Keronen, P., Knohl, A., Krinner, G., Loustau, D., Manca, G.,
950 Matteucci, G., Miglietta, F., Ourcival, J.M., Papale, D., Pilegaard, K., Rambal, S., Seufert, G.,
951 Soussana, J.F., Sanz, M.J., Schulze, E.D., Vesala, T., Valentini, R., 2005. Europe-wide reduction
952 in primary productivity caused by the heat and drought in 2003. Nature 437, 529–533.
953 https://doi.org/10.1038/nature03972

954 Cui, T., Sun, R., Xiao, Z., Liang, Z., Wang, J., 2020. Simulating spatially distributed solar-induced
955 chlorophyll fluorescence using a BEPS-SCOPE coupling framework. Agric. For. Meteorol. 295,
956 108169. https://doi.org/10.1016/j.agrformet.2020.108169

957 Damm, A., Guanter, L., Paul-Limoges, E., van der Tol, C., Hueni, A., Buchmann, N., Eugster, W.,
958 Ammann, C., Schaepman, M.E., 2015. Far-red sun-induced chlorophyll fluorescence shows
959 ecosystem-specific relationships to gross primary production: An assessment based on
960 observational and modeling approaches. Remote Sens. Environ.
961 https://doi.org/10.1016/j.rse.2015.06.004

962 Du, S., Liu, L., Liu, X., Hu, J., 2017. Response of canopy solar-induced chlorophyll fluorescence to the
963 absorbed photosynthetically active radiation absorbed by chlorophyll. Remote Sens. 9, 911.

964 Farquhar, G. D., von Caemmerer, S., Berry, J.A., 1980. A biochemical model of photosynthetic CO2
965 assimilation in leaves of C3 species. Planta 149, 78–90. https://doi.org/10.1007/BF00386231

966 Farquhar, G D, von Caemmerer, S., Berry, J.A., 1980. A biochemical model of photosynthetic
967 CO<Subscript>2</Subscript> assimilation in leaves of C<Subscript>3</Subscript> species.
968 Planta.

969 Feng, H., Xu, T., Liu, L., Zhou, S., Zhao, J., Liu, S., Xu, Z., Mao, K., He, X., Zhu, Z., Chai, L., 2021.
970 Modeling transpiration with sun- induced chlorophyll fluorescence observations via carbon-
971 water coupling methods. Remote Sens. https://doi.org/10.3390/rs13040804

Friedlingstein, P., O'Sullivan, M., Jones, M.W., Andrew, R.M., Hauck, J., Olsen, A., Peters, G.P., Peters, W., Pongratz, J., Sitch, S., Le Quéré, C., Canadell, J.G., Ciais, P., Jackson, R.B., Alin, S., Aragão, L.E.O.C., Arneth, A., Arora, V., Bates, N.R., Becker, M., Benoit-Cattin, A., Bittig, H.C., Bopp, L., Bultan, S., Chandra, N., Chevallier, F., Chini, L.P., Evans, W., Florentie, L., Forster, P.M., Gasser, T., Gehlen, M., Gilfillan, D., Gkritzalis, T., Gregor, L., Gruber, N., Harris, I., Hartung, K., Haverd, V., Houghton, R.A., Ilyina, T., Jain, A.K., Joetzjer, E., Kadono, K., Kato, E., Kitidis, V., Korsbakken, J.I., Landschützer, P., Lefèvre, N., Lenton, A., Lienert, S., Liu, Z., Lombardozzi, D., Marland, G., Metzl, N., Munro, D.R., Nabel, J.E.M.S., Nakaoka, S.I., Niwa, Y., O'Brien, K., Ono, T., Palmer, P.I., Pierrot, D., Poulter, B., Resplandy, L., Robertson, E., Rödenbeck, C., Schwinger, J., Séférian, R., Skjelvan, I., Smith, A.J.P., Sutton, A.J., Tanhua, T., Tans, P.P., Tian, H., Tilbrook, B., Van Der Werf, G., Vuichard, N., Walker, A.P., Wanninkhof, R., Watson, A.J., Willis, D., Wiltshire, A.J., Yuan, W., Yue, X., Zaehle, S., 2020. Global Carbon Budget 2020. Earth Syst. Sci. Data. https://doi.org/10.5194/essd-12-3269-2020

Grossmann, K., Frankenberg, C., Magney, T.S., Hurlock, S.C., Seibt, U., Stutz, J., 2018. Remote Sensing of Environment PhotoSpec : A new instrument to measure spatially distributed red and far- red Solar-Induced Chlorophyll Fluorescence. Remote Sens. Environ. 216, 311–327. https://doi.org/10.1016/j.rse.2018.07.002

Gu, L., Han, J., Wood, J.D., Chang, C.Y.Y., Sun, Y., 2019. Sun-induced Chl fluorescence and its importance for biophysical modeling of photosynthesis based on light reactions. New Phytol. 223, 1179–1191. https://doi.org/10.1111/nph.15796

Guan, X., Chen, J.M., Shen, H., Xie, X., 2021. A modified two-leaf light use efficiency model for improving the simulation of GPP using a radiation scalar. Agric. For. Meteorol. 307, 108546. https://doi.org/10.1016/j.agrformet.2021.108546

Guan, X., Chen, J.M., Shen, H., Xie, X., Tan, J., 2022. Comparison of big-leaf and two-leaf light use efficiency models for GPP simulation after considering a radiation scalar. Agric. For. Meteorol. 313, 108761. https://doi.org/10.1016/j.agrformet.2021.108761

Guanter, L., Bacour, C., Schneider, A., Aben, I., Kempen, T.A. Van, Retscher, C., Köhler, P., Frankenberg, C., Joiner, J., 2021. Sentinel-5P TROPOMI mission 202104, 1–27.

Han, J., Chang, C.Y., Gu, L., Zhang, Y., Meeker, E.W., Magney, T.S., Walker, A.P., Wen, J., Kira, O., McNaull, S., Sun, Y., 2022a. The physiological basis for estimating photosynthesis from Chl a fluorescence. New Phytol. https://doi.org/10.1111/nph.18045

Han, J., Chang, C.Y.Y., Gu, L., Zhang, Y., Meeker, E.W., Magney, T.S., Walker, A.P., Wen, J., Kira, O., McNaull, S., Sun, Y., 2022b. The physiological basis for estimating photosynthesis from Chla fluorescence. New Phytol. https://doi.org/10.1111/nph.18045

Han, J., Gu, L., Warren, J.M., Guha, A., Mclennan, D.A., Zhang, W., Zhang, Y., 2021. The roles of photochemical and non-photochemical quenching in regulating photosynthesis depend on the phases of fluctuating light conditions. Tree Physiol. 1–14. https://doi.org/10.1093/treephys/tpab133

Harrison, S.P., Cramer, W., Franklin, O., Prentice, I.C., Wang, H., Brännström, Å., de Boer, H., Dieckmann, U., Joshi, J., Keenan, T.F., Lavergne, A., Manzoni, S., Mengoli, G., Morfopoulos, C., Peñuelas, J., Pietsch, S., Rebel, K.T., Ryu, Y., Smith, N.G., Stocker, B.D., Wright, I.J., 2021. Eco-evolutionary optimality as a means to improve vegetation and land-surface models. New Phytol. 231, 2125–2141. https://doi.org/10.1111/nph.17558

He, M., Ju, W., Zhou, Y., Chen, J., He, H., Wang, S., Wang, H., Guan, D., Yan, J., Li, Y., Hao, Y., Zhao, F., 2013. Development of a two-leaf light use efficiency model for improving the calculation of terrestrial gross primary productivity. Agric. For. Meteorol. 173, 28–39. https://doi.org/10.1016/j.agrformet.2013.01.003

Helm, L.T., Shi, H., Lerdau, M.T., Yang, X., 2020. Solar-induced chlorophyll fluorescence and short-term photosynthetic response to drought. Ecol. Appl. 30, 1–12. https://doi.org/10.1002/eap.2101

Jiao, Z., Dong, Y., Schaaf, C.B., Chen, J.M., Román, M., Wang, Z., Zhang, H., Ding, A., Erb, A., Hill, M.J., Zhang, X., Strahler, A., 2018. An algorithm for the retrieval of the clumping index (CI) from the MODIS BRDF product using an adjusted version of the kernel-driven BRDF model. Remote Sens. Environ. https://doi.org/10.1016/j.rse.2018.02.041

Joiner, J., Yoshida, Y., Guanter, L., Middleton, E.M., 2016. New methods for retrieval of chlorophyll red fluorescence from hyper-spectral satellite instruments: simulations and application to GOME-

2 and SCIAMACHY. Atmos. Meas. Tech. Discuss. https://doi.org/10.5194/amt-2015-387

Joiner, J., Yoshida, Y., Vasilkov, A.P., Yoshida, Y., Corp, L.A., Middleton, E.M., 2011. First observations of global and seasonal terrestrial chlorophyll fluorescence from space. Biogeosciences. https://doi.org/10.5194/bg-8-637-2011

Ju, W., Chen, J.M., Black, T.A., Barr, A.G., Liu, J., Chen, B., 2006. Modelling multi-year coupled carbon and water fluxes in a boreal aspen forest. Agric. For. Meteorol. https://doi.org/10.1016/j.agrformet.2006.08.008

Jung, M., Koirala, S., Weber, U., Ichii, K., Gans, F., Camps-Valls, G., Papale, D., Schwalm, C., Tramontana, G., Reichstein, M., 2019. The FLUXCOM ensemble of global land-atmosphere energy fluxes. Sci. Data. https://doi.org/10.1038/s41597-019-0076-8

Kattge, J., Knorr, W., 2007. Temperature acclimation in a biochemical model of photosynthesis: A reanalysis of data from 36 species. Plant, Cell Environ. https://doi.org/10.1111/j.1365-3040.2007.01690.x

Kim, J., Ryu, Y., Dechant, B., Lee, H., Kim, H.S., Kornfeld, A., Berry, J.A., 2021a. Solar-induced chlorophyll fluorescence is non-linearly related to canopy photosynthesis in a temperate evergreen needleleaf forest during the fall transition. Remote Sens. Environ. 258, 112362. https://doi.org/10.1016/j.rse.2021.112362

Kim, J., Ryu, Y., Dechant, B., Lee, H., Seok, H., Kornfeld, A., Berry, J.A., 2021b. Solar-induced chlorophyll fluorescence is non-linearly related to canopy photosynthesis in a temperate evergreen needleleaf forest during the fall transition. Remote Sens. Environ. 258, 112362. https://doi.org/10.1016/j.rse.2021.112362

Li, X., Xiao, J., 2020. Global climatic controls on interannual variability of ecosystem productivity: Similarities and differences inferred from solar-induced chlorophyll fluorescence and enhanced vegetation index. Agric. For. Meteorol. 288–289, 108018. https://doi.org/10.1016/j.agrformet.2020.108018

Li, Y., Fang, H., 2022. Real-Time Software for the Efficient Generation of the Clumping Index and Its Application Based on the Google Earth Engine. Remote Sens. 14, 3837.

Liu, J., Chen, J.M., Cihlar, J., Park, W.M., 1997. A process-based boreal ecosystem productivity simulator using remote sensing inputs. Remote Sens. Environ. https://doi.org/10.1016/S0034-4257(97)00089-8

Liu, L., Guan, L., Liu, X., 2017. Agricultural and Forest Meteorology Directly estimating diurnal changes in GPP for C3 and C4 crops using far-red sun-induced chlorophyll fluorescence. Agric. For. Meteorol. 232, 1–9. https://doi.org/10.1016/j.agrformet.2016.06.014

Liu, L., Liu, X., Chen, J., Du, S., Ma, Y., Qian, X., Chen, S., Peng, D., 2020. Estimating Maize GPP using Near-infrared Radiance of Vegetation. Sci. Remote Sens. 2, 100009. https://doi.org/10.1016/j.srs.2020.100009

Liu, X., Liu, L., Hu, J., Guo, J., Du, S., 2020. Improving the potential of red SIF for estimating GPP by downscaling from the canopy level to the photosystem level. Agric. For. Meteorol. 281, 107846. https://doi.org/10.1016/j.agrformet.2019.107846

Liu, X., Liu, Z., Liu, L., Lu, X., Chen, J., Du, S., Zou, C., 2021. Modelling the influence of incident radiation on the SIF-based GPP estimation for maize. Agric. For. Meteorol. 307, 108522. https://doi.org/10.1016/j.agrformet.2021.108522

Liu, Z., Zhao, F., Liu, X., Yu, Q., Wang, Y., Peng, X., Cai, H., Lu, X., 2022. Direct estimation of photosynthetic CO2 assimilation from solar-induced chlorophyll fluorescence (SIF). Remote Sens. Environ. 271, 112893. https://doi.org/10.1016/j.rse.2022.112893

Lu, X., Liu, Z., Zhao, F., Tang, J., 2020. Comparison of total emitted solar-induced chlorophyll fluorescence (SIF) and top-of-canopy (TOC) SIF in estimating photosynthesis. Remote Sens. Environ. https://doi.org/10.1016/j.rse.2020.112083

Luijkx, I., Velde, I.R., Krol, M., Gatti, L., Domingues, L., S. C. Correia, C., Miller, J., Gloor, M., Leeuwen, T., Kaiser, J., Wiedinmyer, C., Basu, S., Clerbaux, C., Peters, W., 2015. Response of the Amazon carbon balance to the 2010 drought derived with CarbonTracker South America. Global Biogeochem. Cycles 29. https://doi.org/10.1002/2014GB005082

Magney, T.S., Barnes, M.L., Yang, X., 2020. On the Covariation of Chlorophyll Fluorescence and Photosynthesis Across Scales. Geophys. Res. Lett. 47, e2020GL091098.

https://doi.org/10.1029/2020GL091098

Magney, Troy S, Bowling, D.R., Logan, B., Grossmann, K., Stutz, J., Blanken, P., 2019. Mechanistic evidence for tracking the seasonality of photosynthesis with solar-induced fluorescence. Proc. Natl. Acad. Sci. In Press. https://doi.org/10.1073/pnas.1900278116

Magney, Troy S., Bowling, D.R., Logan, B.A., Grossmann, K., Stutz, J., Blanken, P.D., Burns, S.P., Cheng, R., Garcia, M.A., Köhler, P., Lopez, S., Parazoo, N.C., Raczka, B., Schimel, D., Frankenberg, C., 2019. Mechanistic evidence for tracking the seasonality of photosynthesis with solar-induced fluorescence. Proc. Natl. Acad. Sci. U. S. A. 116, 11640–11645. https://doi.org/10.1073/pnas.1900278116

Maguire, A.J., Eitel, J.U.H., Griffin, K.L., Magney, T.S., Long, R.A., Vierling, L.A., Schmiege, S.C., Jennewein, J.S., Weygint, W.A., Boelman, N.T., Bruner, S.G., 2020. On the Functional Relationship Between Fluorescence and Photochemical Yields in Complex Evergreen Needleleaf Canopies. Geophys. Res. Lett. 47, e2020GL087858. https://doi.org/10.1029/2020GL087858

Maia, V.A., Santos, A.B.M., de Aguiar-Campos, N., de Souza, C.R., de Oliveira, M.C.F., Coelho, P.A., Morel, J.D., da Costa, L.S., Farrapo, C.L., Fagundes, N.C.A., de Paula, G.G.P., Santos, P.F., Gianasi, F.M., da Silva, W.B., de Oliveira, F., Girardelli, D.T., de Carvalho Araújo, F., Vilela, T.A., Pereira, R.T., da Silva, L.C.A., de Oliveira Menino, G.C., Garcia, P.O., Fontes, M.A.L., dos Santos, R.M., 2020. The carbon sink of tropical seasonal forests in southeastern Brazil can be under threat. Sci. Adv. 6, eabd4548. https://doi.org/10.1126/sciadv.abd4548

Marrs, J.K., Reblin, J.S., Logan, B.A., Allen, D.W., Reinmann, A.B., Bombard, D.M., Tabachnik, D., Hutyra, L.R., 2020. Solar-Induced Fluorescence Does Not Track Photosynthetic Carbon Assimilation Following Induced Stomatal Closure. Geophys. Res. Lett. 47, 1–11. https://doi.org/10.1029/2020GL087956

McCallum, I., Franklin, O., Moltchanova, E., Merbold, L., Schmullius, C., Shvidenko, A., Schepaschenko, D., Fritz, S., 2013. Improved light and temperature responses for light-use-efficiency-based GPP models. Biogeosciences. https://doi.org/10.5194/bg-10-6577-2013

Miao, G., Guan, K., Yang, X., Bernacchi, C.J., Berry, J.A., DeLucia, E.H., Wu, J., Moore, C.E.,

Meacham, K., Cai, Y., Peng, B., Kimm, H., Masters, M.D., 2018. Sun-Induced Chlorophyll Fluorescence, Photosynthesis, and Light Use Efficiency of a Soybean Field from Seasonally Continuous Measurements. J. Geophys. Res. Biogeosciences. https://doi.org/10.1002/2017JG004180

Migliavacca, M., Musavi, T., Mahecha, M.D., Nelson, J.A., Knauer, J., Baldocchi, D.D., Perez-Priego, O., Christiansen, R., Peters, J., Anderson, K., Bahn, M., Black, T.A., Blanken, P.D., Bonal, D., Buchmann, N., Caldararu, S., Carrara, A., Carvalhais, N., Cescatti, A., Chen, J., Cleverly, J., Cremonese, E., Desai, A.R., El-Madany, T.S., Farella, M.M., Fernández-Martínez, M., Filippa, G., Forkel, M., Galvagno, M., Gomarasca, U., Gough, C.M., Göckede, M., Ibrom, A., Ikawa, H., Janssens, I.A., Jung, M., Kattge, J., Keenan, T.F., Knohl, A., Kobayashi, H., Kraemer, G., Law, B.E., Liddell, M.J., Ma, X., Mammarella, I., Martini, D., Macfarlane, C., Matteucci, G., Montagnani, L., Pabon-Moreno, D.E., Panigada, C., Papale, D., Pendall, E., Penuelas, J., Phillips, R.P., Reich, P.B., Rossini, M., Rotenberg, E., Scott, R.L., Stahl, C., Weber, U., Wohlfahrt, G., Wolf, S., Wright, I.J., Yakir, D., Zaehle, S., Reichstein, M., 2021. The three major axes of terrestrial ecosystem function. Nature. https://doi.org/10.1038/s41586-021-03939-9

Mohammed, G.H., Colombo, R., Middleton, E.M., Rascher, U., van der Tol, C., Nedbal, L., Goulas, Y., Pérez-Priego, O., Damm, A., Meroni, M., Joiner, J., Cogliati, S., Verhoef, W., Malenovský, Z., Gastellu-Etchegorry, J.P., Miller, J.R., Guanter, L., Moreno, J., Moya, I., Berry, J.A., Frankenberg, C., Zarco-Tejada, P.J., 2019. Remote sensing of solar-induced chlorophyll fluorescence (SIF) in vegetation: 50 years of progress. Remote Sens. Environ. 231, 111177. https://doi.org/10.1016/j.rse.2019.04.030

Monteith, J.L., Unsworth, M.H., 1990. Principles of environmental physics, 2nd Edition. Edward Arnold, London.

Morozumi, T., Kato, T., Kobayashi, H., Sakai, Y., Nakashima, N., Buareal, K., Nasahara, K.N., Akitsu, T.K., Murayama, S., Noda, H.M., Muraoka, H., 2023. Contributions of the understory and midstory to total canopy solar-induced chlorophyll fluorescence in a ground-based study in conjunction with seasonal gross primary productivity in a cool-temperate deciduous broadleaf forest. Remote Sens. Environ. https://doi.org/10.1016/j.rse.2022.113340

Nunes, M.H., Camargo, J.L.C., Vincent, G., Calders, K., Oliveira, R.S., Huete, A., Mendes de Moura, Y., Nelson, B., Smith, M.N., Stark, S.C., Maeda, E.E., 2022. Forest fragmentation impacts the seasonality of Amazonian evergreen canopies. Nat. Commun. 13. https://doi.org/10.1038/s41467-022-28490-7

Paul-Limoges, E., Damm, A., Hueni, A., Liebisch, F., Eugster, W., Schaepman, M.E., Buchmann, N., 2018. Effect of environmental conditions on sun-induced fluorescence in a mixed forest and a cropland. Remote Sens. Environ. 219, 310–323. https://doi.org/10.1016/j.rse.2018.10.018

Pierrat, Z., Magney, T., Parazoo, N.C., Grossmann, K., Bowling, D.R., Seibt, U., Johnson, B., Helgason, W., Barr, A., Bortnik, J., Norton, A., Maguire, A., Frankenberg, C., 2022a. Diurnal and Seasonal Dynamics of Solar-Induced Chlorophyll Fluorescence , Vegetation Indices , and Gross Primary Productivity in the Boreal Forest Journal of Geophysical Research : Biogeosciences. https://doi.org/10.1029/2021JG006588

Pierrat, Z., Magney, T., Parazoo, N.C., Grossmann, K., Bowling, D.R., Seibt, U., Johnson, B., Helgason, W., Barr, A., Bortnik, J., Norton, A., Maguire, A., Frankenberg, C., Stutz, J., 2022b. Diurnal and Seasonal Dynamics of Solar-Induced Chlorophyll Fluorescence, Vegetation Indices, and Gross Primary Productivity in the Boreal Forest. J. Geophys. Res. Biogeosciences 127. https://doi.org/10.1029/2021JG006588

Porcar-Castell, A., Tyystjärvi, E., Atherton, J., Van Der Tol, C., Flexas, J., Pfündel, E.E., Moreno, J., Frankenberg, C., Berry, J.A., 2014. Linking chlorophyll a fluorescence to photosynthesis for remote sensing applications: Mechanisms and challenges. J. Exp. Bot. 65, 4065–4095. https://doi.org/10.1093/jxb/eru191

Rajewicz, P.A., Zhang, C., Atherton, J., Wittenberghe, S. Van, Riikonen, A., Magney, T., Fernandez-marin, B., Ignacio, J., Plazaola, G., Porcar-castell, A., 2023. The photosynthetic response of spectral chlorophyll fluorescence differs across species and light environments in a boreal forest ecosystem. Agric. For. Meteorol. 334, 109434. https://doi.org/10.1016/j.agrformet.2023.109434

Reichstein, M., Falge, E., Baldocchi, D., Papale, D., Aubinet, M., Berbigier, P., Bernhofer, C., Buchmann, N., Gilmanov, T., Granier, A., Grünwald, T., Havránková, K., Ilvesniemi, H., Janous,

D., Knohl, A., Laurila, T., Lohila, A., Loustau, D., Matteucci, G., Meyers, T., Miglietta, F., Ourcival, J.M., Pumpanen, J., Rambal, S., Rotenberg, E., Sanz, M., Tenhunen, J., Seufert, G., Vaccari, F., Vesala, T., Yakir, D., Valentini, R., 2005. On the separation of net ecosystem exchange into assimilation and ecosystem respiration: Review and improved algorithm. Glob. Chang. Biol. 11, 1424–1439. https://doi.org/10.1111/j.1365-2486.2005.001002.x

Ryu, Y., Berry, J.A., Baldocchi, D.D., 2019. What is global photosynthesis? History, uncertainties and opportunities. Remote Sens. Environ. 223, 95–114. https://doi.org/10.1016/j.rse.2019.01.016

Schimel, D., Pavlick, R., Fisher, J.B., Asner, G.P., Saatchi, S., Townsend, P., Miller, C., Frankenberg, C., Hibbard, K., Cox, P., 2015. Observing terrestrial ecosystems and the carbon cycle from space. Glob. Chang. Biol. 21, 1762–1776.

Sellers, P.J., Berry, J.A., Collatz, G.J., Field, C.B., Hall, F.G., 1992. Canopy reflectance, photosynthesis, and transpiration. III. A reanalysis using improved leaf models and a new canopy integration scheme. Remote Sens. Environ. 42, 187–216.

Shan, N., Zhang, Y., Chen, J.M., Ju, W., Migliavacca, M., Peñuelas, J., Yang, X., Zhang, Z., Nelson, J.A., Goulas, Y., 2021. A model for estimating transpiration from remotely sensed solar-induced chlorophyll fluorescence. Remote Sens. Environ. 252. https://doi.org/10.1016/j.rse.2020.112134

Sun, Y., Frankenberg, C., Wood, J.D., Schimel, D.S., Jung, M., Guanter, L., Drewry, D.T., Verma, M., Porcar-Castell, A., Griffis, T.J., Gu, L., Magney, T.S., Köhler, P., Evans, B., Yuen, K., 2017. OCO-2 advances photosynthesis observation from space via solar-induced chlorophyll fluorescence. Science (80-. ). https://doi.org/10.1126/science.aam5747

Sun, Y., Fu, R., Dickinson, R., Joiner, J., Frankenberg, C., Gu, L., Xia, Y., Fernando, N., 2015. Drought onset mechanisms revealed by satellite solar-induced chlorophyll fluorescence: Insights from two contrasting extreme events. J. Geophys. Res. G Biogeosciences 120, 2427–2440. https://doi.org/10.1002/2015JG003150

Swoczyna, T., Bussotti, F., Swoczyna, T., Kalaji, H.M., Bussotti, F., Mojski, J., Pollastrini, M., 2022. Environmental stress -what can we learn from chlorophyll a fluorescence Environmental stress - what can we learn from chlorophyll a fl uorescence analysis in woody plants ? A review.

https://doi.org/10.3389/fpls.2022.1048582

Van Der Tol, C., Berry, J.A., Campbell, P.K.E., Rascher, U., 2014. Models of fluorescence and photosynthesis for interpreting measurements of solar-induced chlorophyll fluorescence. J. Geophys. Res. Biogeosciences 119, 2312–2327. https://doi.org/10.1002/2014JG002713

Vitale, L., Arena, C., Virzo de Santo, A., 2012. Seasonal changes in photosynthetic activity and photochemical efficiency of the Mediterranean shrub Phillyrea angustifolia L. Plant Biosyst. https://doi.org/10.1080/11263504.2011.651507

Wang, S., Zhang, Y., Ju, W., Chen, J.M., Ciais, P., Cescatti, A., Sardans, J., Janssens, I.A., Wu, M., Berry, J.A., Campbell, E., Fernández-Martínez, M., Alkama, R., Sitch, S., Friedlingstein, P., Smith, W.K., Yuan, W., He, W., Lombardozzi, D., Kautz, M., Zhu, D., Lienert, S., Kato, E., Poulter, B., Sanders, T.G.M., Krüger, I., Wang, R., Zeng, N., Tian, H., Vuichard, N., Jain, A.K., Wiltshire, A., Haverd, V., Goll, D.S., Peñuelas, J., 2020. Recent global decline of CO2 fertilization effects on vegetation photosynthesis. Science (80-. ). 370, 1295–1300. https://doi.org/10.1126/science.abb7772

Wang, S., Zhang, Y., Ju, W., Wu, M., Liu, L., 2022a. Temporally corrected long-term satellite solar-induced fluorescence leads to improved estimation of global trends in vegetation photosynthesis during ISPRS Journal of Photogrammetry and Remote Sensing Temporally corrected long-term satellite solar-induced. https://doi.org/10.1016/j.isprsjprs.2022.10.018

Wang, S., Zhang, Y., Ju, W., Wu, M., Liu, L., He, W., Peñuelas, J., 2022b. Temporally corrected long-term satellite solar-induced fluorescence leads to improved estimation of global trends in vegetation photosynthesis during 1995–2018. ISPRS J. Photogramm. Remote Sens. 194, 222–234. https://doi.org/https://doi.org/10.1016/j.isprsjprs.2022.10.018

Wang, Y.P., Leuning, R., 1998. A two-leaf model for canopy conductance, photosynthesis and partitioning of available energy I: Model description and comparison with a multi-layered model. Agric. For. Meteorol. https://doi.org/10.1016/S0168-1923(98)00061-6

Wutzler, T., Lucas-Moffat, A., Migliavacca, M., Knauer, J., Sickel, K., Šigut, L., Menzer, O., Reichstein, M., 2018. Basic and extensible post-processing of eddy covariance flux data with

REddyProc. Biogeosciences 15, 5015–5030. https://doi.org/10.5194/bg-15-5015-2018

Xiao, J., Chevallier, F., Gomez, C., Guanter, L., Hicke, J.A., Huete, A.R., Ichii, K., Ni, W., Pang, Y., Rahman, A.F., Sun, G., Yuan, W., Zhang, L., Zhang, X., 2019. Remote sensing of the terrestrial carbon cycle: A review of advances over 50 years. Remote Sens. Environ. 233, 111383. https://doi.org/10.1016/j.rse.2019.111383

Xiao, Z., Liang, S., Wang, J., Chen, P., Yin, X., Zhang, L., Song, J., 2014. Use of general regression neural networks for generating the GLASS leaf area index product from time-series MODIS surface reflectance. IEEE Trans. Geosci. Remote Sens. https://doi.org/10.1109/TGRS.2013.2237780

Yang, J.C., Magney, T.S., Albert, L.P., Richardson, A.D., Frankenberg, C., Stutz, J., Grossmann, K., Burns, S.P., Seyednasrollah, B., Blanken, P.D., Bowling, D.R., 2022. Gross primary production ( GPP ) and red solar induced fluorescence ( SIF ) respond differently to light and seasonal environmental conditions in a subalpine conifer forest. Agric. For. Meteorol. 317, 108904. https://doi.org/10.1016/j.agrformet.2022.108904

Yang, P., Prikaziuk, E., Verhoef, W., Van Der Tol, C., 2021. SCOPE 2.0: A model to simulate vegetated land surface fluxes and satellite signals. Geosci. Model Dev. 14, 4697–4712. https://doi.org/10.5194/gmd-14-4697-2021

Zaks, J., Amarnath, K., Kramer, D.M., Niyogi, K.K., Fleming, G.R., 2012. A kinetic model of rapidly reversible nonphotochemical quenching. Proc. Natl. Acad. Sci. U. S. A. 109, 15757–15762. https://doi.org/10.1073/pnas.1211017109

Zeng, Y., Badgley, G., Dechant, B., Ryu, Y., Chen, M., Berry, J.A., 2019. A practical approach for estimating the escape ratio of near-infrared solar-induced chlorophyll fluorescence. Remote Sens. Environ. https://doi.org/10.1016/j.rse.2019.05.028

Zhang, Y., Parazoo, N.C., Williams, A.P., Zhou, S., Gentine, P., 2020. Large and projected strengthening moisture limitation on end-of-season photosynthesis. Proc. Natl. Acad. Sci. U. S. A. 117, 9216–9222. https://doi.org/10.1073/pnas.1914436117

Zhang, Y., Xiao, X., Wu, X., Zhou, S., Zhang, G., Qin, Y., Dong, J., 2017. A global moderate

resolution dataset of gross primary production of vegetation for 2000-2016. Sci. data. https://doi.org/10.1038/sdata.2017.165

Zhang, Z., Chen, J.M., Zhang, Y., Li, M., 2023. Improving the ability of solar-induced chlorophyll fluorescence to track gross primary production through differentiating sunlit and shaded leaves. Agric. For. Meteorol. 341, 109658. https://doi.org/10.1016/j.agrformet.2023.109658

Zhang, Z., Zhang, Y., Porcar-Castell, A., Joiner, J., Guanter, L., Yang, X., Migliavacca, M., Ju, W., Sun, Z., Chen, S., 2020. Reduction of structural impacts and distinction of photosynthetic pathways in a global estimation of GPP from space-borne solar-induced chlorophyll fluorescence. Remote Sens. Environ. 240, 111722.

Zheng, Y., Shen, R., Wang, Y., Li, X., Liu, S., Liang, S., Chen, J.M., Ju, W., Zhang, L., Yuan, W., 2020. Improved estimate of global gross primary production for reproducing its long-Term variation, 1982-2017. Earth Syst. Sci. Data 12, 2725–2746. https://doi.org/10.5194/essd-12-2725-2020

Zhu, K., Chen, J., Wang, S., Fang, H., Chen, B., Zhang, L., Li, Y., Zheng, C., Amir, M., 2023. Characterization of the layered SIF distribution through hyperspectral observation and SCOPE modeling for a subtropical evergreen forest. ISPRS J. Photogramm. Remote Sens. 201, 78–91. https://doi.org/10.1016/j.isprsjprs.2023.05.014

Zhuang, J., Wang, Y., Chi, Y., Zhou, L., Chen, J., Zhou, W., Song, J., Zhao, N., Ding, J., 2020. Drought stress strengthens the link between chlorophyll fluorescence parameters and photosynthetic traits. PeerJ 8, 1–20. https://doi.org/10.7717/peerj.10046

## List of Figure Captions

**Figure 1**. The performance of different models in estimating the half-hourly (or hourly) GPP. Each row represents the results of different methods, and each column represents the results of different ENF sites. (a)-(c), (d)-(f), (g)-(i), and (j)-(l) show the performance of the two-leaf, layered, layered two-leaf, and big-leaf models, respectively. The figures in the first column show the GPP estimation tested at the CA-obs site, the figures in the second column show the

results of the US-NR1 site, and those in the last column show the results of the KR-TCK site. All GPP estimations in this figure used the iterative method to estimate Ci. The color of the dots represents the corresponding air temperature, the dashed black line is the regression line, and the solid red line is the 1:1 line.

**Figure 2.** Time series of GPP observations and GPP estimates from the (a) two-leaf, (b) layered, (c) layered two-leaf, (d) big-leaf, and (e) linear models using the empirical linear relationship between SIF and GPP and from the (f) nonlinear model based on the empirical relationship between SIF and GPP. The grey dots represent the half-hourly observations, and the pink dots represent the GPP estimates. Here, we only displayed the results from the CA-obs site using the iterative method for estimating Ci.

**Figure 3.** Diurnal dynamics of GPP observation and GPP estimates from (a) the two-leaf, (b) layered, (c) layered two-leaf, (d) big-leaf, (e) linear, and (f) nonlinear models. Variables with the suffix "_iter" refer to GPP estimation with $C_i$ estimated using the iterative method, and variables with the suffix "_lambda" refer to GPP estimation with $C_i$ estimated via the simple λ-based method. This figure shows the results from the CA-obs site using all of the half-hourly data obtained during the entire study period. The solid lines represent the average dynamics, and the shaded areas represent 95% confidence intervals. Similar results were obtained at the other sites.

**Figure 4.** Comparison between the diurnal dynamics of GPP estimations from the big-leaf model and the (a) layered, (b) two-leaf, and (c) layered two-leaf models and the corresponding (d) incident PAR, (e) temperature, (f) SIF, and (g) GPP on July 29, 2019, and August 2, 2019. (h) shows the changes in estimated J/SIF ratio, and (i) shows the dynamics of estimated J using the big-leaf model. The shaded areas represent the 95% interval. All the data used in this figure were obtained from the CA-obs half-hourly dataset.

**Figure 5.** Diurnal dynamics of GPP estimation in different layers. The GPP estimations in (a) and (b) came from the layered model, and the GPP estimations in (c) and (d) came from the layered two-leaf model. The color of the dots represents the layer index, and a larger number represents a deeper location within the canopy. The LAI of each layer in this figure can be

calculated as total LAI/10.

**Figure 6.** Depths of the layer above which the leaves contributed 80% of the total GPP on July 29, 2019, and August 2, 2019. Data used for depth estimation and plotting were half-hourly estimations from (a) the layered model and (b) the layered two-leaf model at the CA-obs site.

**Figure 7.** (a) Diurnal variation in the GPP contribution of shaded leaves; (b) seasonal variation in the GPP contribution of shaded leaves; (c) diurnal variation in the LAI fraction of shaded leaves; (d) seasonal variation in the LAI fraction of shaded leaves. The cross-marks in the plots represent the outliers, the black dots represent the mean values of each box, and the green lines represent the median values of each box.

**Figure 8.** The light response of single-leaf qL (in red), canopy-scale qL obtained from the layered model (in gray), and canopy-scale qL from the two-leaf model (in pink). The PAR label of the x-axis refers to the incident PAR obtained at the top of the canopy.

**Figure 9.** The impact of LAI on the light response of the (a) canopy-scale qL from the two-leaf model; (b) canopy-scale qL of sunlit leaves; (c) canopy-scale qL of shaded leaves. The color of the dots represents the corresponding LAI. The PAR label of the x-axis refers to the incident PAR obtained at the top of the canopy.

**Figure 10.** The diurnal patterns of single-leaf qL (red lines), canopy qL from the layered model (black lines), canopy-scale qL from the two-leaf model (green lines), and the qL in different layers of the canopy (colored scatters). The color of the dots represents the layer index, and the larger number represents the deeper location within the canopy. The LAI of each layer in this figure can be calculated as total LAI/10.

Figure 1



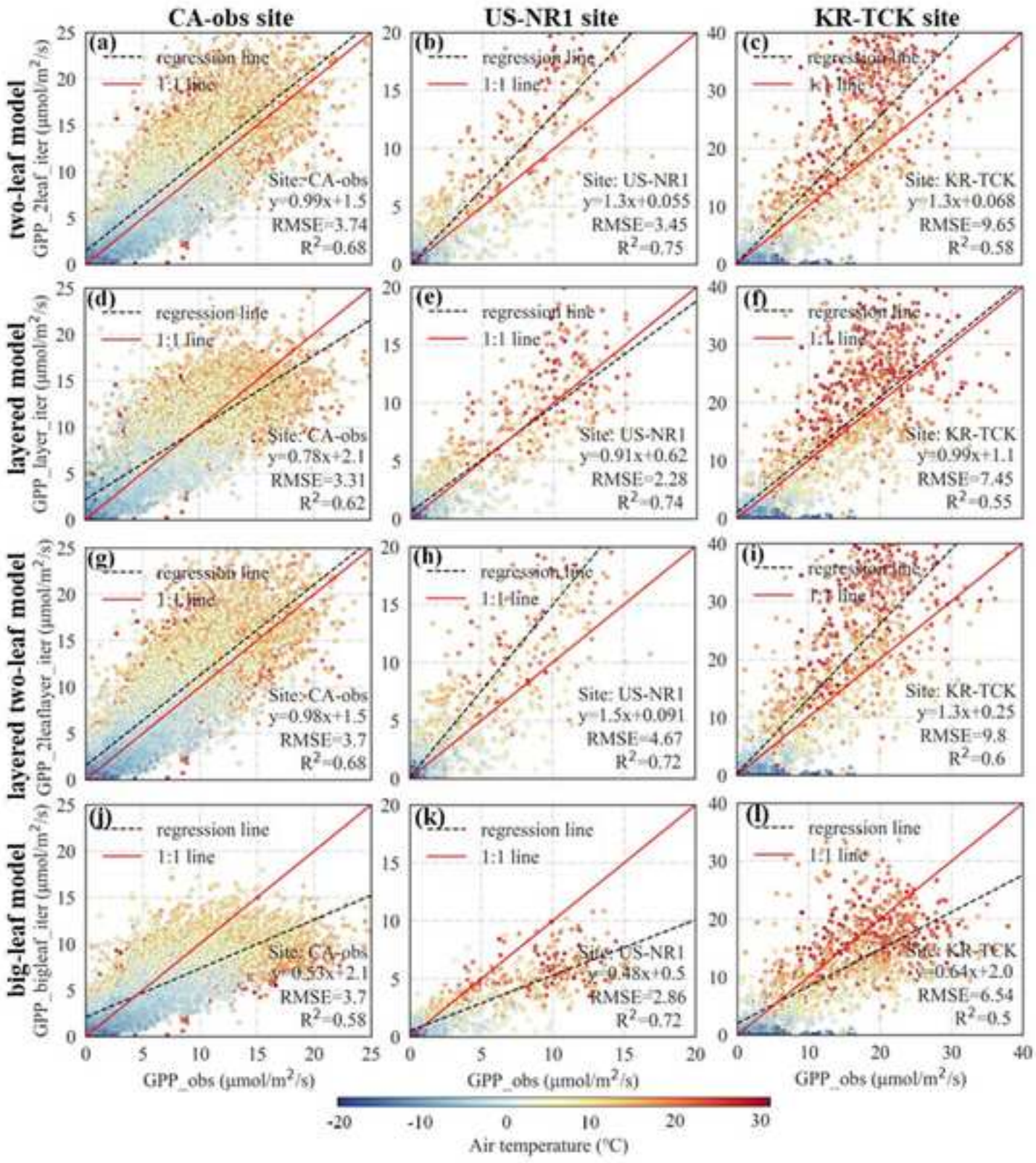

Figure 2

Click here to access/download;Figure;Figure 2.jpg

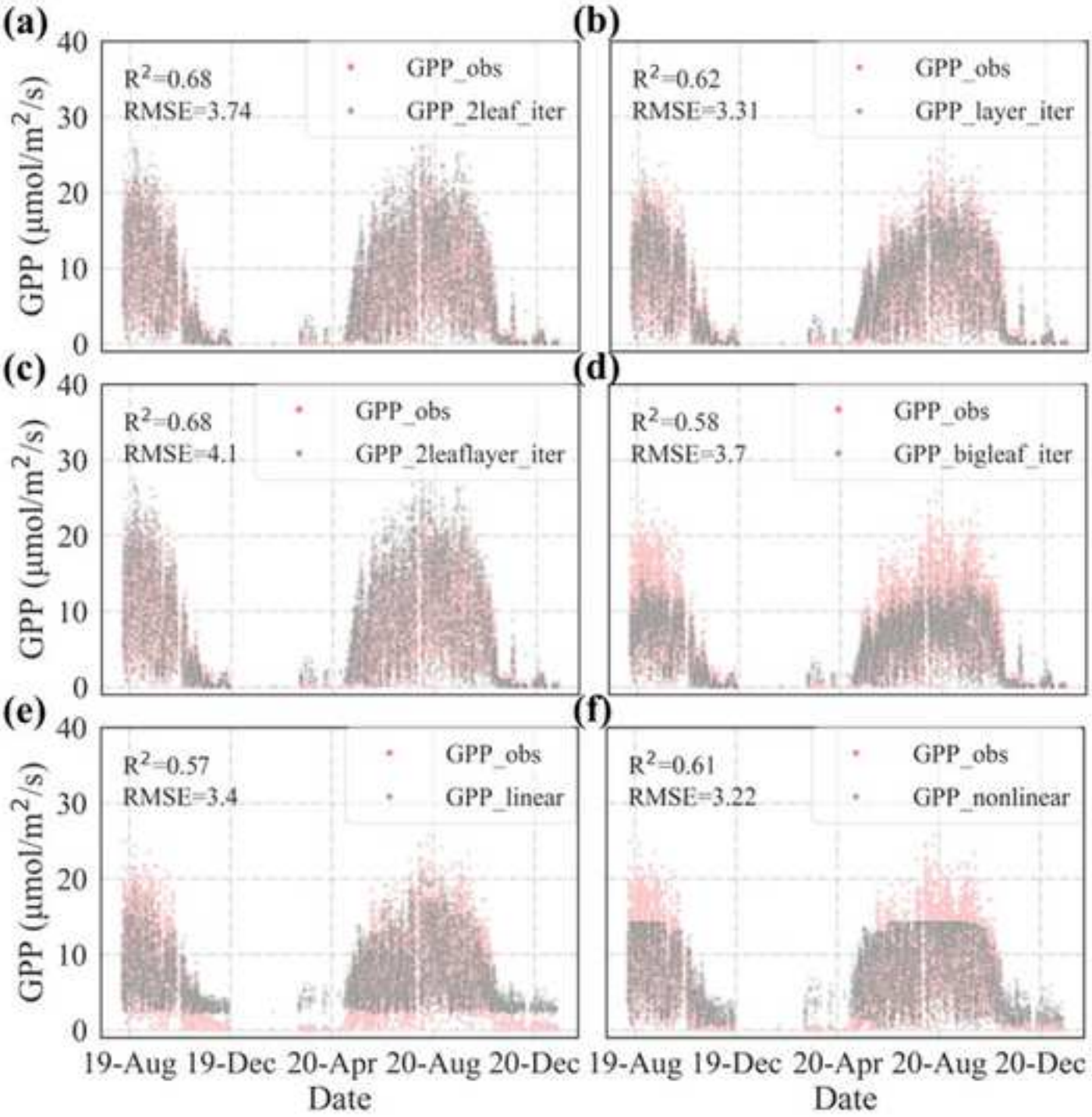

Figure 3



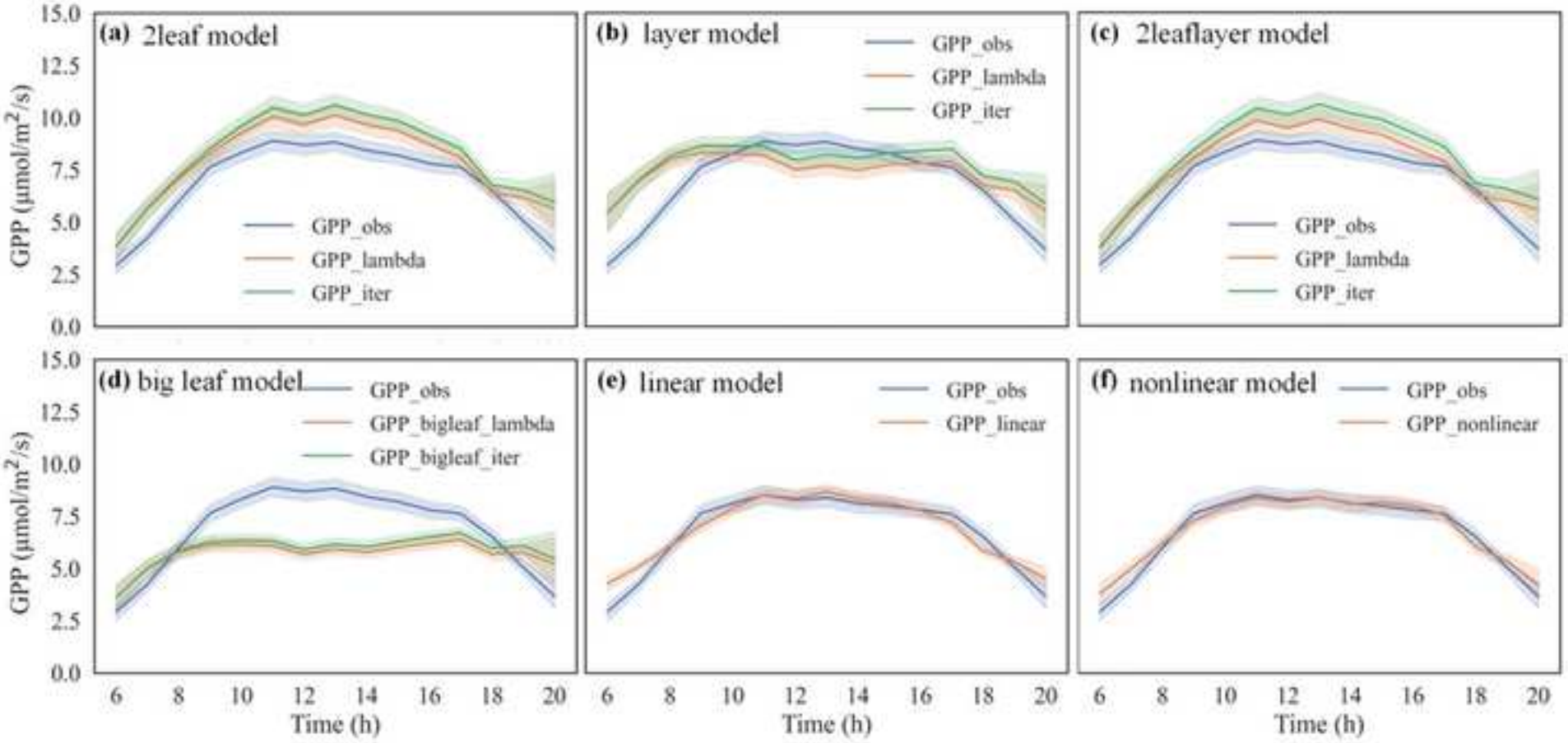

Figure 4

Click here to access/download;Figure;Figure 4.jpg

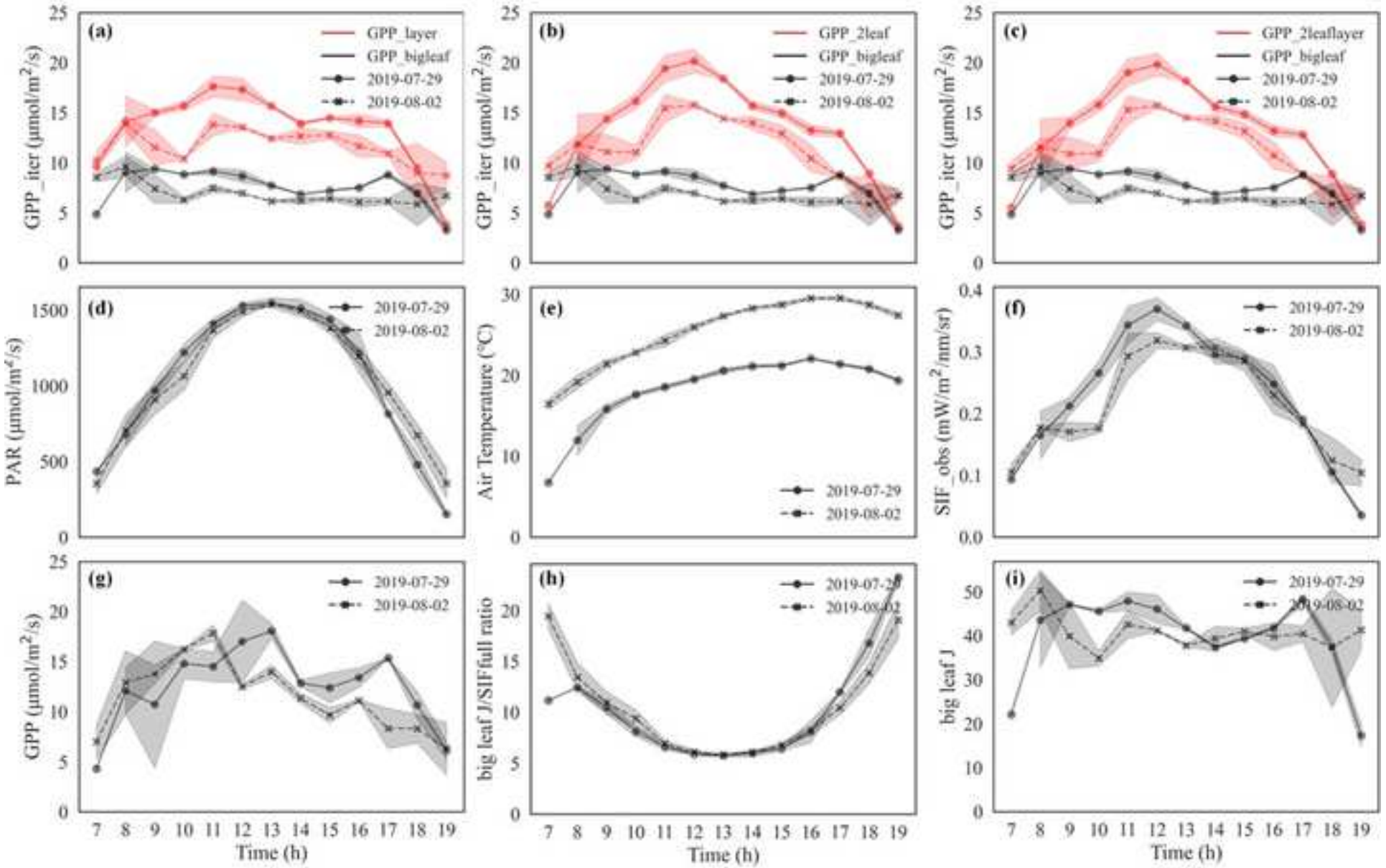

Figure 5



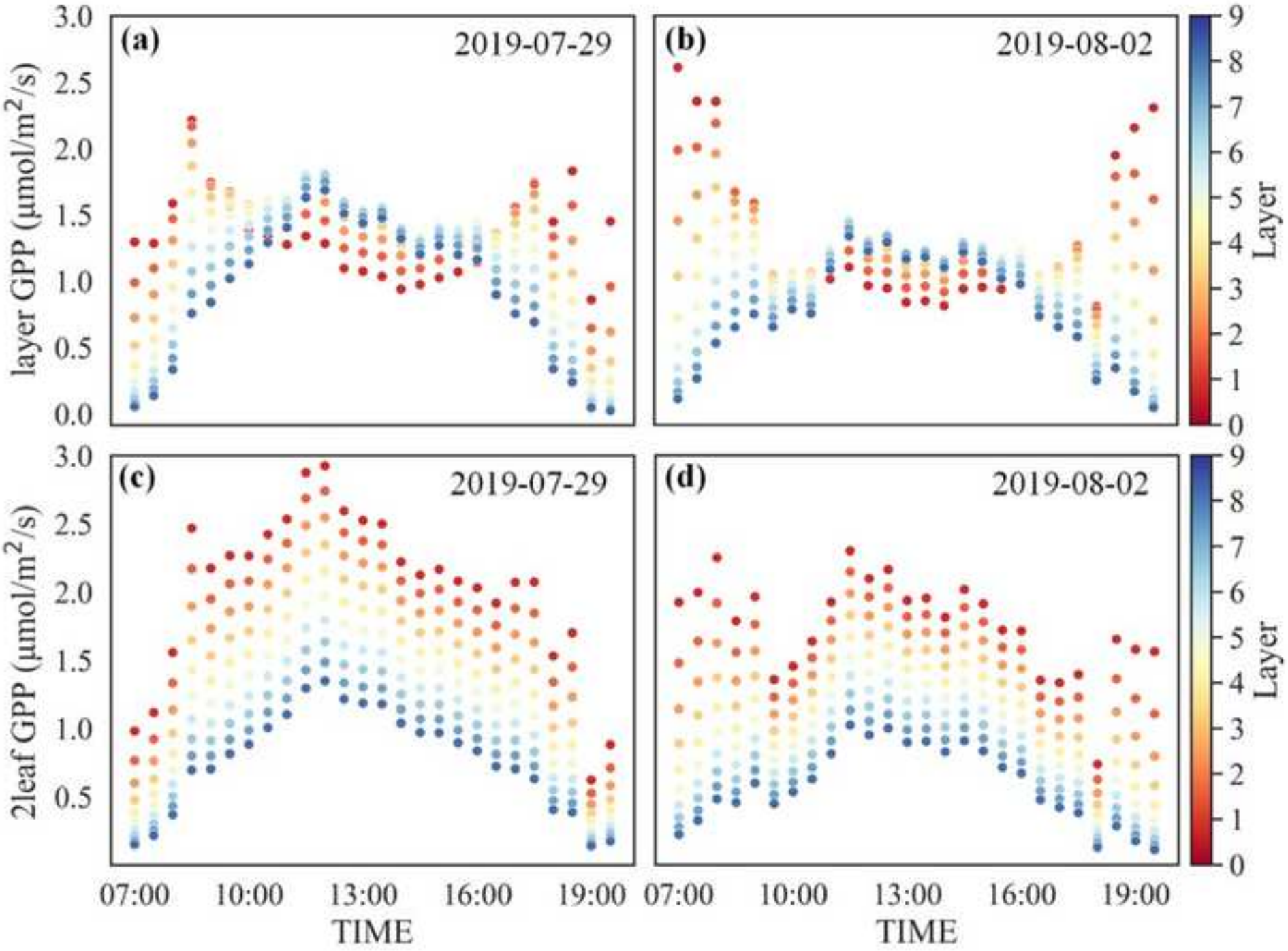

Figure 6

Click here to access/download;Figure;Figure6.jpg

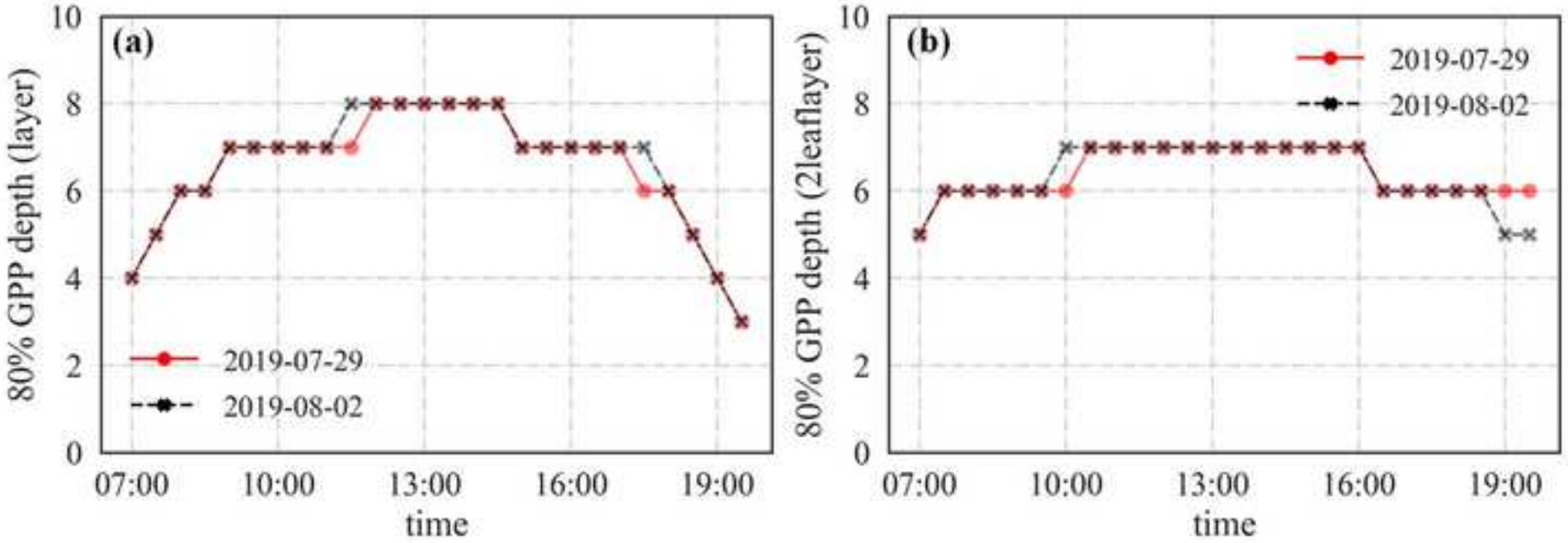

Figure 7



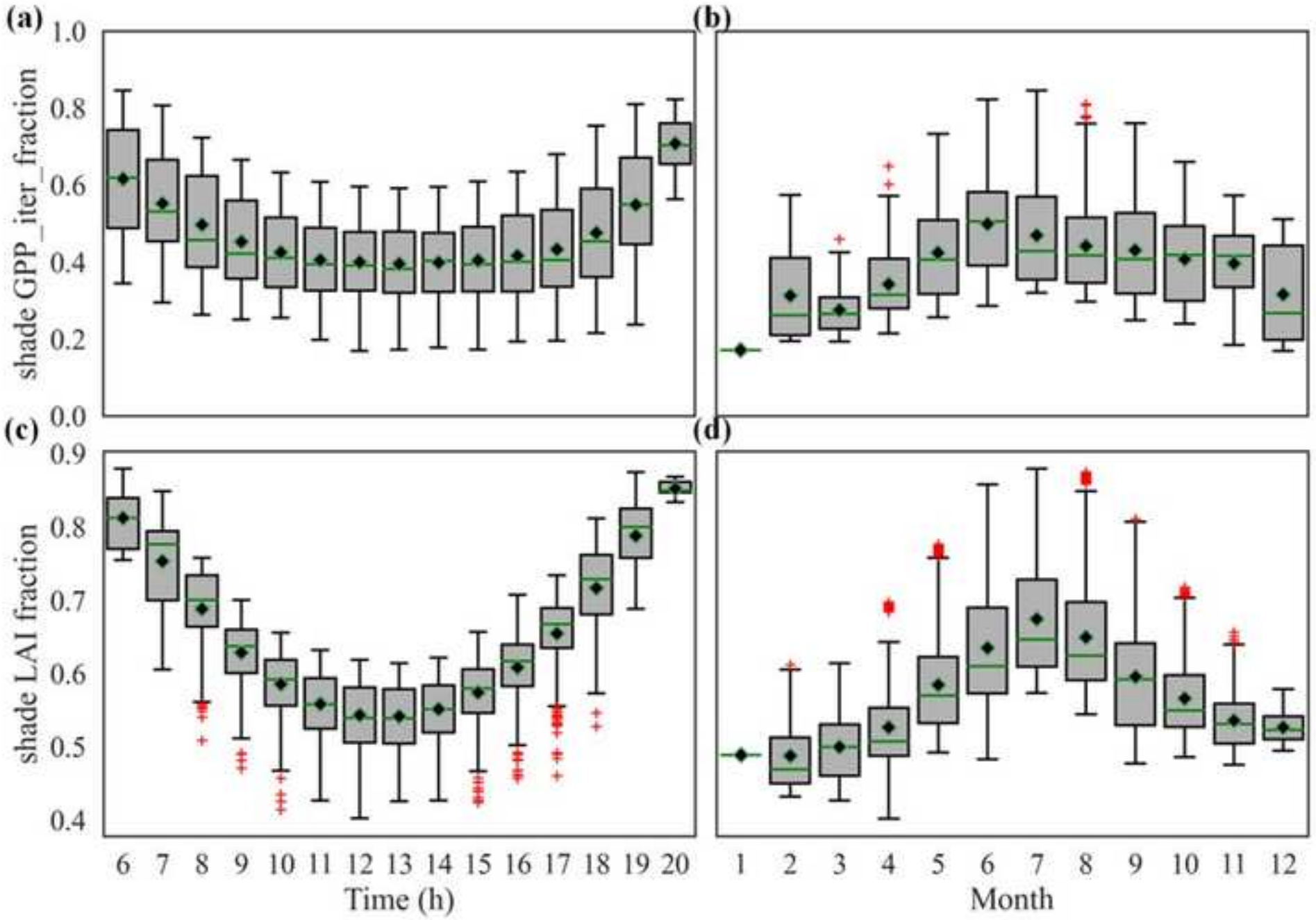

Figure 8

Click here to access/download;Figure;Figure 8.jpg

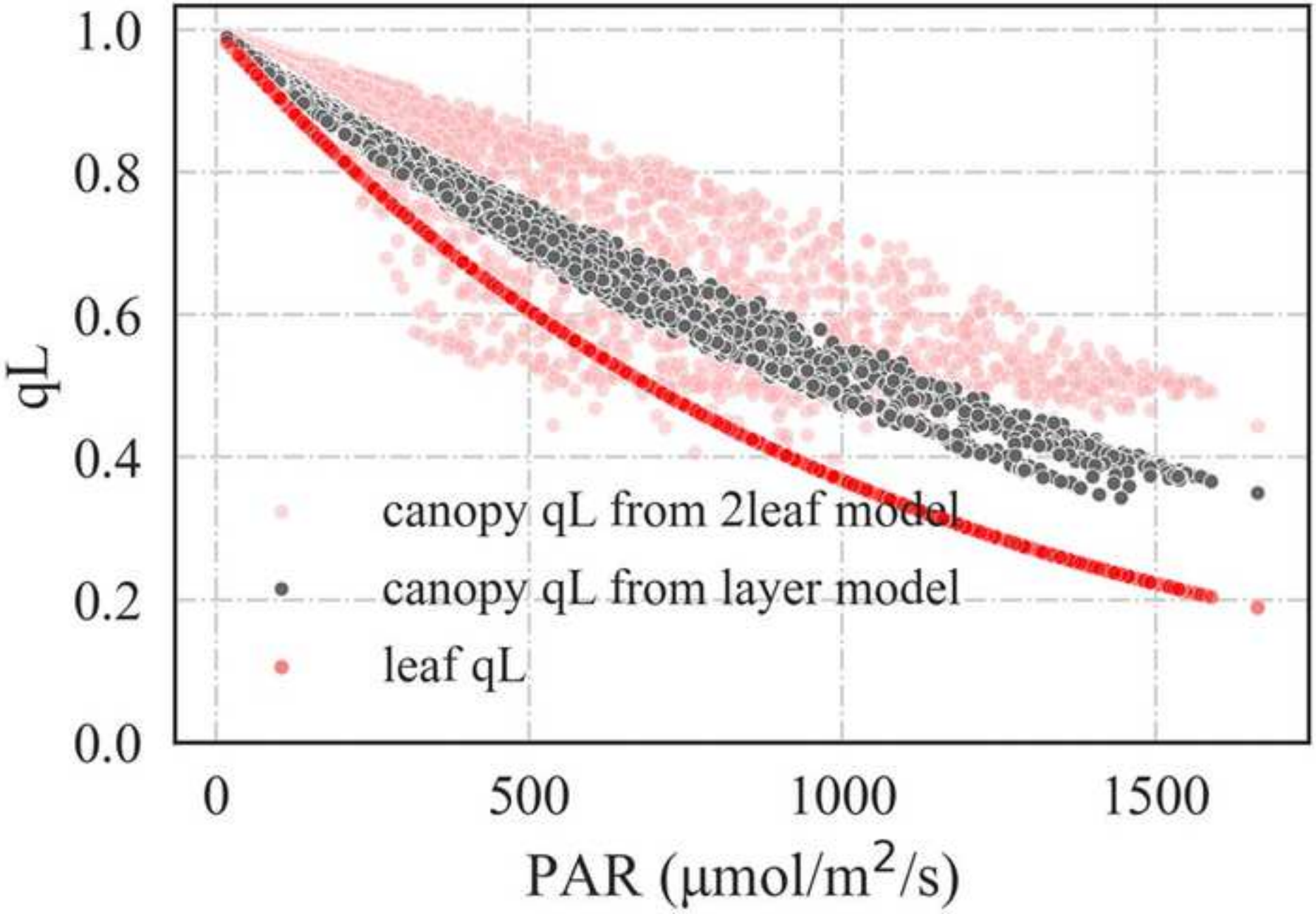

Figure 9

Click here to access/download;Figure;Figure 9.jpg

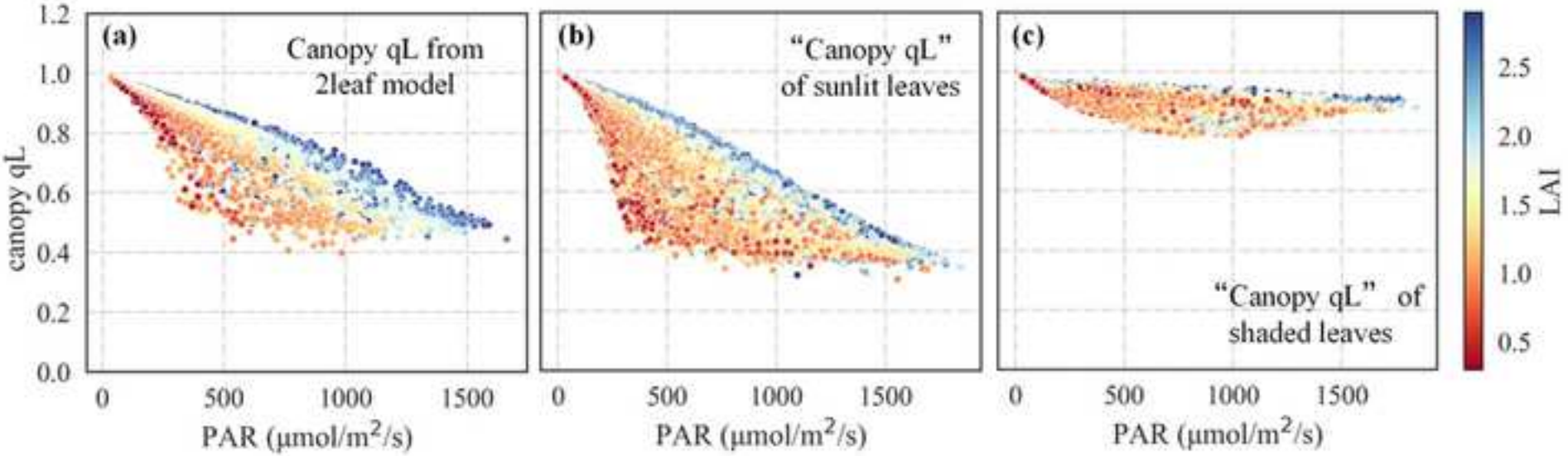

Figure 10

Click here to access/download;Figure;Figure 10.jpg